Manipulation of Lamb waves with elastic metamaterials

Wei Wang

Sorbonne Université

Université Pierre et Marie Curie

Sciences Mécaniques, Acoustique, Electronique et Robotique de Paris (SMAER)

Manipulation of Lamb Waves with Elastic Metamaterials

Par **Wei WANG**

Thèse de doctorat préparée à l'Institut des NanoSciences de Paris (INSP)

Présentée et soutenue publiquement le 4 octobre 2019

Devant le jury composé de :

Rapporteurs :

M. Bruno MORVAN	Professeur, Université Le Havre Normandie
M. Abdelkrim TALBI	Professeur, Ecole Centrale Lille

Examinateurs :

M. Thomas BRUNET	Maître de Conférence, Université de Bordeaux
M. Bahram DJAFARI-ROUHANI	Professeur, Université Lille 1
M. Régis MARCHIANO	Professeur, Sorbonne Université
M. Yan PENNEC	Professeur, Université Lille 1

Directeur de thèse :

M. Bernard BONELLO	Directeur de Recherche CNRS – Sorbonne Université

To my parents

To my family

To my friends

Acknowledgements

This thesis was accomplished in Institut des Nanosciences de Paris (INSP) at Sorbonne Université and funded by China Scholarship Council, from October 2016 to October 2019. I would like to dedicate this work to all those who have offered me tremendous assistance during the past three years.

I wish to acknowledge the jury members of my dissertation defense, Prof. Bruno Morvan, Prof. Abdelkrim Talbi, Dr. Thomas Brunet, Prof. Bahram Djafari-Rouhani, Prof. Régis Marchiano, Prof. Yan Pennec and Dr. Bernard Bonello for taking time to review my manuscript and attend my defense. Your professional suggestions and discussion help to improve the quality of my manuscript.

I would like to express my sincerest gratitude to my advisor, Dr. Bernard Bonello, for giving me this precious opportunity to conduct academic research in INSP. Your expert instructions and guidance have been the most important foundation of my research. Your profound experience and knowledge in the experiments deeply impressed me. Regardless of the heavy work, you were always patient with me whenever I came to you with any kinds of questions. Thank you for your efforts spent in polishing the articles and your warm encouragement and strong support when suffering from the rejection.

I would like to express my deepest gratefulness to our collaborators, Prof. Bahram Djafari-Rouhani and Prof. Yan Pennec at Universté de Lille 1. Your thorough knowledge in the scientific fields of the phononic crystals and the metamaterials greatly broadened my horizons. And I really enjoyed and benefit a lot from the fruitful discussion each time when we visited you. It is your professional remarks and constructive suggestions that consolidate the success of my works included in this thesis.

I want to thank my friend Dr. Xin Fang, the former exchange student, for his technical supports in the numerical calculation and discussion in the daily work at the very beginning of my research study. I would like to present my heartfelt appreciation to my friends Dr. Feng Xu, Dr. Ning Liang and Dr. Tengfei Li. They are not just friends, but rather like mentors in my life. Thank you for your continuous concern, guidance and encouragement. I will always remember the pleasant moments we spent at every weekends and travelled in Venezia and Nice. I also want to thank my colleague and friend Dan Zhao, for her suggestions and encouragement and for sharing the interesting things that brings happy hours into the monotonous research work.

Special thanks should be given to my friend Dr. Mingguan Yang and his wife Jian Zhou. It is you that encouraged me to make the decision to resign and came to France to pursuit for the doctoral degree. My thanks also go to my friend Dr. Hao Jiang, my high school classmate. Staying with him I can speak the dialect that makes me feel at home.

I would like to thank my friends I have met in the Cité Internationale Universitaire de Paris who make my life colorful and unforgettable. Special thanks are given to Dr. Shijie Dong, Dr. Weiwei Fang, Zhelu Hu, Dr. Haidai Hu, Xiao Liu, Kankan Qin, Wenyi Wu, Dr. Yishan Ye, Dr. Huaning Wang and Dr. Teng Zhang, I enjoyed playing badminton with you.

I wish to thank my colleagues in the acoustic team in INSP, especially Dr. Cyril Jean, Dr. Camille Lagoin and Ronan Delalande. I really appreciated your assistance and enjoyed the delightful moments staying with you in our office.

I highly appreciate the valuable remarks from Dr. Yabin Jin and Dr. Jinfeng Zhao at Tongji University. I would like to thank Prof. Yongdong Pan and Prof. Zheng Zhong for recommending me to study for the doctoral degree with Dr. Bernard Bonello.

Last but not least, I wish to express my deepest gratitude to my parents and my family for their constant support and unconditional love.

Contents

General introduction

Over the past three decades, the discovery and development of phononic crystals and metamaterials have revolutionized the manipulation of wave propagation in both the elastic and acoustic mediums [1–5]. Owing to the periodically modulated elastic modulus and mass density in a scale either comparable to the wavelength (phononic crystals) or much smaller than the wavelength (metamaterials), many remarkable wave propagation phenomena unachievable in the nature materials have been predicted theoretically and demonstrated experimentally, including band gap [6], negative refraction [7], over-the-diffraction-limit imagining [8], acoustic cloaking [9], non-reciprocal propagation [10], etc.

Designing artificial structures to manipulate elastic waves, especially Lamb waves that are widely used in the industrial applications, through either band folding or local resonance has been one of the most fruitful scientific pursuits. One decade ago, pillar type structure that consists of depositing a periodic array of cylinders on a plate was firstly developed [11,12]. It has been proved to be one promising candidate in controlling Lamb waves. The pillar can function as either a scatter when the wavelength in the plate is comparable to the periodicity or a resonator if the wavelength is much larger than the periodicity. Thus, both Bragg and low frequency band gaps can be generated [13–15]. When behaving as a resonator, it exhibits three kinds of resonances, namely the bending, the compressional and the torsional modes [16]. The bending and compressional vibration can easily couple with the symmetric and antisymmetric Lamb waves and the torsional motion can interact with the shear-horizontal Lamb waves [17–19]. Obviously, the pillar type periodic structures have significant potentials in controlling the propagation of Lamb waves. Especially the pillared metamaterials, it can modulate the wave propagation in the subwavelength scale. In that system, instead of merely designing local resonance to form a low frequency band gap that simply blocks the wave propagation, it is more interesting to investigate the occurrence of the doubly negative property [20–22], simultaneously negative effective elastic modulus and mass density, that not only allows for the wave propagation, but also processes the negative group velocity which can be further adopted to realize the negative refraction, lensing and cloaking [23–25].

In recent years, the emergence of topological insulators provides a fascinating way to realize the defect-immune and lossless energy transport. Unidirectional wave propagation at the domain between two topologically distinct systems has been experimentally observed and the associated topological nature ensures the suppression of the backscattering in the presence of impurities and disorders [26–28]. Owing to

the bulk-edge correspondence, the difference in topological invariants guarantees the number of the edge states. By analogy with the quantum Hall effect, the quantum spin Hall effect and the quantum valley Hall effect, this concept was soon extended to phononic crystals. While breaking the time-reversal symmetry in the system, the topological chiral edge states emulating the quantum Hall effect will occur at the boundary [29–31]. Upon the reservation of the time-reversal symmetry in the configuration, the topological pseudospin-protected edge states [32–34] in analogy to the quantum spin Hall effect and the topological valley-protected edge states [35–37] mimicking the quantum valley Hall effect will occur at the domain wall. More interestingly, the topological pseudospin-valley combined edge states have been reported very recently which utilizes both the pseudospin and valley degrees of freedom [38–44]. Inspiring by these, we raise the interests to investigate the topological transport of Lamb waves in the pillar type structure that can provide an extraordinary approach to robustly guide Lamb waves.

Besides these passive designs that are only suitable for the predefined applications, the actively tunable phononic crystals and metamaterials have gained considerable attention owing to the imminent quests on the time-dependent wave propagation modulation [45,46]. In these systems, an external field originating from the electronic, the magnetic or the mechanical devices is usually introduced which can dynamically tune the effective properties in a relatively narrow frequency interval [47–50]. By analogy with these, it might be interesting to involve external sources into the pillar type systems to achieve the timely modulation of Lamb waves.

This manuscript is devoted to develop passive and active approaches to manipulate Lamb waves in the pillared phononic crystals and metamaterials. It is organized as follows. In the first chapter, we firstly investigate the negative properties associated with the bending, the compressional and the torsional modes in two square lattice single-sided pillared metamaterials. Secondly, two different schemes to achieve the doubly negative property are explained in details. The potentials of the doubly negative property in the negative refraction and acoustic cloaking is numerically demonstrated.

In the second chapter, we investigate the topological transport of Lamb waves in the pillared phononic crystals. To begin with, we recall the methodology in constructing a single Dirac cone and a double Dirac cone by folding the band structure. After that, the occurrence of the topologically valley-protected edge states in an asymmetric double-sided pillared phononic crystal is discussed. The unidirectional propagation of the edge states at different domain walls are studied. Besides, we consider a symmetric double-sided pillared phononic crystal where the symmetric and antisymmetric modes can be totally decoupled. The occurrence of the topologically valley-protected, pseudospin-protected and pseudospin-valley combined edge states is demonstrated. The refraction and transmission of the topological edge states at the zigzag and armchair terminations is studied.

In the third chapter, we present an active method to control the transmission of zero-order antisymmetric Lamb wave propagating through an infinite line of pillars. Two different systems with the second-order bending resonance and the first-order compressional resonance of the pillars separated and superimposed are taken into consideration. In contrast to the metamaterials, the coupling between the neighboring pillars is discussed. External traction force and pressure are then applied on the pillars that can well couple with the bending and compressional vibration. Both the magnitude and relative phase of the external sources against the transmission coefficient are studied. The efficiency of the external traction force and pressure is also evaluated.

Chapter 1

1 Doubly negative property in double-sided pillared metamaterials

1.1 Introduction

The advent of locally resonant metamaterials almost two decades ago [51], and the great deal of research that ensue [2–5], have significantly contributed to the possibilities we have now for controlling the propagation and the dispersion of acoustic and elastic waves. Some effective properties of these artificial structures may exhibit abnormal behaviors in narrow frequency intervals where they may be infinite positive, null or even negative. In these frequency intervals where only one effective parameter is negative, the mass density, the bulk modulus or the shear modulus, the wave propagation is completely forbidden that leads to the total reflection of the incident wave, impinging on the metamaterial from the adjacent homogeneous medium within which the wavelength may be several orders of magnitude larger than the lattice constant [52–54]. In contrast, if the structure is engineered to support frequency intervals where the doubly negative property occurs, *i.e.* simultaneously negative effective mass density and bulk (shear) modulus, phenomena not present in nature may arise, for instance, the negative refraction, the cloaking effect and the over-the-diffraction-limit imaging. Generally speaking, the doubly negative property can be achieved either by combining two different substructures, each supporting a different resonance or by constructing a single structure where two resonances can occur in the same frequency interval [55].

In the past decade, a couple of acoustic [25,56–63] and elastic configurations allowing for the doubly negative property have been theoretically predicted and experimentally demonstrated. Regarding the elastic systems, it can be classified into discrete and continuum designs. For example, Huang *et al.* [64] put forward a discrete one-dimensional metamaterial by assembling a mass-in-mass subsystem featuring the negative effective mass density and a symmetric mass-truss subsystem featuring the negative effective Young's modulus. Wang *et al.* [65,66] reported both one-dimensional and two-dimensional discrete metamaterials which allows to independently control the effective mass density and stiffness. Concerning the continuum systems, for instance, Liu *et al.* [21] proposed a three-constituents chiral metamaterial made by embedding soft-coated heavy cylinders into a polyethylene matrix that achieves the doubly negative property thanks to the combination of the translational and rotational resonances of the heavy cores. Introducing the same two resonances but this time in a single-phase metamaterial plate, Zhu *et al.* [23] observed the subwavelength negative refraction of the longitudinal elastic wave experimentally and demonstrated in this way the

occurrence of simultaneously negative effective mass density and bulk modulus. Lai *et al.* [20] proposed a two-dimensional elastic metamaterial that comprises a multi-mass locally resonant inclusion in the unit cell. It exhibits the monopolar, the dipolar and the quadrupolar resonances that can respectively turn the mass density, the bulk modulus and the shear modulus negative. However, in most of these aforementioned metamaterials, the doubly negative property only occurs in a very narrow frequency interval which may constitute a drawback for many applications. To overcome this difficulty, Dong *et al.* [24] developed a topology optimization scheme to design a two-dimensional single-phase anisotropic elastic metamaterial with the broadband doubly negative property. Besides, its ability in the superlensing effect as well as the cloaking effect in the deep subwavelength scale for both the longitudinal and transverse elastic waves is numerically evidenced.

Nevertheless, most of these research was dealing with the bulk waves whereas the modulation over other types of elastic waves, such as Lamb waves, is a prerequisite to the development of the planar double-negative elastic metamaterials. Along this line, a single-phase elastic metamaterial featuring two independent resonators inside the plate allowing to independently tune the effective mass density and stiffness was proposed and experimentally investigated by Oh *et al.* [67]. Later on, the same group experimentally demonstrated the subwavelength focusing of the zero-order symmetric Lamb waves in the proposed structure [68]. Chen *et al.* [69] reported an adaptive hybrid metamaterial that possesses both the negative effective mass density as well as the extremely tunable stiffness by properly adjusting both the mechanical and electric elements. Furthermore, Gusev *et al.* [22] presented a double-negative metamaterial plate for the flexural waves based on the resonant elements attached to a thin plate. In this design, the negative effective mass density is achieved by the normal-force interactions whereas the effective stiffness becomes negative owing to the rotationally resonant mechanical elements.

More practical candidates in that respect are probably the pillared metamaterials which could be described as phononic stubbed plates constructed by depositing periodic cylindrical dots on a thin homogeneous substrate as independently proposed by Pennec *et al.* [11] and Wu *et al.* [12]. It has been reported that the pillared metamaterials can achieve both high frequency band gaps associated to the Bragg scattering and low frequency band gaps related to the local resonances of the pillars [70–75]. However, the locally resonant band gap is usually very narrow that poses great challenges to the applications. To deal with this, Assouar *et al.* [76] developed a two-dimensional double-sided pillared metamaterial and theoretically predicted that the relative bandwidth of the locally resonant band gap can be significantly increased by a factor of two compared to the classical one-sided counterpart. Subsequently, Bilal *et al.* [77,78] proposed another design within which the pillars stand in between the holes regularly patterned in the plate. This structure, sometimes referred as a trampoline, allows to broaden the low frequency band gap by a factor of four. Very recently,

such pillared metamaterials have been employed to manipulate the surface acoustic wave. Zhao *et al.* [79] experimentally demonstrated the subwavelength focusing of Rayleigh waves using the gradient-index pillared phononic crystals made of air holes scatters in a thick silicon substrate. Benchabane *et al.* [80] reported the manipulation of the mechanical vibrations at the micron scale by exploiting the interaction between the individual, isolated pillars and the surface acoustic waves. Oudich *et al.* [81] proposed a composite pillar made of a one-dimensional phononic crystal and observed the confined modes at the pillar-substrate interface that couples with the surface acoustic waves and causes their attenuation. The aforementioned wave propagation phenomena in the pillared metamaterials or phononic crystals ensue from the interaction between the vibration of the pillars at resonances and the elastic waves propagating in the substrate. Generally, three kinds of resonances can be involved in the dynamic properties of these systems, namely the bending, the compressional and the torsional modes that in the low frequency regime can couple with the zero-order symmetric (S_0), the zero-order antisymmetric (A_0) and the zero-order shear-horizontal (SH_0) Lamb waves propagating in the plate respectively.

Up to now, the realization of the doubly negative property in the pillared metamaterials have never been reported. And the quest to manipulate Lamb waves in the subwavelength scale becomes one of the most interesting scientific topics in physical acoustics. This is why we perform this study in this chapter to seek a new way to control the propagation of Lamb waves. It is constructed as follows. In Sec. 1.2, the single negative property in the single-sided pillared metamaterials is analyzed. Subsequently, the first mechanism to achieve the doubly negative property founded in an asymmetric double-sided pillared metamaterial is reported in Sec. 1.3. Then, we investigate a more specific situation in Sec. 1.4, a symmetric double-sided pillared metamaterial, that provides a second mechanism to realize the doubly negative property. In Sec. 1.5, we illustrate some applications with the proposed double-negative pillared metamaterial and demonstrate the occurrence of the doubly negative property in return. Finally, it ends with the general conclusion in Sec. 1.6.

1.2 Single negative property in single-sided pillared metamaterials

1.2.1 Lamb waves in a periodic structure

Before analyzing the band structure and the dynamical properties of the pillared metamaterials, we briefly recall the main features of Lamb waves in the periodically structured plates. Lamb waves are the solutions of the equations of motion for a harmonic wave propagating in a medium with a finite thickness along one direction of space and infinite along the other two, with the boundary conditions that the components of the stress in the direction normal to the free surfaces are zero. Owing to the mirror-symmetry with respect to the mid-plane of the plate, these modes can be distinguished as symmetric and antisymmetric modes. In a

homogeneous isotropic medium, the three lowest branches are respectively the antisymmetric flexural branch and the symmetric shear horizontal and longitudinal branches. The higher branches have a cut-off frequency as the wave vector **k** approaches 0 and those modes are highly dispersive. The phononic crystal plate is usually constructed by inserting periodic inclusions (holes) into the plate or by depositing pillars on it. The dispersion curves of this periodic inhomogeneous medium are now described in the corresponding two-dimensional Brillouin zone (BZ) with their dynamical properties having specific characteristics including the band gaps, the folding of the dispersion curves and the mode conversion. In particular, the strong resonances associated with the pillars can be very efficient in opening band gaps. Although the branches have more complex character and coupling between the displacement components than in a homogeneous plate, some branches still feature the flexural, the longitudinal or the shear horizontal character. In the case of the single-sided pillared metamaterials, the mirror-symmetry with respect to the mid-plane of the plane in the unit cell is strictly speaking broken, while this mirror-symmetry property can be restored in the case of the double-sided pillared metamaterials (Sec. 1.4) which allows to separately investigate the symmetric and antisymmetric modes. We show that this property can be very helpful in designing the double-negative pillared metamaterial.

1.2.2 Negative effective mass density

In this part, we are going to analyze the dynamical properties of a single-sided pillared metamaterial arranged in the square lattice. The elementary unit cell is displayed in figure 1.1(a) where a denotes the lattice constant, d and h stand for the diameter and the height of the pillars respectively and e is the thickness of the plate. The periodicity lies in the plane (x, y) and the z-axis is chosen to be perpendicular to the plate. In order to obtain the dynamic properties in the MHz range, we assumed these parameters to be a = 200μm, d = 120μm, h = 325μm and e = 100μm. The whole structure is made of steel whose physical parameters are the Young's modulus E = 200GPa, the Poisson's ratio v = 0.3 and the mass density ρ = 7850kg/m^3. Owing to the same material for the plate and the pillars, thus strong coupling between Lamb waves propagating in the plate and the vibrations of the pillars may be expected especially in the vicinity of the resonant frequencies [82]. This proposed single-phase configuration much differs from the composite pillared metamaterial where a soft rubber provides the bonding between the resonators and the stiff plate generally giving rise to the sharp resonances [74,83,84].

The band structure shown in figure 1.1(b) was obtained by applying periodic conditions on the unit cell and solving the eigenequations with COMSOL Multiphysics. The color scale in this figure represents the relative amplitude of the out-of-plane displacement component $\xi = \frac{\iiint_{\text{pillar}} u_z^2 dV}{\iiint_{\text{pillar}} \left(u_x^2 + u_y^2 + u_z^2\right) dV}$. It can be seen that a

complete band gap opens in between 3.17MHz to 3.48MHz. In this frequency interval, the wavelengths of A_0 and S_0 Lamb modes in the plate are about 500µm and 1800µm respectively, *i.e.* more than twice and nine times the lattice constant. Therefore, this low frequency band gap cannot result from the Bragg scattering. It rather suggests that this complete band gap should be ascribed to the local resonances of the pillars. To support this assertion, we have computed the eigenmodes of the unit cell at point M of the BZ for the three branches converging to frequency 3.1MHz [see the inset in figure 1.1(b)]. The results are displayed in figure 1.1(c). Clearly, the deformation concentrates in the pillar whereas it is almost zero in the plate. This is further supported by the flat branches in the lower frequency edge of the band gap that correspond to zero group velocities and are evidences of the local resonances as widely discussed in Refs. [71,76,85,86]. Moreover, the deformation shown in figure 1.1(c) corresponds to the two second-order bending modes, labelled as points A and B, and the compressional mode, labelled as point C. Given the square symmetry of the unit cell, the bending modes A and B are polarized along orthogonal directions and occur at the same frequency.

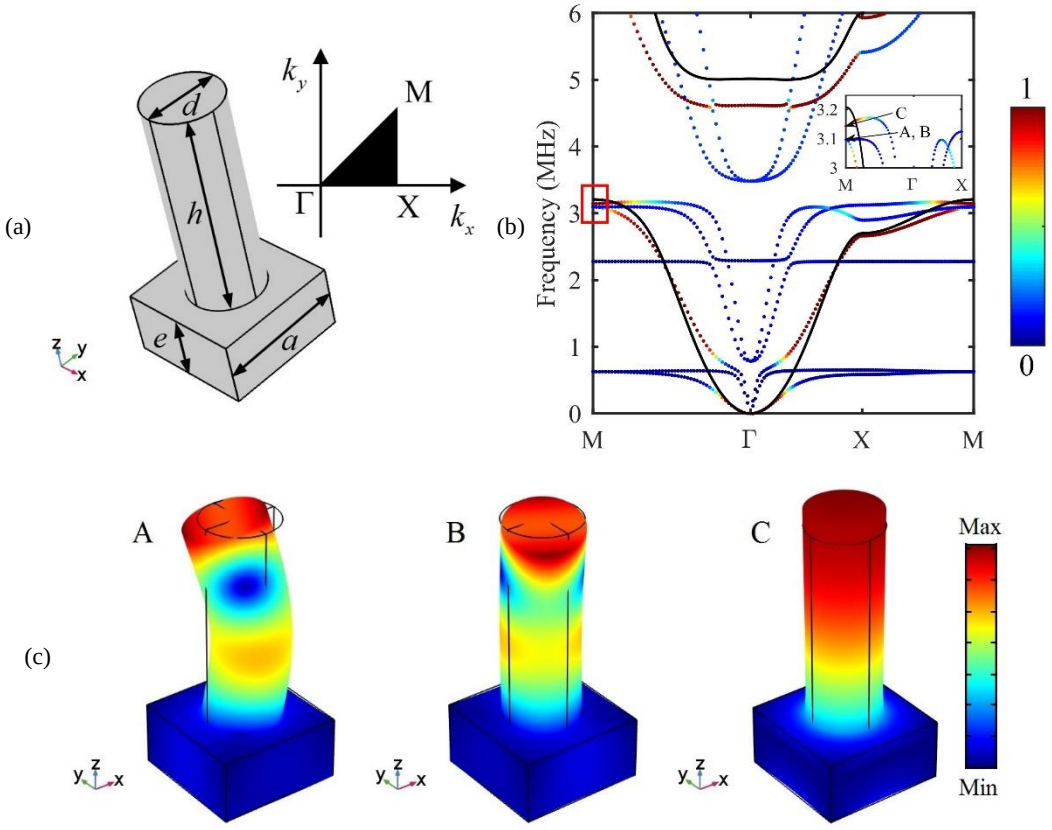

Figure 1.1: (a) Elementary unit cell of the investigated single-sided pillared metamaterial and the first irreducible BZ of the square lattice. (b) Band structure in the low frequency regime along the high symmetry axes of the first irreducible BZ. The color scale corresponds to the relative amplitude of the out-of-plane displacement component, integrated over its volume (see text). For comparison, the band structure of the simplified system described by

equation (1.1) is shown as the black solid lines. Inset: enlargement of the dispersion curves around 3.1MHz. (c) Eigenmodes of the unit cell at points A, B, and C labelled in (b).

In order to investigate the formation of the low frequency band gap, we employ a frequency response analysis. The method, which is only valid in the long wavelength limit, consists of applying an external displacement field **U** on the four lateral boundaries of the unit cell while leaving free both the top and the bottom faces [16,87]. The induced force **F** exerted on these boundaries is then derived from the stress average over the four boundaries of the unit cell considered as a homogeneous media. In the harmonic regime at frequency $\omega/2\pi$, **F** and **U** are related through $\mathbf{F} = -\omega^2 V \left[\rho\right]_{eff} \mathbf{U}$, where V is the volume of the unit cell and $\left[\rho\right]_{eff}$ is the 3×3 dynamic effective mass density matrix to be determined. This can be done by successively applying the harmonic prescribed displacement $\mathbf{U}_i = U_0 \exp(i\omega t)\mathbf{x}_i$ (i = 1, 2, 3) along one of the axes in the principal coordinate system while the other two components are set to zero. In addition, symmetry arguments allow to reduce the number of the independent matrix components. For the structure we consider here, the z-axis being a four-fold symmetry axis the matrix are invariant through the exchange of the indices 1 and 2 and therefore $\rho_{11} = \rho_{22}$, $\rho_{12} = \rho_{21}$, $\rho_{13} = \rho_{23}$ and $\rho_{31} = \rho_{32}$. Moreover, it has been demonstrated in Ref. [76] that in a pillared metamaterial the off-diagonal terms in $\left[\rho\right]_{eff}$ are null except for values very close to the resonant frequencies where a singularity occurs. Thus, the only elements to be considered are ρ_{11}, $\rho_{22} = \rho_{11}$ and ρ_{33}. Their variations around the lower frequency edge of the band gap are displayed in figure 1.2. The component ρ_{11} that mainly relates to the in-plane motion [modes A and B in figure 1.1(c)], is negative from 3.21MHz to 3.50MHz, whereas ρ_{33} that should be ascribed to the out-of-plane displacement [mode C in figure 1.1(c)], becomes negative from 3.26MHz to 4.63MHz. A complete band gap opens when all the components of the effective mass density matrix become negative, *i.e.* in between 3.26MHz and 3.50MHz in the present case.

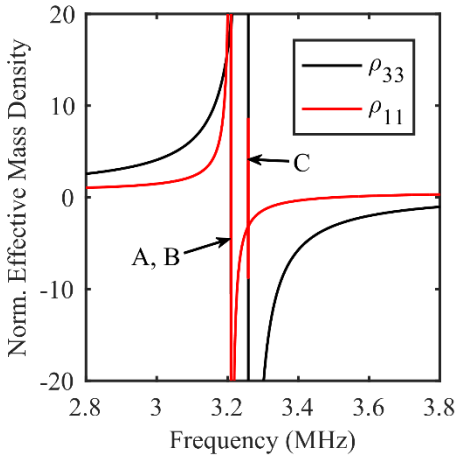

Figure 1.2: Effective mass density matrix components ρ_{11} (red) and ρ_{33} (black) normalized to the mass density of steel as a function of the excitation frequency.

This is in good agreement with the low frequency band gap shown in figure 1.1(b) that goes from 3.17MHz to 3.48MHz. The small discrepancy of about 2.8% on the lower frequency edge of the forbidden band may be readily ascribed to the phase change across the unit cell, not accounted for in the calculation because the preceding theory is only valid in the long wavelength assumption.

Besides this comprehensive approach where the structure is considered as an effective medium, one can also explain the formation of the low frequency band gap owing to a local analysis of the motion of the pillar. In this framework, the resonator is represented by a mass-spring subsystem that couples to the plate within which an elastic wave at frequency $\omega/2\pi$ and wave vector **k** propagates. Let us firstly consider the first-order compressional resonance shown in figure 1.1(c). The pillar vibrates along the *z*-axis and can exert a vertical traction force on the plate. It can be modeled as a mass-spring subsystem with mass *m* and spring stiffness k_C depicted by the right panel in figure 1.3(a). Gusev *et al.* [22] already solved the equations of motion of this corresponding mechanical system and obtained an analytical expression for the effective mass density component ρ_{33}. The governing equations of this simplified model in the frequency domain can be written as:

$$\begin{cases} D\dfrac{\partial^4}{\partial x^4}\hat{u}_z - \rho e\omega^2\hat{u}_z = nk_C\left(\hat{u}-\hat{u}_z\right) \\ m\omega^2\hat{u} = k_C\left(\hat{u}-\hat{u}_z\right) \end{cases}. \tag{1.1}$$

In equation (1.1), Fourier transform of both the vertical displacement of the plate u_z and mass *u* allow to eliminate the time dependence and lead to the variables $\hat{u}_z$ and $\hat{u}$ written in the frequency domain; $D = e^3E/12\left(1-\nu^2\right)$ is the flexural rigidity of the plate that depends on both the Young's modulus *E* and the Poisson's ratio ν; *n* is the number of the mass-springs per unit area; $\omega_C = \sqrt{k_C/m}$ is the resonant frequency of the mass-spring subsystem. Remembering that $\hat{u}_z$ reads $\hat{u}_z = u_0\exp\left(ikx\right)$, we can derive the wave number *k* by solving equation (1.1), namely:

$$k^2 = \omega\left(\frac{e}{D}\right)^{1/2}\left[\rho + \frac{nm}{e\left(1-\omega^2/\omega_C^2\right)}\right]^{1/2}. \tag{1.2}$$

Equation (1.2) shows that k^2 turns imaginary if ω takes a value in between ω_C and $\left(1+nm/\rho e\right)^{1/2}\omega_C$, hence preventing the propagation of the flexural waves in the plate. Moreover, equation (1.2) allows to define the effective mass density as:

$$\rho_{eff}\left(\omega\right)=\rho+\frac{nm}{e\left(1-\omega^2/\omega_C^2\right)}. \tag{1.3}$$

It turns negative when the excitation frequency is in the same interval. This well explains the occurrence of the negative value of the component ρ_{33}. This simplified model can be further extended to the case of a two-dimensional phononic crystal by setting periodic conditions and implementing a plane wave expansion method to derive the dispersion curves [88]. Then, the solution is represented by the black solid lines in figure 1.1(b).

It is less intuitive to establish the governing equations that accurately describe the complex motions of the pillar and the plate for the second-order bending resonance. However, the problem can be simplified by analogizing the single-sided pillared unit cell to the classical cantilevered beam in which the rigid body is replaced by a deformable medium and where the oscillation of the pillar is excited by Lamb wave that propagates in the plate. In this simplified model depicted in figure 1.3(b), the internal forces at the interface between the pillar and the plate can be modeled as a moment and traction force parallel to the plate surface. It allows for a comprehensive analyze of the effective mass density and a better understanding of the occurrence of the negative mass density.

Let us firstly consider the motion of the pillar in the sagittal plane depicted in the middle panel of figure 1.3(b). Since no traction force is considered, the motion reduces to a pendulum motion and can be well modeled by a mass-torsional spring with mass *m*, rotational inertia *J* and torsional stiffness k_B rigidly attached to the plate. Then, the governing equations for the wave propagation along the *x*-axis in this plate-resonator coupled system can be written as [89]:

$$\begin{cases} D\dfrac{\partial^4\hat{u}_z}{\partial x^4}-\rho e\omega^2\hat{u}_z=nk_B\left(\dfrac{\partial\hat{\theta}}{\partial x}-\dfrac{\partial^2\hat{u}_z}{\partial x^2}\right) \\ J\omega^2\hat{\theta}=k_B\left(\hat{\theta}-\dfrac{\partial\hat{u}_z}{\partial x}\right) \end{cases}, \tag{1.4}$$

where $\hat{u}_z$ and $\hat{\theta}$ are the vertical displacement of the plate and the rotation angle of the torsional spring in the frequency domain; k_B and J determine the resonant frequency of the mass-torsional spring subsystem through $\omega_B = \sqrt{k_B/J}$. By solving equation (1.4), we can derive the wave number k, namely:

$$k^2 = \frac{1}{2D}\left\{\left[4De\omega^2\rho + \left(\frac{nJ\omega_B^2}{\omega_B^2/\omega^2 - 1}\right)^2\right]^{1/2} - \frac{nJ\omega_B^2}{\omega_B^2/\omega^2 - 1}\right\}. \tag{1.5}$$

Equation (1.5) allows to define the effective mass density at frequency $\omega/2\pi$ as being:

$$\rho_{eff}(\omega) = \rho + \frac{n^2J^2\omega^2}{4De}\left(\frac{1}{1-\omega^2/\omega_B^2}\right)^2. \tag{1.6}$$

Equation (1.6) shows that ρ_{eff} is always positive whatever the frequency. Therefore, the resonance of the torsional spring cannot explain on its own that ρ_{11} becomes negative in the specific frequency interval and in turn the occurrence of the negative effective mass density. Therefore, it is essential to consider the traction force acting on the foot of the pillar to understand the formation of the negative effective mass density evidenced by the simulations above.

This traction force excites the plate into an oscillation and the pillar can be regarded as an additional mass M attached to the unit cell by the compression springs with stiffness k_H. For the wave propagating along the x-axis, the problem reduces to the classic one-dimensional mass-spring metamaterial depicted in the right panel of figure 1.3(b). One can show that the effective mass density can be written as [90]:

$$\rho_{eff} = \frac{1}{V}\left(m_0 + \frac{M}{1-(\omega^2/\omega_H^2)}\right), \tag{1.7}$$

where m_0 stands for the mass of the plate in the unit cell and $\omega_H = \sqrt{k_H/(M+m_0)}$ is the angular frequency of the assembly "unit cell + additional mass". Clearly, the effective mass density turns negative in between ω_H and $\omega_H\sqrt{1+M/m_0}$. This simple model well explains the occurrence of the negative values of the component ρ_{11}, as well it shows that the existence of a traction force is essential to understand the formation of the negative effective mass density in this single-sided pillared metamaterial. We further show in Sec.

1.4 that it is also essential to explain the negative property in the symmetric double-sided pillared metamaterials.

Therefore, it can be concluded that in the proposed single-sided pillared metamaterial the low frequency band gap can be attributed to the local resonances of the pillars. The effective mass density turns negative in that frequency interval owing to the combination of the bending and the compressional resonances. As for the bending resonance, the motion of the pillars may be broken down into a rotational and a translational component. It is the latter that turns the component ρ_{11} of the effective mass density matrix to be negative, whereas the moment applied to the plate by the rotational motion is ineffective. Regarding the compressional resonance, it results in the negative component ρ_{33} of the effective mass density matrix.

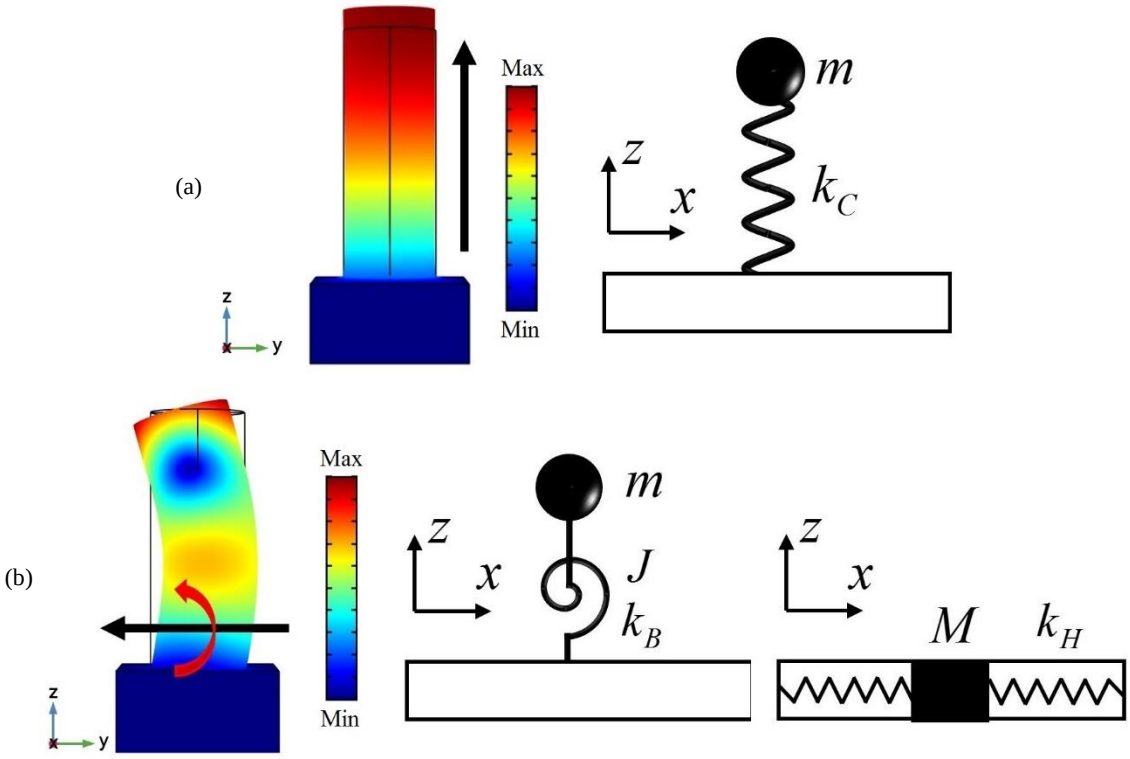

Figure 1.3: (a) Vertical traction force (left panel) and simplified mass-spring subsystem (right panel) for the compressional resonance C. (b) Scheme of the traction force and moment (left panel), simplified mass-torsional spring subsystem (mid panel) and mass-spring subsystem modelling the bending resonances denoted as A and B in figure 1.1(c).

1.2.3 Negative effective shear modulus

As discussed in Sec. 1.2.2, the combination of the bending and the compressional resonances of the pillars can contribute to the negative effective mass density. Remembering that the pillar resonator features three

kinds of resonances, namely the bending, the compressional and the torsional modes, naturally, it might question that whether the torsional mode can lead to the negative property.

Interestingly, it has been theoretically demonstrated by Liu *et al.* [21] and Wang *et al.* [65,66] that the rotational resonance of a core mass in a discrete mass-spring system can generate the negative effective stiffness. By tuning the translational resonance of the core mass to the same frequency interval that achieves the negative effective mass density, then the doubly negative property can be obtained. Afterwards, more practical designs involving the rotational inertia have been proposed to demonstrate both numerically and experimentally its occurrence [21,23,91] which in turn widen the scope of applications. In analogy to these, the torsional vibration of the pillars can couple with SH modes propagating in the thin plate, therefore, the effective shear modulus may potentially become negative as well.

To investigate the torsional mode, we develop another single-sided configuration as shown in figure 1.4(a). The diameter and the height of the pillars were chosen to be d = 110μm and h = 130μm respectively. The other parameters, such as the lattice constant a, the thickness of the plate e and the physical properties, are the same as the one proposed in figure 1.1(a). The corresponding band structure was computed and displayed in figure 1.4(b). It can be seen that no complete band gap occurs in the investigated frequency range from 0 to 7MHz. The eigenmodes of the unit cell evaluated at points A, B and C labelled in figure 1.4(b) are shown in figure 1.4(c). In the eigenmodes at points A and B, unambiguously, the pillar undergoes an alternative torsional motion around its central axis. As for the eigenmode at point C, it represents the first-order compressional resonance.

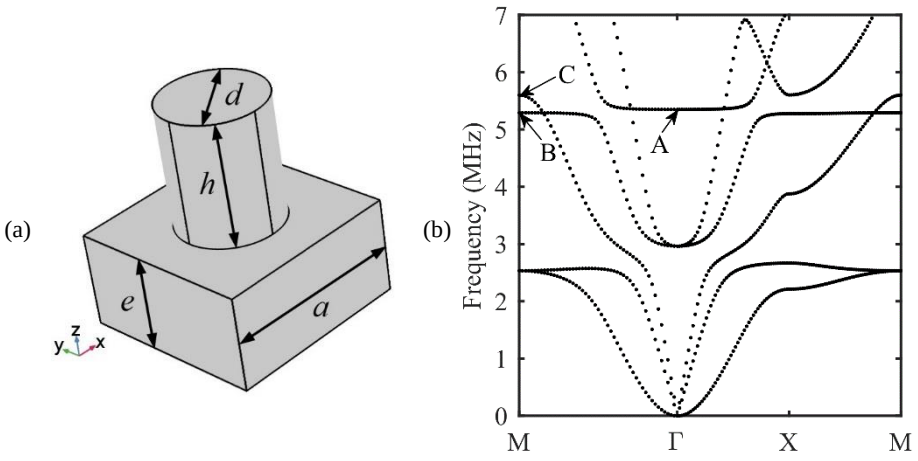

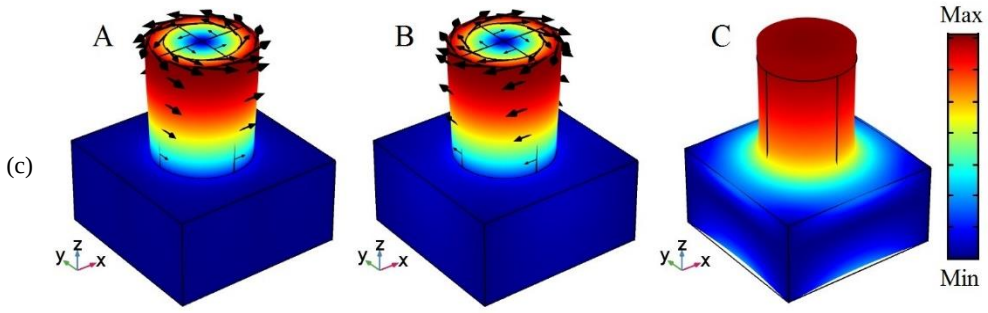

Figure 1.4: (a) Elementary unit cell of the proposed single-sided pillared metamaterial and (b) its corresponding band structure. (c) Eigenmodes of the unit cell at points A, B, and C labelled in (b).

As mentioned before, the torsional motion of the pillars can couple with the local shear deformation of the plate which can potentially modulate the effective shear modulus μ_{eff} of the plate, probably becoming negative. To verify this assumption, we have calculated the effective shear modulus using the numerical method described in Refs. [24,91,92]. In the calculation, instead of a pure shear strain excitation that could not excite the torsional mode, we have considered a simple shear strain field applied along two parallel lateral boundaries. This sets the local displacement field and excites the torsional vibration of the pillar effectively. Then, the variation of the effective shear modulus against the excitation frequency is deduced from the equivalence between the energy of the induced force vectors on the lateral boundaries and the strain energy of the effective medium. The relationship between them can be expressed as $\sum_{\partial V}\mathbf{F}\cdot\mathbf{U}=\frac{1}{2}\mu_{eff}\gamma^2 V$, where ∂V stands for the set of the lateral boundaries and γ represents the amplitude of the applied simple shear strain field. The result displayed in figure 1.5 depicts that the effective shear modulus is negative from 5.29MHz to 5.36MHz, in very good agreement with the frequency interval in between point B (5.29MHz) and point A (5.35MHz). Therefore, it is suggested that a locally resonant band gap should be expected in this interval. However, owing to the dispersion curve of the compressional mode labelled as point C in figure 1.4(c) that goes through this frequency interval, no complete band gap opens. Therefore, we can conclude that the negative effective shear modulus can be achieved by the torsional resonance of the pillar in the single-sided pillared metamaterial.

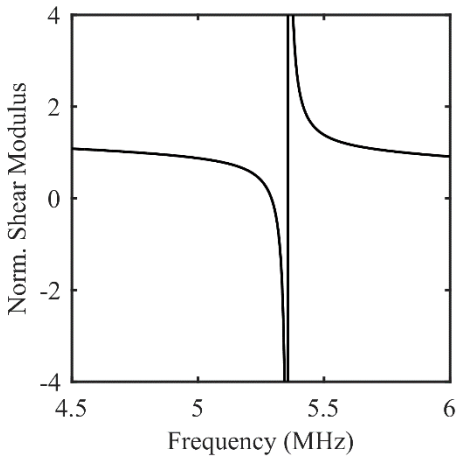

Figure 1.5: Effective shear modulus normalized to the shear modulus of steel as a function of the excitation frequency.

1.3 Doubly negative property in an asymmetric double-sided pillared metamaterial

In Sec. 1.2, we demonstrate that in the single-sided pillared metamaterials the combination of the bending and the compressional resonances of the pillars can generate the negative effective mass density and the torsional mode of the pillars can contribute to the negative effective shear modulus. As proposed in Ref. [55], one practical scheme to achieve the doubly negative property is to combine two different substructures, each supporting a different resonant mode. Therefore, it is suggested that we can assemble the previously discussed two single-sided pillared metamaterials to form a double-sided system within which the negative effective mass density from one pillar and the negative effective shear modulus from another pillar are turned specially to the common frequency interval. Then, the doubly negative property can be expected in the merged structure.

1.3.1 Doubly negative property in merged structure

To achieve this, we develop two different single-sided pillared metamaterials in analogy to the previously two systems, denoted as SPM-A in figure 1.6(a) constructed by a periodic array of pillar A and as SPM-B in figure 1.6(b) constructed by a periodic array of pillar B. The parameters of pillar A are optimized to possess a low frequency band gap featuring the negative effective mass density and to ensure that the frequency of the torsional resonance of pillar B can fall into this band gap.

Regarding SPM-A configuration, the diameter and the height of the pillar A were chosen to be d = 80μm and h = 200μm. The corresponding band structure is displayed in figure 1.6(d). It can be seen that a low frequency band gap occurs in between 5.19MHz and 5.47MHz. As concluded in Sec. 1.2.2, it should be accredited to the negative effective mass density generated by the combination of the bending and the compressional resonances of pillar A. The local resonances can also be evidenced by the flatness of the

dispersion curves around the lower limit of the band gap and the eigenmodes at point M of the BZ, labelled as points C and D in figure 1.6(d). The deformation and displacement fields of the eigenmodes displayed in figure 1.6(h) illustrate that they are the second-order bending resonance and the first-order compressional resonance of pillar A. Further, the effective mass density matrix components are evaluated and their evolution against the excitation frequency is shown in figure 1.6(e). Both components turn negative in between 5.32MHz and 5.49MHz which is in good agreement with the forbidden band that goes from 5.19MHz to 5.47MHz with a small discrepancy of about 2.5% at the lower edge. With regard to SPM-B configuration, the parameters of pillar B are the same as the one proposed in Sec. 1.2.3. For comparison, the band structure is displayed in figure 1.6(f). The eigenmodes of the unit cell at points E, F and G are displayed in figure 1.6(h). Afterwards, to build a double-sided pillared metamaterial, we attach pillar A and pillar B to the top and the bottom sides of a thin plate respectively as shown in figure 1.6(c). Clearly, the merged structure is asymmetric about the mid-plane of the plate. To validate this approach to obtain the doubly negative property, we have computed the band structure of this asymmetric double-sided pillared metamaterial (ADPM). The dispersion curves are displayed in figure 1.6(g). As expected, an isolated negative-slope branch (red) appears in between 5.28MHz and 5.35MHz. In addition, we display the eigenmodes of the unit cell at some points (labelled from point C' to point G' in order) in figure 1.6(h).

Comparing the band structures of these three kinds of pillared metamaterials allows understanding the formation of this newly isolated branch. At point M of the BZ, the bending and the compressional modes (point C and point D) in figure 1.6(d) slightly shift to point C' and point D' in figure 1.6(g) upon attachment of pillar B to the bottom side of the thin plate. For both resonances, the displacement fields of ADPM displayed in figure 1.6(h) show that the deformation of pillar B is very small at the compressional resonance and even null at the bending resonance. This suggests that pillar B acts merely as an inert mass attached to the plate that simply shifts the resonant frequencies of pillar A. Accordingly, the frequency interval of the negative effective mass density generated by the resonances C' and D' of pillar A in ADPM also shifts and now appears in between 5.21MHz and 5.48MHz instead of 5.19MHz to 5.47MHz in SPM-A, but the overall mechanism leading to the negative effective mass density is the same for both pillared metamaterials.

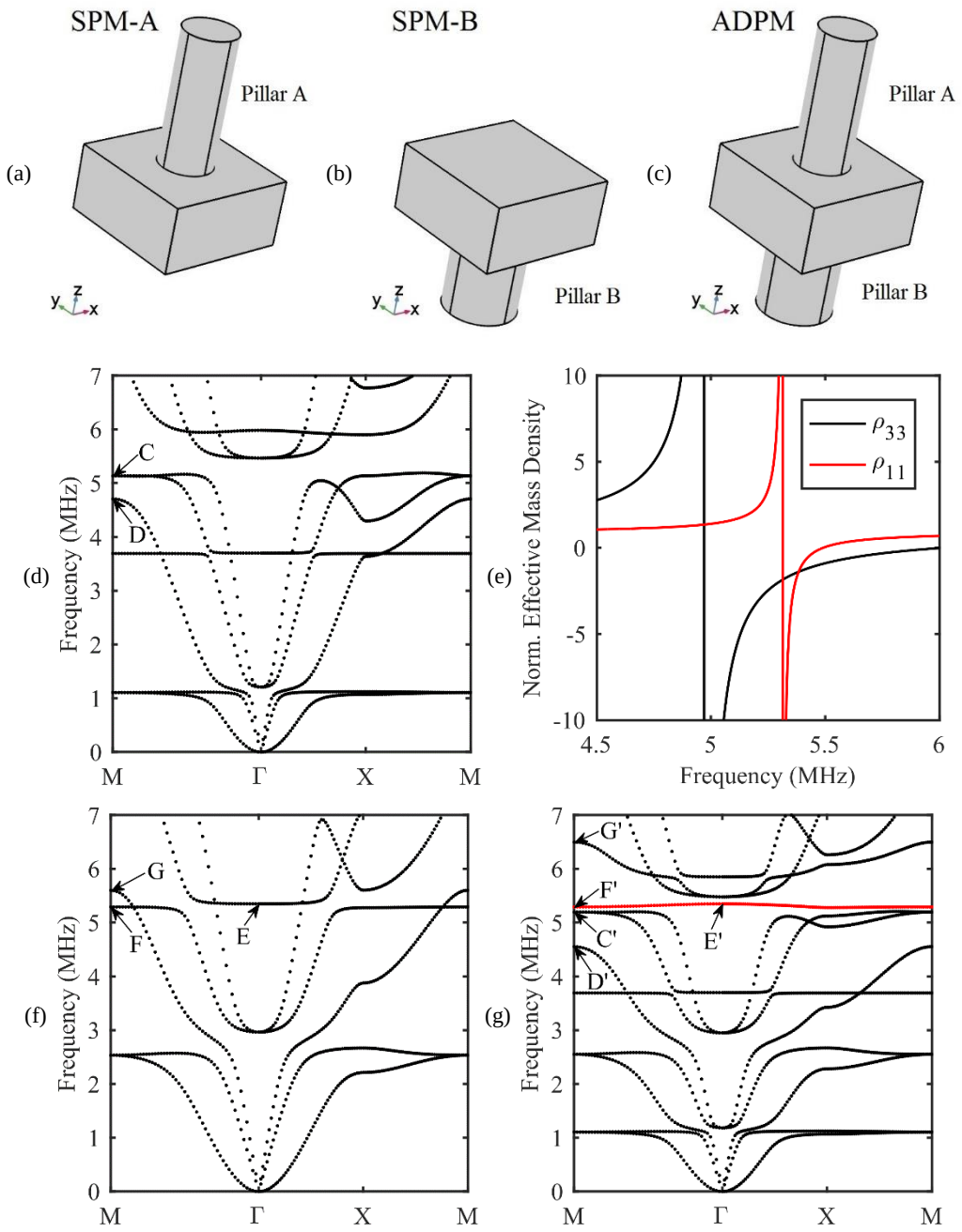
SPM-A
SPM-B
ADPM
(a)
(b)
(c)
Pillar A
Pillar B
Pillar A
Pillar B
(d)
(e)
(f)
(g)
Frequency (MHz)
Norm. Effective Mass Density
Frequency (MHz)
ρ_{33}
ρ_{11}
C
D'
G
F
E
G'
F'
C'
E'
D'
M
Γ
X
M

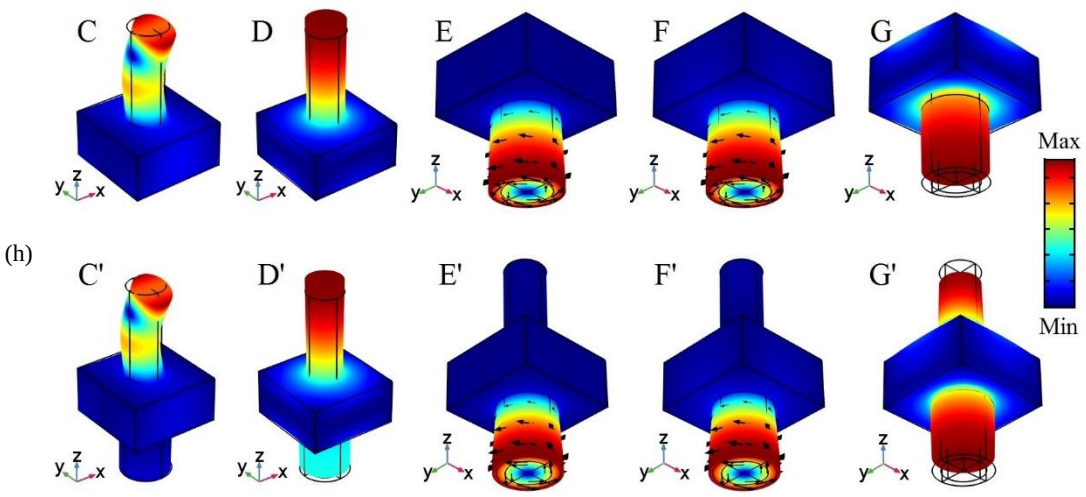

Figure 1.6: Elementary unit cells of (a) SPM-A, (b) SPM-B and (c) DPM and corresponding band structures of (d) SPM-A, (f) SPM-B and (g) ADPM. (e) Effective mass density matrix components ρ_{11} (red solid line) and ρ_{33} (black solid line) normalized to the mass density of steel as a function of the excitation frequency. (h) Eigenmodes of the unit cell at points labelled in panels (d), (f) and (g).

The situation becomes totally different when comparing the band structures of ADPM and SPM-B. In this case, appending pillar A to SPM-B does not summarize into a resonant frequency shift of pillar B. At point M of the BZ, the compressional resonance labelled as point G' influences both pillars in ADPM [see panel G' in figure 1.6(h)] and therefore the shift from point G (the compressional resonance of SPM-B) to point G' cannot be ascribed to an inert mass attached to the plate as before. Meanwhile, the eigenfrequencies at points labelled as E and F [see figure 1.6(f)] remain unchanged because there is no coupling between the torsional vibration of pillar B and the bending and the compressional vibrations of pillar A. For a sake of consistency in the notations, these points are labelled as E' and F' in figure 1.6(g). As mentioned before, the effective shear modulus turns negative in the frequency interval between these two points. Therefore, both the negative effective mass density and shear modulus are achieved in this frequency interval which perfectly explains the occurrence of the propagative branch with a negative-slope in figure 1.6(g).

However, it should not be assumed from the eigenmodes of ADPM at points E' and F' that the torsional resonance of pillar B merely induces the negative effective shear modulus. As proof of this, figure 1.7(a) displays the eigenmode of the unit cell at the wave vector in the middle of ΓM boundary. While pillar B vibrates on its torsional mode, the motion of pillar A clearly corresponds to the bending resonance. Moreover, the top view depicted in the right panel reveals that the vibration lies in the plane perpendicular to the direction of propagation, which suggests that the doubly negative branch is SH polarized. This is further confirmed by the eigenmode at the wave vector in the middle of ΓX boundary in figure 1.7(b). Again, pillar A vibrates on its bending mode with a motion lying in the plane perpendicular to the direction of

propagation, as better viewed in the top view displayed in the right panel of figure 1.7(b), confirming that the double-negative branch is SH polarized. At this point, the amplitude of the torsional motion of pillar B is relatively small but non-null from which it can be concluded that both the bending mode of pillar A and the torsional mode of pillar B contribute to the formation of the double-negative branch.

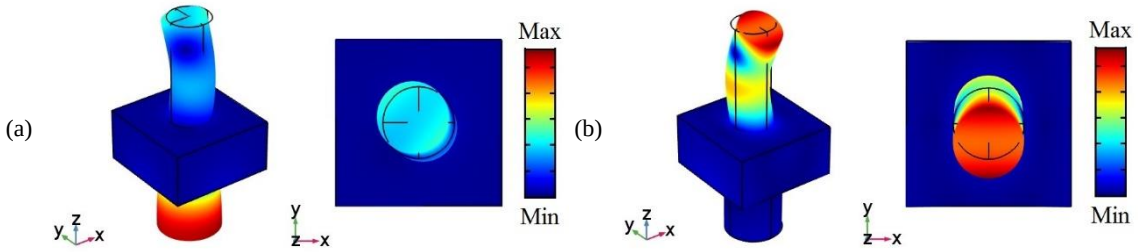

Figure 1.7: Eigenmodes of ADPM unit cell at the wave vectors in the middle of ΓM (a) and ΓX (b) boundaries. Their top views are shown in the corresponding right panels.

1.3.2 Enlargement of the double-negative branch

We have demonstrated in Sec. 1.3.1 the occurrence of the doubly negative property that ranges from 5.28MHz to 5.35MHz in the proposed ADPM. In some specific applications and devices where a high selectivity in frequency is a requirement, this narrow interval may be an advantage but there are other applications where a broad band is preferable instead. To establish that the pillared metamaterials we have investigated in this work are able to meet such contradictory requirements, we have improved the design of the structure by including holes drilled throughout the plate to enlarge the doubly negative branch. Actually, Bilal *et al.* [77] have reported that the subwavelength band gaps can be increased by a factor of four in a perforated plate. Such local resonance amplification phenomenon is sometimes called the trampoline effect. In this section, we examine the impact of these holes on the width of the double-negative branch. Four through-holes with a diameter of 60µm are drilled at the four corners of the square lattice unit cell of the proposed ADPM. The band structure denoted as the red dotted lines is displayed in figure 1.8(a). For comparison, the band structure of ADPM without perforated hole is also shown in figure 1.8(a) as the black dotted lines. Both band structures share almost the same profile. In particular, the doubly negative branch along ΓX direction is almost not affected by the holes. Along ΓM direction, the eigenfrequency at point F' decreases to point F" because of the softening of the plate, logically leading to the increase of the width of the double-negative branch by a factor of 2.3 where the effective shear modulus is negative that extends now from 5.19MHz to 5.35MHz. Figure 1.8(b) plots the band structure when the diameter of the holes is enlarged up to 100µm. Both the eigenfrequencies of the bending and the compressional modes significantly shift downwards. The frequency of the eigenmode at point F' is strongly impacted and moves down to point F"' and the doubly negative property occurs now in between 5.07MHz and 5.33MHz allowing for a broader

propagative band (the width is increased by a factor of 3.7). Note that this approach also applies to the chiral configuration described in Sec. 1.3.5.

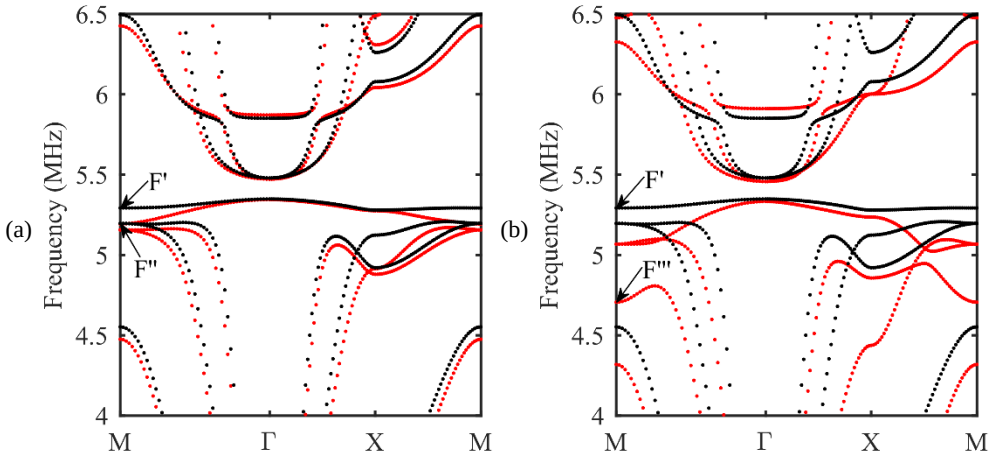

Figure 1.8: Band structures (red dotted lines) after introducing perforated holes with the diameter 60μm (a) and 100μm (b) at the four corners of the square lattice unit cell of the proposed ADPM. The band structure of ADPM without perforated holes is shown as the black dotted lines for reference.

1.3.3 Polarization-filter behavior

We have demonstrated in Sec. 1.3.1 that the isolated propagative branch is SH polarized. Therefore, it is quite natural to investigate the transmission of an incident SH_0 mode through a structure of finite dimension along one direction of space and in turn, the coupling of this wave with both the torsional and the bending modes of the pillars. To this end, we have considered a two-dimensional metamaterial plate consisting of nine unit cells along the *x*-axis and infinite along the *y*-axis [figure 1.9(a)]. Periodic condition $k_y = 0$ is applied to investigate the propagation along ΓX direction. Two perfectly matched layers (with the length set to be two times the wavelength of S_0 Lamb mode) are involved at two ends to eliminate the reflected waves from the boundaries. The incident wave was launched at a distance of 1000μm away from the left edge and impinged the array of resonators at normal incidence. The transmission coefficient, defined as the ratio of the displacement component along the *y*-axis of the transmitted wave to the one of the plate without pillars is shown in figure 1.9(b) as the black solid line. This coefficient is almost equal to unity in the frequency interval where the doubly negative property occurs, which confirms that both the bending motion of pillar A and the torsional vibration of pillar B are efficiently excited. For comparison, figure 1.9(b) displays as the red solid line the transmission coefficient of an incident A_0 Lamb wave normalized to the out-of-plane displacement component of the incident wave. In the frequency interval where the doubly negative property occurs, the transmission coefficient is equal to zero. Symmetry considerations well explain this result. Actually, both the deformation caused by the elastic wave and the geometry of the structure are symmetric about the plane (*x, z*). This makes it impossible the coupling with the bending mode

of pillar A in the plane perpendicular to the direction of propagation and thus the double-negative branch turns to be a band gap. Similar conclusions may be drawn for an incident S_0 Lamb wave, even though its in-plane displacement component is larger than its antisymmetric counterpart. It should be noted to conclude this section that one can take advantage of the different behaviors along ΓX direction observed for incident SH_0 and A_0 or S_0 Lamb waves to conceive new polarization filter devices based on the geometry of the proposed ADPM.

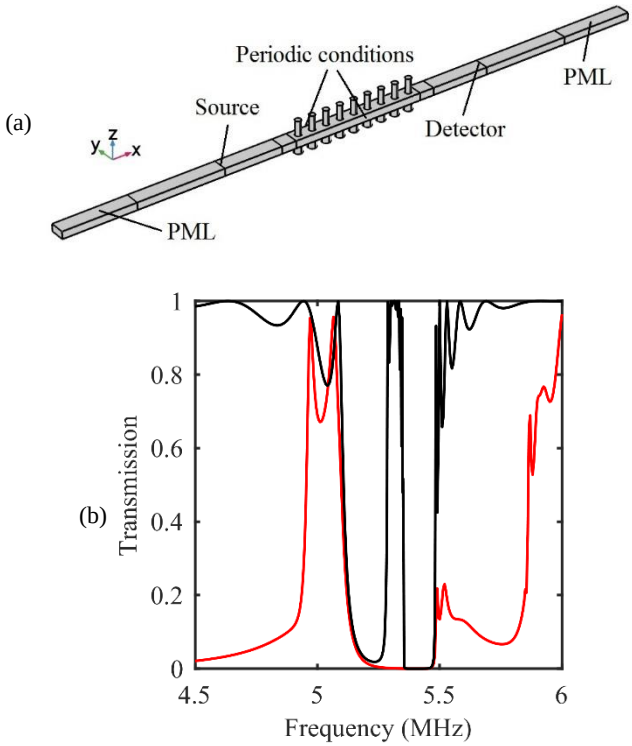

Figure 1.9: (a) Finite element model to investigate the transmission of an incident SH_0 and A_0 Lamb waves along ΓX direction. (b) Transmission spectra of incident SH_0 (black) and A_0 Lamb waves (red) propagating across the supercell in (a).

1.3.4 Mode conversion phenomenon

In Ref. [82], Jin *et al.* have established that a pillar reemits Lamb waves when it is excited on either the bending or the compressional eigenmode. Therefore, one must question the property of the transmitted waves in figure 1.9(a) and investigate on the possible mode conversion resulting from the interactions of the pillars at resonances with the incident SH_0 wave propagating in the plate. The analysis is based on the fact that both S_0 and A_0 modes have the out-of-plane displacement component, contrary to SH_0 mode that is in-plane polarized. The computation is performed for the propagation along different directions in the first irreducible BZ.

When the propagation is along ΓX direction at a frequency in the double-negative branch (*i.e.* k_y = 0 and $\omega/2\pi$ = 5.33MHz), the out-of-plane displacement component u_z is null, within the computation accuracy, and only u_y has a measurable value in the transmitted field. Let us note here that the mode conversion cannot occur for the propagation along this direction since, as shown above, the bending vibration of pillar A lies in the plane (*y*, *z*) in that case. Therefore, the wave vector of the reemitted wave is along the *y*-axis which is why the displacement field in the unstructured area downstream the pillars does not feature any out-of-plane displacement component. In contrast, when the wave vector slightly deviates from ΓX direction and has a non-null component k_y, the out-of-plane displacement component comes out in the transmitted field. For instance, when $k_y = 0.05\pi/a$, the amplitude normalized to the amplitude of an incident SH_0 wave at k_y = 0 is $u_z/U_y = 0.08$ which suggests the occurrence of A_0 and/or S_0 modes in the transmitted field. Accordingly, the normalization of the amplitude of the in-plane displacement components u_x and u_y is $u_x/U_y = 0.12$ and $u_y/U_y = 0.98$. This ratio goes up to $u_z/U_y = 0.29$, $u_x/U_y = 0.41$ and $u_y/U_y = 0.75$ when $k_y = 0.2\pi/a$. An efficient way to identify the exact nature of the modes in the transmitted field is to compute their dispersion $\mathbf{k}(\omega)$ for frequencies in the double-negative branch. To this end, an incident SH_0 wave with $k_y = 0.2\pi/a$ and a frequency in the range where the doubly negative property occurs, is excited in front of the structure; both the components u_y and u_z of the displacement field are then computed at 256 different positions along the direction of propagation separated by 50µm from one another, downstream the pillars. The amplitude against the magnitude of the wave vector **k** is deduced from the spatial Fourier transform of the data. The results for u_x and u_z, normalized to the amplitude of an incident SH_0 wave, are displayed in figure 1.10(a) and figure 1.10(b) respectively. The peak at k = 0.01µm^{-1} in figure 1.10(a) evidently corresponds to SH_0 mode transmitted through the periodic structure. The other two branches appear at the wave vectors of k = 6.5×10^{-3}µm^{-1} and k = 17.6×10^{-3}µm^{-1}. These branches correspond to S_0 and A_0 modes respectively which clearly demonstrates that the mode conversion towards both A_0 and S_0 modes occurs during the propagation of SH_0 mode through the structure when the wave vector deviates from ΓX direction. In figure 1.10(b), SH_0 mode disappears because it does not contain the out-of-plane displacement component and the emergence of A_0 and S_0 modes confirm the occurrence of the mode conversion again.

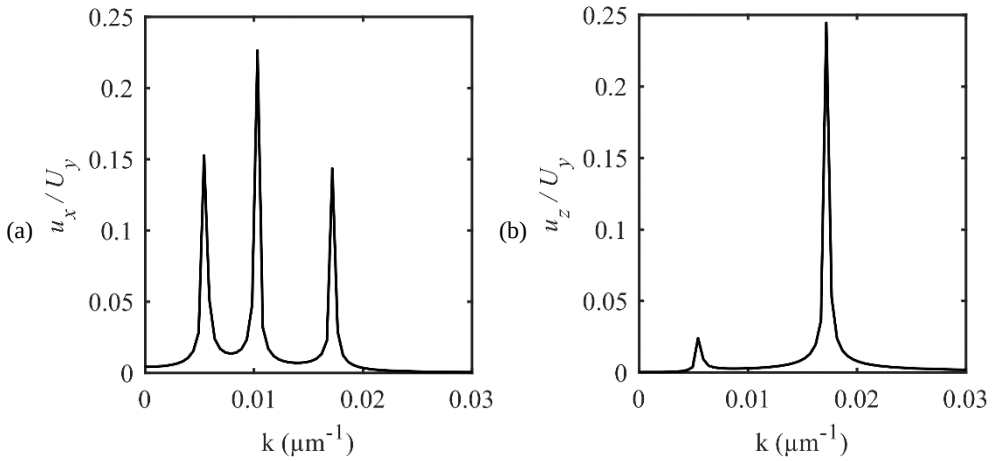

Figure 1.10: Fourier spectrum of the displacement components along the *x*-axis (a) and the *z*-axis (b) of the transmitted wave at the frequencies inside the double-negative branch.

1.3.5 Pillared metamaterial with chirality

The preceding analysis in Sec. 1.3.3 unambiguously demonstrates that along ΓX direction the doubly negative property can be excited with an incident SH_0 mode whereas most of the applications proposed so far rely on the dispersive properties of A_0 or S_0 mode. This raises the issue of how to efficiently and simultaneously excite both the bending resonance of pillar A and the torsional mode of pillar B with A_0 or S_0 mode. The main difficulty comes from the excitation of the torsional motion of pillar B. Once the torsional vibration of pillar B is excited, then the local shear deformation in the plate can easily excite the bending vibration of pillar A in the perpendicular plane.

An achievable solution to address this problem is to introduce the chirality [93,94] to pillar B in order to break the symmetry of the unit cell. As a consequence, it is expected that the propagation of the waves in the plate results in an asymmetric deformation in the surrounding area of the pillar, thus should easily lead to the torsional vibration especially when the frequency of the wave is close to the one of the torsional eigenmode. Both the cross section and the side view of a chiral pillar fulfilling this requirement are sketched in figure 1.11(a). Eight flanks equally spaced in azimuth with a length l = 60μm and a width w = 10μm are inserted along a solid cylinder with the diameter d = 100μm and the height h = 105μm. A twist angle θ = 45° in the anticlockwise direction is further applied to each flanks, as shown in the bottom panel of figure 1.11(a). The band structure of this chiral double-sided pillared metamaterial (CDPM) is displayed as the red dotted lines in figure 1.11(b) together with the band structure of ADPM which is included merely for comparison as the black dotted lines. The band structure of CDPM has a similar profile as the one of ADPM. The doubly negative branch goes from 5.37MHz to 5.41MHz which is slightly different from ADPM where the doubly negative branch goes from 5.28MHz to 5.35MHz. The eigenmodes at points labelled as L, N, and P in figure 1.11(b) that correspond respectively to the bending and the compressional resonances of

pillar A and to the torsional resonance of pillar B, are illustrated in figure 1.11(d). Comparing these displacement fields to their counterparts in ADPM [see the displacement fields at points C', D', E' in the lower panel of figure 1.6(h)] indicates that the eigenmodes of the unit cell in the frequency domain of interest are conserved when introducing chirality in pillar B.

To further point out the efficiency of the chirality to excite the torsional vibration, we show as the red solid line in figure 1.11(c) the transmission spectrum of an incident A_0 mode propagating through the supercell put forward in figure 1.9(a) replaced the chiral pillar B on the bottom side of the plate. A transmission coefficient of about 0.25 is obtained in the frequency range where the doubly negative property occurs thanks to the combination of the bending vibration of pillar A and the torsional vibration of chiral pillar B. This result must be compared with the transmission spectrum of A_0 mode which is null inside the double-negative branch in the absence of chirality [see the red solid line in figure 1.9(b)] since the torsional resonance could not be excited in that case.

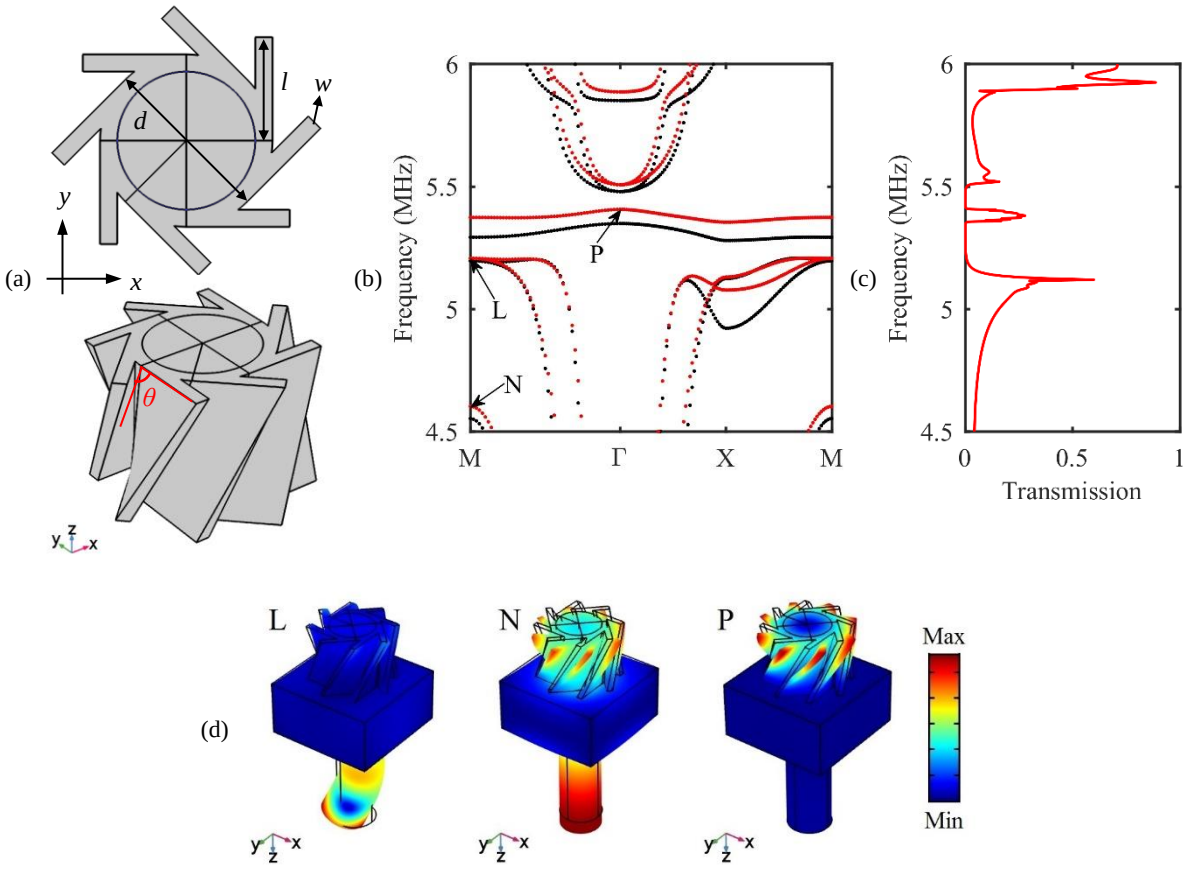

Figure 1.11: (a) Representative profile of the chiral pillar B. (b) Band structure of CDPM (red dotted lines) and ADPM (black dotted lines). (c) Transmission spectrum of an incident A_0 mode propagating across the supercell shown in figure 1.9(a) with the chiral pillar B instead. (d) Eigenmodes of the unit cell at points indicated in (b).

1.4 Doubly negative property in a symmetric double-sided pillared metamaterial

It has been evidenced in Sec. 1.3 that the doubly negative property can be obtained by assembling two different single-sided pillared metamaterials. One features the negative effective mass density that results from the combination of the bending and the compressional resonances and the other one generates the negative shear modulus that comes from the torsional mode. What's more, we need to ensure that the eigenfrequency of the torsional mode of one pillar can fall inside the low frequency band gap induced by the other pillar. And to meet such requirement, these two pillars usually have different dimensions. Thus, it might raise the question that what would happen in a symmetric double-sided pillar metamaterial that can be recognized as a more specific case. In this section, we are going to discuss a symmetric double-sided pillared metamaterial that enables the enlargement of the width of the low frequency band gap as reported in Refs. [76,83,84,95]. We show that the doubly negative property can be obtained through an appropriate choice of the dimensions of the pillars and the plate.

1.4.1 Occurrence of isolated negative-slope branch

The elementary unit cell of the symmetric double-sided pillared metamaterial is shown in figure 1.12(a). Two identical pillars are symmetrically arranged on both sides of the plate. The geometric parameters of the unit cell are the same as those of the single-sided pillared metamaterial in Sec. 1.2.2. The corresponding band structure is shown in figure 1.12(b). In contrast to the band structure of the single-sided pillared metamaterial displayed in figure 1.1(b), an isolated propagative negative-slope branch arises inside the complete band gap that opens in between 3.25MHz and 3.76MHz. This is almost twice the width of the band gap obtained in the single-sided pillared metamaterial. This enlargement is due to the strong coupling between the resonances of the double-sided pillars and Lamb waves propagating in the plate [76].

The isolated branch in between 3.53MHz and 3.57MHz divides the band gap into two narrower ones ranging from 3.25MHz to 3.53MHz and from 3.57MHz to 3.76MHz respectively. A zoomed view of the isolated branch is displayed in the inset. The negative slope of this branch throughout the first irreducible BZ cannot be afforded to a band folding effect and rather suggests simultaneous negative effective mass density and modulus resulting from the local resonances of the pillars. In support of this argument, we show in figure 1.12(c) the displacement field at two characteristic points in this branch. At point Γ of the BZ [point D in the inset of figure 1.12(b)] the displacement field clearly corresponds to a symmetric compressional mode of the double-sided pillars [left panel in figure 1.12(c)] whereas the motion of the double-sided pillars at middle point between Γ and X is a symmetric bending mode [right panel in figure 1.12(c)]. We show in the following that the former is responsible for the negative effective Young's modulus whereas the latter, similar to the single-pillared metamaterial, leads to the negative effective mass density.

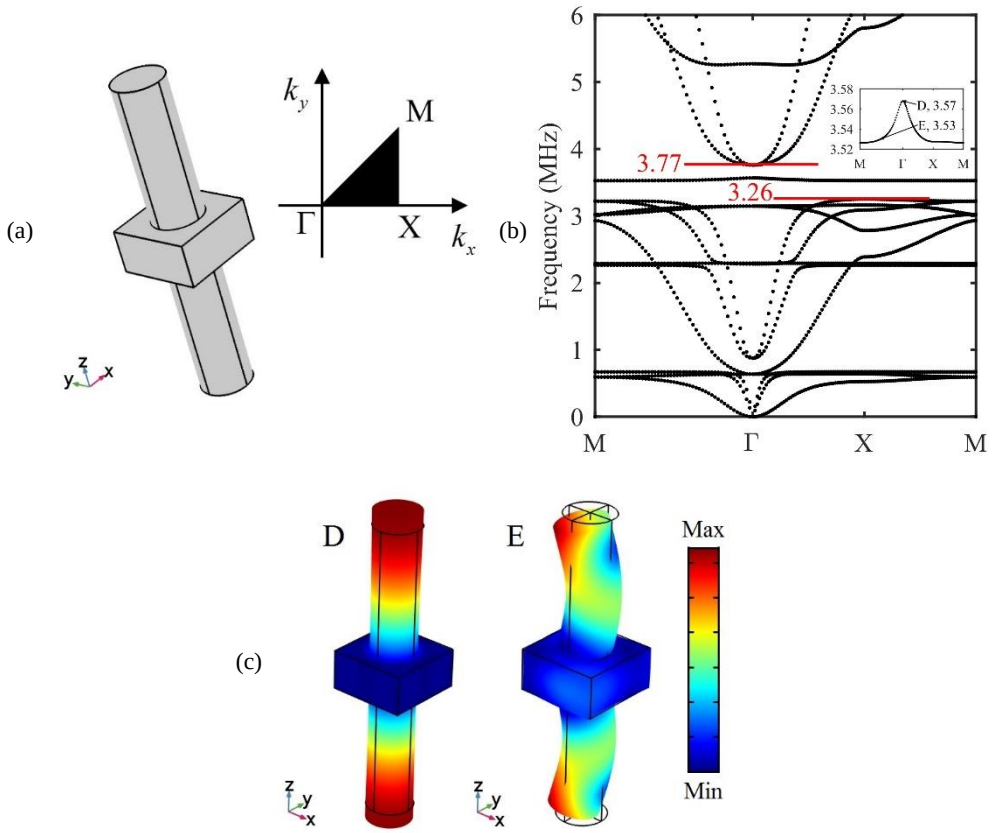

Figure 1.12: (a) Elementary unit cell of the symmetric double-sided pillared metamaterial and its first irreducible BZ of the square lattice. (b) Band structure in the low frequency range. Inset: enlargement of the isolated branch. (c) Eigenmodes of the unit cell at points denoted as D and E in the inset.

1.4.2 Formation of the double-negative branch

Before analyzing the formation of the isolated branch, it is necessary to identify the resonances in the frequency range of interest. This can be done by computing the displacement field in the unit cell upon the global harmonic excitation $(Ae^{i\omega t}, 0, 0)$. On the whole, there are four resonances involving a motion in the plane (x, z), namely: B_A (3.17MHz) is the second-order antisymmetric bending resonance; B_S (3.26MHz) is the second-order symmetric bending resonance; C_A (3.04MHz) is the first-order antisymmetric compressional resonance, and C_S (3.57MHz) is the first-order symmetric compressional resonance. The corresponding displacement fields are displayed in figure 1.13(a). Because of the squared symmetry of the unit cell one should also add to this list two bending resonances equivalent to modes B_S and B_A respectively, but involving motions along the y-axis.

As it is the case in the single-sided pillared metamaterial, the formation of the low frequency band gap should be the signature of the negative effective mass density that results in turn from the combination of the bending and the compressional resonances of the double-sided pillars. For verifying this hypothesis, the

same method as the one applied in Sec. 1.2.2 was implemented to calculate the effective mass density matrix against the excitation frequency. The normalized components ρ_{11} and ρ_{33} displayed in figure 1.13(b), highlight the role played by each resonance. Actually, at the frequencies of B_A and C_S the changes in ρ_{11} and ρ_{33} are very sharp and cannot generate the negative effective mass density. On the contrary, both ρ_{11} and ρ_{33} turn negative at the frequencies of B_S and C_A which thus directly relate to the negative effective mass density. The simplified traction forces and moments modeling the interaction between the pillars and the plate at the resonances provide a comprehensive understanding of these divergent behaviors. Both are schematically described in figure 1.13(a) by the black and red arrows respectively. At B_A resonance, the moments induced by the two identical pillars are the same whereas the traction forces are pointing in opposite directions and hence the resultant force becomes zero. Although the resultant moment is not equal to zero, it does not couple with the motion in the plate and this bending resonance cannot induce the negative effective mass density: ρ_{11} and ρ_{22} do not turn negative around the antisymmetric bending resonance, except at the exact resonant frequency. The reverse phenomenon occurs at B_S resonance. Actually at this frequency the resultant moment is equal to zero, but not the resultant traction force that consequently contributes to the negative value of ρ_{11} in between 3.26MHz and 3.77MHz. Owing to the symmetry, ρ_{22} gets also negative in the same frequency interval.

The same argument applies for both compressional modes. Indeed, the resultant force at the frequency of C_S (*i.e.* 3.57MHz) is null and this mode does not trigger the negative values of the component ρ_{33}. Conversely, the situation at the frequency of C_A is similar to the one observed at the compressional resonance in the single-sided pillared metamaterial: the axial forces in the pillars combine and ρ_{33} takes the negative values in the range from 3.04MHz to 5.29MHz.

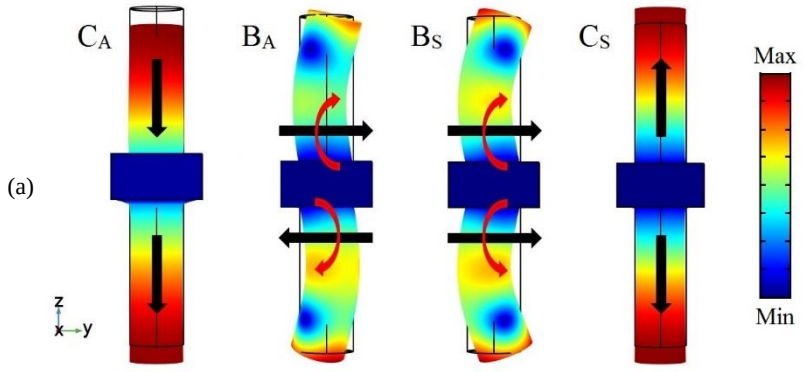

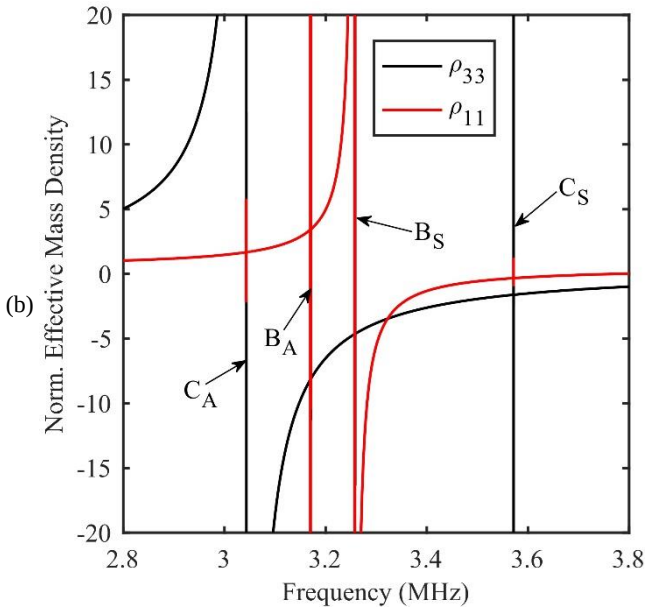

Figure 1.13: (a) Eigenmodes of the unit cell at the four representative resonance frequencies upon excitation $(Ae^{i\omega t},0,0)$. (b) Effective mass density matrix components ρ_{11} (red) and ρ_{33} (black) normalized to the mass density of steel as a function of the excitation frequency.

Overall, the negative effective mass density is achieved at any frequency in the frequency interval ranging from 3.26MHz to 3.77MHz, including the vibrational modes on the isolated branch therein, where ρ_{11}, ρ_{22} and ρ_{33} are all negative as shown in figure 1.13(b). Both these values exactly match the limits of the low frequency band gap displayed in figure 1.12(b) and further highlighted with the red solid lines in figure 1.12(b).

Although the isolated branch is relatively flat, especially along XM direction of the BZ, the group velocity is non-null and the propagation of the elastic energy at the corresponding frequencies is allowed. Therefore, the dynamic modulus is necessarily negative for any vibrational mode on this branch. Figure 1.13(b) clearly demonstrates that the narrow interval around 3.57MHz where propagation is allowed corresponds to the first-order symmetric compressional resonance C_S which is thus causing the negative effective modulus and in turn the doubly negative property. However, it should be noticed that this resonance involves a purely out-of-plane motion only at points Γ, X and M of the BZ. In between these main corners, the in-plane motions contribute also to the deformation of the pillars, as it can be observed in figure 1.12(c), the eigenmode at point E.

Similar to the analytical study developed above to explain the negative effective mass density achieved in the single-sided pillared metamaterial, one can model the symmetric compressional vibration of the double-sided pillared system as two identical mass-spring subsystems, each featuring a mass m and a stiffness k_C,

vibrating in phase as shown in figure 1.14(a). In this figure, e is the thickness of the plate; $A_x = e \times a$ and $A_z = a^2$ are the areas of boundaries parallel to the planes (y, z) and (x, y) respectively. To calculate the vertical traction forces exerted on the plate when the pillars are on a vertical motion, let us consider two harmonic tension forces F_x with the same amplitude, both applied along the x-axis on the lateral boundaries parallel to the plane (y, z) and pointing in opposite directions [figure 1.14(b)]. Displacements $\pm x_1$ of the lateral boundaries, $\pm z_1$ of the free surfaces and $\pm z_2$ of the mass m result from the forces F_x [figure 1.14(b)]. It is expected that the harmonic deformation induced by F_x allows to excite the resonances of the mass-spring subsystems if the frequency is properly tuned.

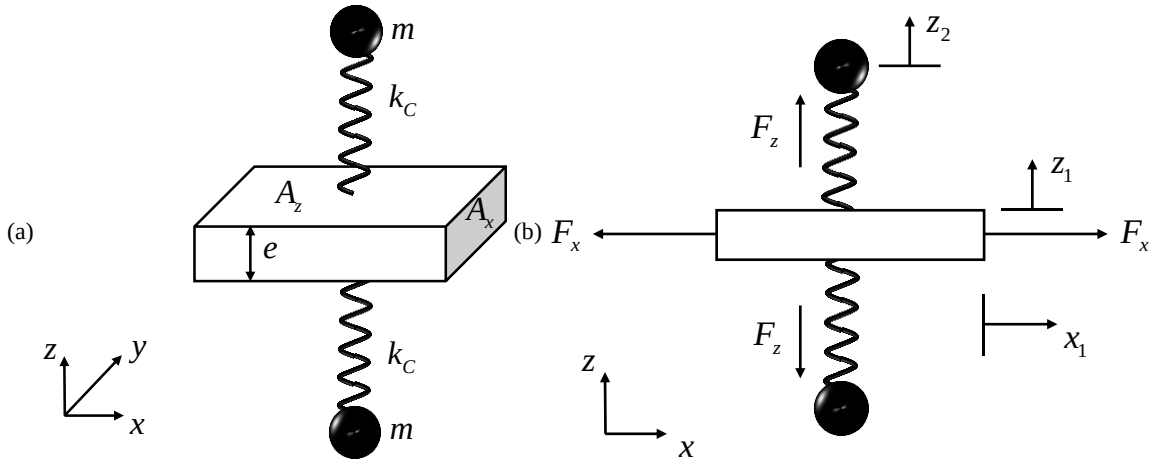

Figure 1.14: (a) Schematic model of the unit cell with two identical mass-spring subsystems. (b) Side view of the unit cell and notations of the displacements induced by the forces applied along the x-axis.

To simplify the derivation of the effective Young's modulus E_{eff} of the unit cell, we assume that the reactive forces F_z caused by the vibration of the mass-spring subsystems are uniformly distributed on the matrix plate. Under this hypothesis, the dynamic stress tensor σ and strain tensor ε in the plate submitted to a harmonic excitation are given by Hooke's law and can be expressed as:

$$\begin{cases} \sigma_x = \dfrac{F_x}{A_x} \\ \sigma_y = 0 \\ \sigma_z = \dfrac{F_z}{A_z} \\ \varepsilon_x = \dfrac{2x_1}{a} = \dfrac{1}{E}\left(\sigma_x - \nu\sigma_z\right) \\ \varepsilon_z = \dfrac{2z_1}{e} = \dfrac{1}{E}\left(\sigma_z - \nu\sigma_x\right) \end{cases} . \qquad (1.8)$$

As previously, E is the Young's modulus and ν the Poisson's ratio of the plate. On the other hand, the equation of motion of the mass-spring subsystem is:

$$m\frac{\partial^2 z_2}{\partial t^2} = -F_z = -k_C\left(z_2 - z_1\right). \tag{1.9}$$

By combining equations (1.8) and (1.9) one can easily obtain:

$$\frac{F_x}{A_x} = E\left(1 - \frac{\nu^2}{1 + \frac{k_M}{k_C}\frac{\omega^2 - \omega_0^2}{\omega^2}}\right)^{-1}\frac{2x_1}{a}, \tag{1.10}$$

where $\omega_0 = \left(k_C/m\right)^{1/2}$ is the natural frequency of the mass-spring subsystem, $k_M = 2EA_z/e$ is the effective stiffness of the plate.

Equation (1.10) is nothing else but the Hook's law applied to an effective medium whose effective Young's modulus $E_{eff} = E\left(1 - \frac{\nu^2}{1 + \frac{1}{\eta}\frac{\omega^2 - \omega_0^2}{\omega^2}}\right)^{-1}$ depends on the frequency $\omega/2\pi$ and takes into account the internal motions of the unit cell through the parameters $\eta = k_C/k_M$ and ω_0.

The effective Young's modulus E_{eff} can also be written evidently as:

$$E_{eff} = E\left(1 + \frac{\nu^2\omega^2}{\left(1 - \nu^2 + 1/\eta\right)\omega^2 - 1/\eta\,\omega_0^2}\right). \tag{1.11}$$

The effective Young's modulus diverges if $\omega = \omega_0\left(\frac{1}{\left(1-\nu^2\right)\eta + 1}\right)^{1/2}$, which thus must be regarded as the resonant frequency of the effective medium. It is interesting to notice here that the resonant frequency of the effective medium is not that of the mass-spring subsystem. Furthermore, $E_{eff} = 0$ when $\omega = \omega_0\left(1/\eta + 1\right)^{1/2}$ and E_{eff} is negative if:

$$\omega_0\left(\frac{1}{\eta+1}\right)^{1/2} < \omega < \omega_0\left(\frac{1}{\left(1-\nu^2\right)\eta+1}\right)^{1/2}. \tag{1.12}$$

This interval would become broader when the Poisson's ratio *v* increases. Although this simplified model hardly allows predicting the position and width of the isolated double-negative branch, it provides an intuitive comprehension of the occurrence of the negative effective Young's modulus and in turn the doubly negative property in the symmetric double-sided pillared metamaterials.

1.4.3 Evolution of the double-negative branch against the geometric parameters

Being the consequence of a resonant phenomenon, the double-negative branch of the proposed structure is relatively narrow which may be a drawback for some applications. However, the width of the frequency band where the doubly negative property occurs can be increased through a proper choice of the geometrical parameters of the unit cell [82]. Here, we investigate the influence of the height and the diameter of the pillars as well as the thickness of the plate, on both the width of the forbidden band gap and the negative-slope branch.

Both figure 1.15(a) and (b) display the effect of the dimensions of the pillars on both the low frequency band gap and the negative-slope branch. Increasing the height of the pillar leads to the decrease of the central frequency of the band gap, as well as to the decrease of the range where the doubly negative property occurs. This should be related to the decrease of the compressional resonance frequency for increasing the height of the pillars [96]. Moreover, the lower part of the band gap broadens as the height of the pillars increases. In contrast, the propagative branch moves closer to the upper limit of the band gap as the height of the pillars increases leading to the closure of the upper part when the height of each pillar is more than about 350µm. Remembering that the effective mass density tends towards zero while keeping negative values when the frequency approaches the upper limit of the band gap [see figure 1.13(b)], it is expected that this structure may behave as a zero-index elastic metamaterial. Actually, in that case the phase velocity in the metamaterial tends to infinity and therefore the refractive index (*i.e.* ratio of the velocity in the background to the velocity in the metamaterial) goes to zero. This point is further developed below.

On the other hand, the bending resonance is very sensitive to the diameter of the pillars [82] and consequently this parameter has a large impact on the width of the band gap that broadens as the diameter increases [figure 1.15(b)]. However, the width of the double-negative branch is very little affected by this parameter and remains equal to about 8.5% of the width of the forbidden band whatever the diameter of the pillars is.

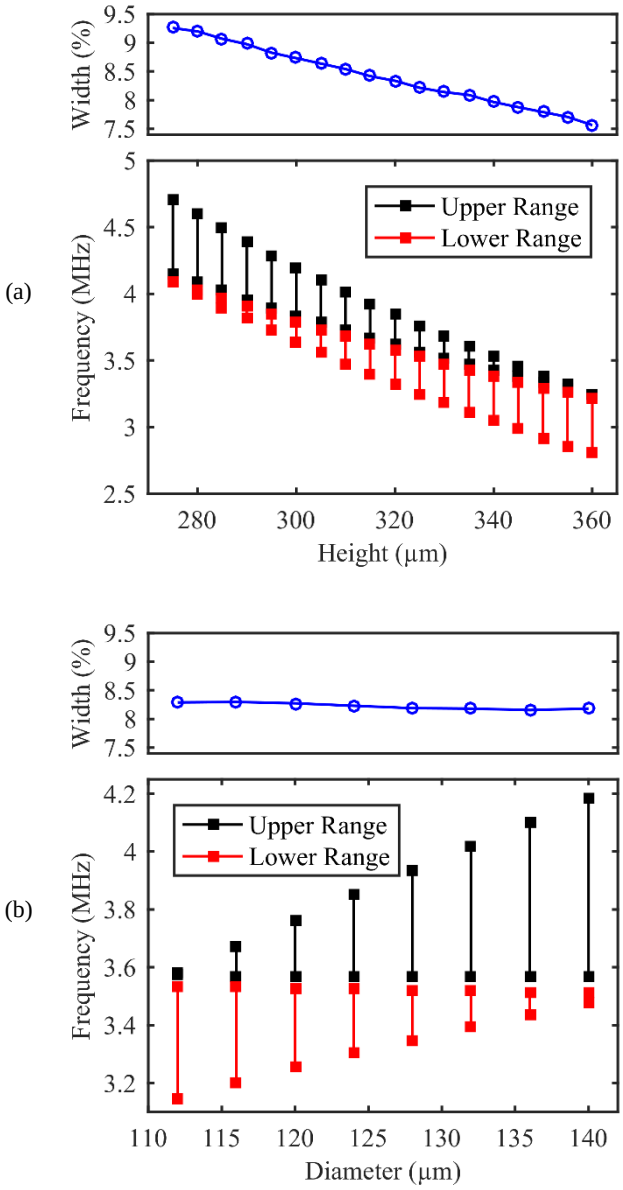

Figure 1.15: Edges of the band gap (lower panel) and relative width of the double-negative branch (upper panel) against (a) the height and (b) the diameter of the pillars. The black (red) solid lines stand for the upper (lower) part of the band gap. In both panels the blue curve is the relative width of the band where the doubly negative property occurs.

However, the parameter that most efficiently affects the width of both the band gap and the double-negative branch is the thickness of the plate (figure 1.16). Actually, both parts of the band gap slightly decrease as the thickness increases while at the same time the width $\Delta\omega$ of the double-negative branch linearly increases when increasing the thickness of the plate. The relative width of the frequency interval exhibiting the negative effective Young's modulus reaches the maximum value of ~20% of the total band gap when e = 180µm.

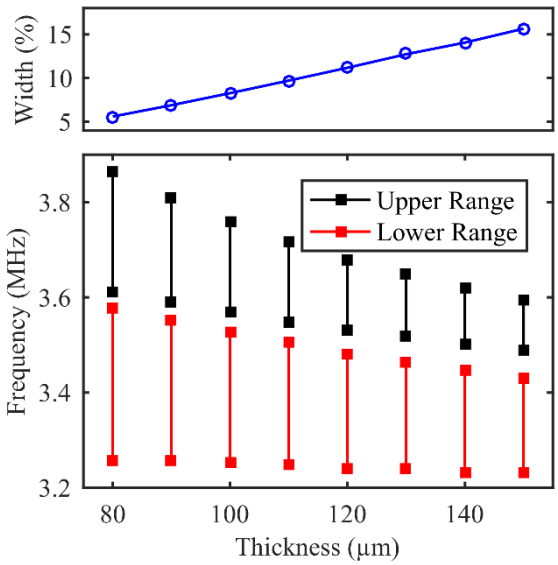

Figure 1.16: Edges of the band gap (lower panel) and relative width of the double-negative branch (upper panel) against the thickness of the plate. The black (resp. red) solid lines stand for the upper (resp. lower) part of the band gap. The blue curve is the relative width of the branch where the doubly negative property occurs.

A simple model allows to summarize these results. Actually, at C_S resonance there is almost no displacement at the foot of the pillars [see figure 1.13(a)] that can be modelled as a mass-spring system with a steady attachment point and for which the displacement on top of the pillar is proportional to the axial force. With these assumptions, Hooke's law leads to $k_C = \pi d^2 E / 4h$ and the ratio $\eta = k_C / k_M$ can be written as $\eta = \pi d^2 e / 8ha^2$. With the typical dimensions of the unit cell, η is always much less than unity and equation (1.12) can be expanded as:

$$\Delta\omega = \frac{\pi}{16} v^2 \left(E/\rho\right)^{1/2} \frac{d^2 e}{h^2 a^2}, \tag{1.13}$$

where we have used $\omega_0 = \left(k_C/m\right)^{1/2} = \left(E/\rho h^2\right)^{1/2}$. Equation (1.13) gives the full account of the behaviors displayed in figure 1.15 and figure 1.16.

Although relatively narrow even when it is maximum, the width of the doubly negative branch remains sufficient for an experimental validation based onto conventional techniques as for instance the excitation of Lamb waves with the interdigitated transducers (IDTs) on a piezoelectric film. Actually, in the frequency range that we have considered, elastic waves featuring a spectral purity δf better than the width of the negative effective Young's modulus band can be easily obtained with an IDT comprising only a few tens

pairs of electrodes, allowing in turn to tailor the transition from the single negative property to the doubly negative property. It is worth noting that our results are not specific to the MHz range and may be transposed to either the GHz or the kHz range by rescaling both the thickness of the plate and the lattice constant while keeping the ratio $\lambda/a = const$ (λ is the wavelength at the operating frequency) and adapting the dimensions of the pillars accordingly. The high frequency domain fits with nanostructures whose typical dimensions (thickness of the plate, high and diameter of the pillars, and lattice constant) are of a few micrometers or less, with the possible applications such as the vibration isolation of the sensitive components, the super-focusing, the high-resolution imaging, or the cloaking of elastic waves (see Sec. 1.5.2). At the other end of the scale, the symmetric double-sided pillared metamaterials with the typical dimensions in the millimeter range are excellent candidates for the noise reduction and filtering in the audio range. However, a narrow band is not necessarily a drawback and even it becomes an advantage for all applications and devices where a high selectivity in frequency is a requirement.

1.5 Applications of doubly negative property

1.5.1 Refraction at the outlet of a prism-shaped supercell

The theoretical prediction and experimental observation of the negative refraction of Lamb waves have been reported in both elastic phononic crystals [7,97,98] and metamaterials [21,23,24]. In the former case, the negative refraction relates to the periodicity and the resulting band folding and therefore the wavelength of the propagating wave is of the same order of magnitude as the lattice constant. In contrast, in an elastic metamaterial, the negative refraction is the direct consequence of simultaneously negative effective mass density and modulus (or stiffness) [21,23,24] and observing the phenomenon in the long wavelength limit provides further evidence of the doubly negative property.

For this purpose, we have investigated the refraction of an incident Lamb wave at the interface between a two-dimensional prism-shaped double-sided pillared metamaterial and the surrounding plate. The structure depicted in figure 1.17(a) consists of 120 unit cells arranged in a 45° isosceles triangle in a circular steel plate. The plate is surrounded by a perfectly matched layer to eliminate any reflections from the boundaries. The two perpendicular boundaries of the prism are set parallel to the lattice directions ΓX and XM. A line source of width 1600μm is placed 100μm away from the inlet interface perpendicularly to ΓX direction and the wave impinged the prism at normal incidence.

1.5.1.1 Asymmetric single-sided pillared metamaterial supercell

To demonstrate the doubly negative property in the asymmetric double-sided pillared metamaterial discussed in Sec. 1.3, an incident SH_0 wave was launched at the line source. After propagation along the *x*-

axis in the prism, the incident SH_0 wave was reflected at the outlet interface and propagated along the negative *y*-axis. Obviously, the reflected SH_0 wave can couple with the bending vibration of the pillars in the plane (*x*, *z*) which in turn allows for reemission of both A_0 and S_0 Lamb modes along the positive *x*-axis. Therefore, both these modes should be expected in the transmitted field. Two frequencies in close vicinity in the doubly negative branch were investigated, namely 5.31MHz and 5.33MHz [see figure 1.17(b)]. At these frequencies the wavelength of SH_0 mode is about 2.9 times the lattice constant while 4.9 and 1.8 times the lattice constant for S_0 and A_0 modes respectively. At frequency 5.33MHz, the out-of-plane displacement component u_z displayed in figure 1.18(a) confirms that the wave is negatively refracted at the outlet interface providing evidence that both the effective mass density and the shear modulus are simultaneously negative. More surprisingly, a large part of incident wave is positively refracted which cannot be explained without the help of the mode conversion illustrated above. To show this, we have analyzed the wave refraction in the reciprocal space [98–100] and computed the equifrequency contours (EFCs) in both the super cell and the surrounding plate. The approach consists of separately considering the symmetric and antisymmetric Lamb modes. Both modes feature the out-of-plane polarization and thus are necessarily present in the transmitted field shown in figure 1.18(a). Let us firstly consider A_0 mode. The EFCs of the supercell from 5.3MHz to 5.34MHz are displayed in figure 1.18(b) as the grey solid lines (highlighted as blue at frequency 5.33MHz). The red circle denotes the EFC at frequency 5.33MHz in the plate and the cyan dashed line represents the normal to the outlet interface. Noticing that the EFCs shrink as the frequency increases which confirms the negative group velocity in the double-negative branch. Owing to the conservation of the component of the wave vector parallel to the interface, it is straightforward to draw the wave vector of the refracted wave in the plate [red arrow $\mathbf{k_A}$ in figure 1.18(b)] as well as the group velocities in both the supercell (blue bold arrow $\mathbf{V_g}$) and the surrounding plate (red bold arrow $\mathbf{V_{gA}}$) which are normal to the EFCs. This simple scheme well accounts for the negative refracting angle $\theta(-) = 17.2°$ measured at the outlet interface of the supercell [see figure 1.18(a)] but not for the positive one. To explain the positive refraction, one must consider wave vector **k** in the supercell beyond the first BZ as depicted in figure 1.18(c). Within this scheme of refraction, the relationship between **k** and $\mathbf{V_g}$ inside the doubly negative branch remains satisfied, namely $\mathbf{k} \cdot \mathbf{V_g} < 0$. Moreover, the conservation of the wave vector parallel to the outlet interface leads to a transmitted wave with the positively refracted angle $\theta(+) = 75.7°$.

Regarding the refraction at frequency 5.31MHz, the mechanism is exactly the same and leads to both negatively and positively refracted A_0 Lamb modes as depicted in figure 1.19. The EFCs analysis results are displayed in figure 1.19(b) and (c) that correspond to the negative and positive refraction respectively. The only difference lying in the refracted angles as shown in figure 1.19 and table 1.1.

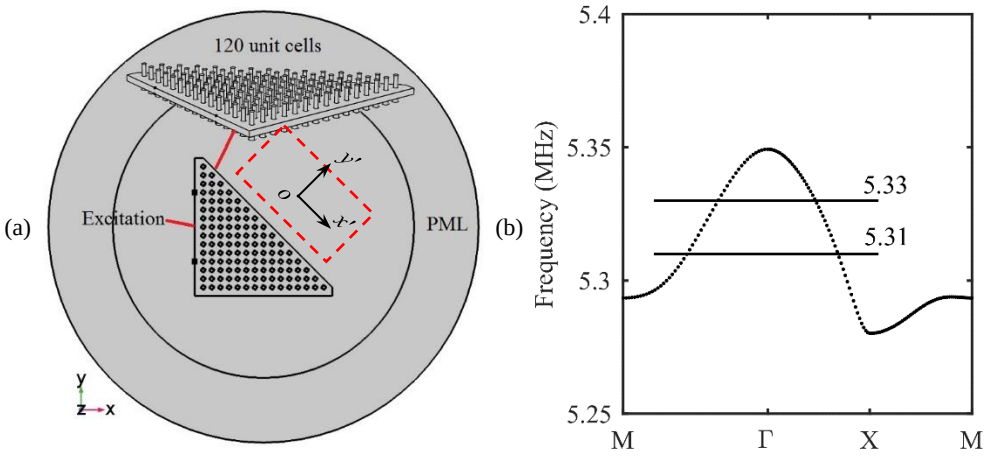

Figure 1.17: (a) Finite element model adopted to investigate the refraction at the outlet interface between a prism-shaped supercell and the surrounding plate. (b) Relative positions of the excitation frequencies inside the double-negative branch.

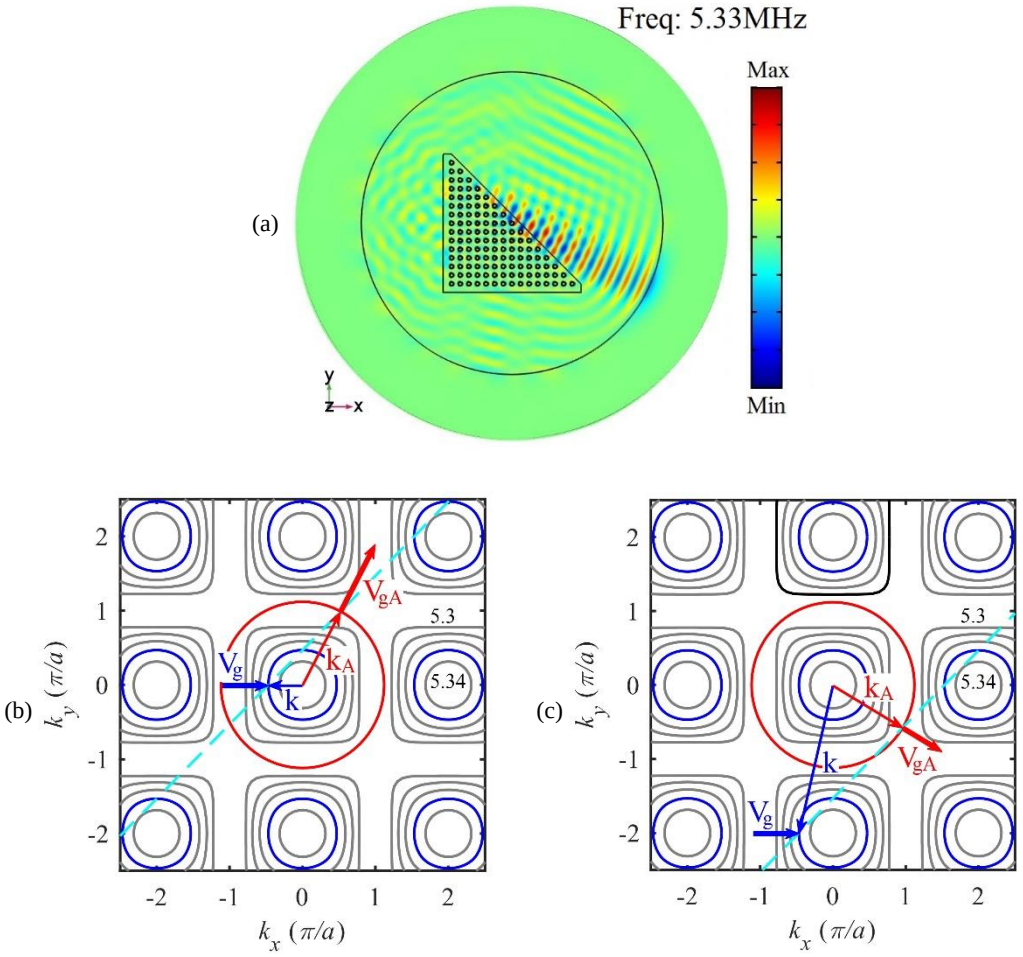

Figure 1.18: (a) Plot of the out-of-plane displacement on the top surface of the plate under the excitation of an incident SH_0 mode at frequency 5.33MHz. EFCs analysis of (b) the negative and (c) the positive refraction at the outlet interface. The transmitted wave is assumed to be A_0 mode only.

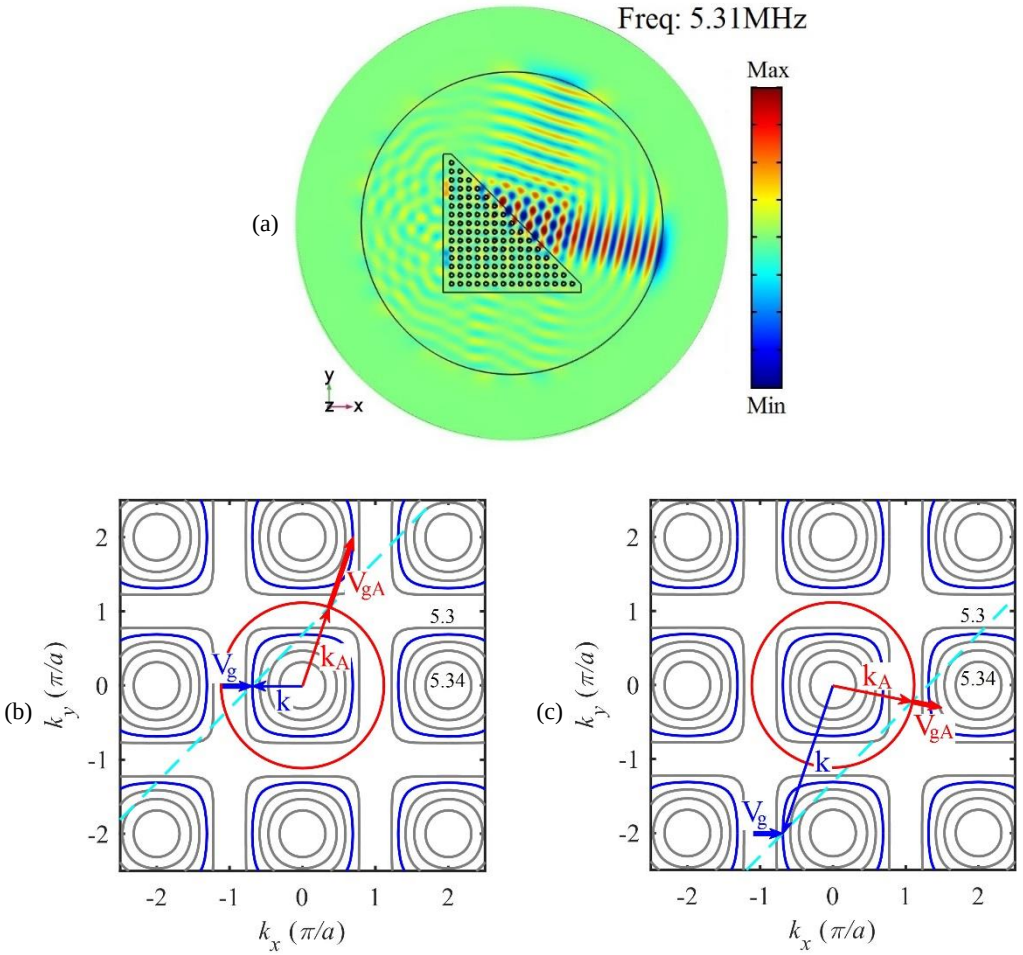

Figure 1.19: (a) Plot of the out-of-plane displacement on the top surface of the plate under the excitation of an incident SH_0 mode at frequency 5.31MHz. EFCs analysis of (b) the negative and (c) the positive refraction at the outlet interface. The transmitted wave is assumed to be A_0 mode only.

Secondly, we assume that the transmitted wave only consists of S_0 mode and we analyze the refraction at frequencies 5.33MHz and 5.31MHz following the same procedure as for A_0 mode. The results are displayed in figure 1.20(a) and (b) where the blue solid lines represent the EFCs in the supercell and the magenta solid lines represent the EFCs in the surrounding plate at frequencies 5.33MHz and 5.31MHz. The group velocities and the wave vectors in the supercell are denoted as $\mathbf{V_g}$ and $\mathbf{k}$ respectively. Both these quantities were calculated at frequencies 5.33MHz in figure 1.20(a) and 5.31MHz in figure 1.20(b). The symbols $\mathbf{V_{gS}}$ and $\mathbf{k_S}$ shown in figure 1.20(a) are for the group velocity and the wave vector at frequency 5.33MHz in the surrounding plate.

It can be seen that the refraction schemes for S_0 mode at frequencies 5.33MHz and 5.31MHz are totally different from one another. Only the negative refraction with an angle of 54.9° occurs in the former case and no refracted beam, whether positive or negative, is observed in the latter case. This suggests the

occurrence of the abnormal refraction [101–103] that both the symmetric and antisymmetric modes contribute to the out-of-plane displacement on the negative side of the normal to the outlet interface at frequency 5.33MHz whereas only the antisymmetric mode gets refracted, both positively and negatively, if the frequency is lowered down to 5.31MHz.

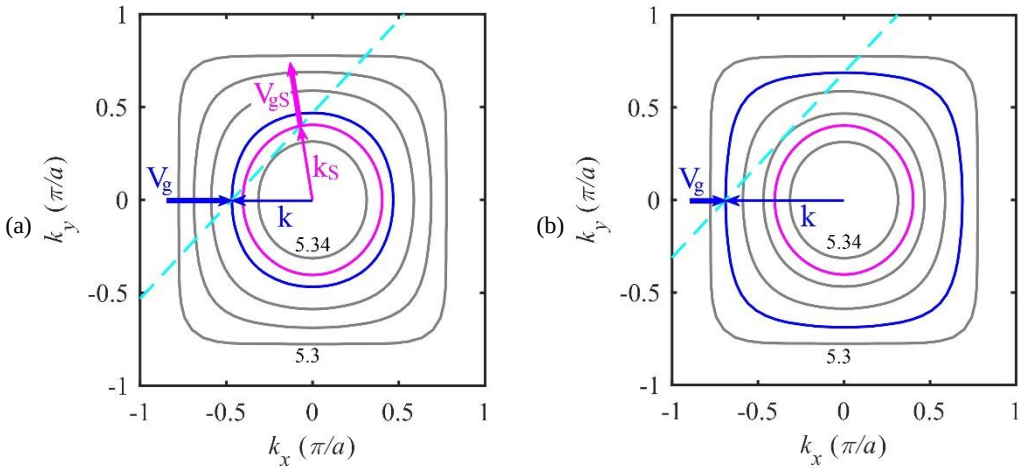

Figure 1.20: EFCs analysis of the refraction at the outlet interface at frequencies (a) 5.33MHz and (b) 5.31MHz. The transmitted wave is assumed to be S_0 mode only.

To further confirm the EFCs analysis, we have performed two-dimensional Fourier transform on the out-of-plane displacement in the area surrounded by a red rectangle dashed line in figure 1.17(a). The computations were done in a local system of coordinates ($x'Oy'$) obtained by rotating the original system by 45° clockwise. The results at frequencies 5.33MHz and 5.31MHz are displayed in figure 1.21(a) and (b) respectively. Both A_0 and S_0 Lamb modes are observed in figure 1.21(a) while there is no contribution of S_0 mode in figure 1.21(b). It is consistent with the previous EFCs analysis that S_0 mode can only be negatively refracted at frequency 5.33MHz. For comparison, the refracted angles calculated from the EFCs analysis are displayed as red dashed lines for A_0 mode and magenta dashed line for S_0 mode. Both are in good agreement with the two-dimensional Fourier transform results.

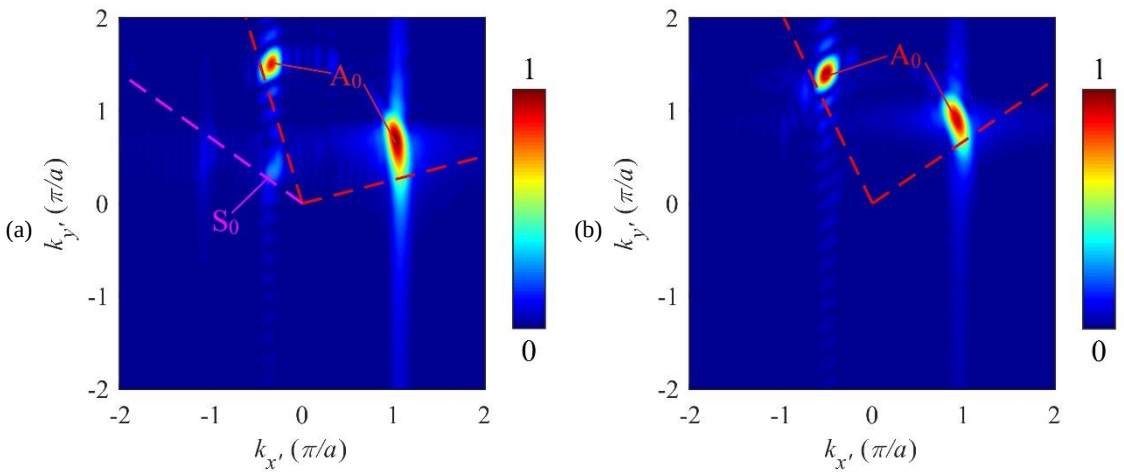

Figure 1.21: Two-dimensional Fourier transform of the out-of-plane displacement in the red rectangle dashed area shown in figure 1.17(a) at frequencies (a) 5.33MHz and (b) 5.31MHz. The red and magenta dashed lines represent their refracted angles calculated from the EFCs analysis.

Thirdly, with regard to the refraction of SH_0 mode, one must consider its in-plane displacement. However, the analysis is rendered more difficultly by the fact that both A_0 and S_0 modes contribute to the in-plane motion downstream the outlet interface. To illustrate this, we display the in-plane displacement components u_x and u_y on the top surface of the plate at frequency 5.33MHz in the left and right panels of figure 1.22(a) respectively. As previously, the refraction on both sides of the normal to the outlet interface can be observed. However, as a result of the displacement components associated to A_0 and S_0 modes whose polarization are close to the *y*-axis [see figure 1.19(b) and figure 1.20(a)], the wave front of the negatively refracted beam in the right panel of figure 1.22(a) appears unstructured. To analyze the refraction of SH_0 mode, the EFC for SH_0 mode in the plate at frequency 5.33MHz is sketched in figure 1.22(b) as the green solid line. $\mathbf{V_{gSH}}$ (green bold arrow) and $\mathbf{k_{SH}}$ (green arrow) are the group velocity and the wave vector for SH_0 mode and $\mathbf{V_g}$ (blue bold arrow) and **k** (blue arrow) are the ones at the same frequency in the supercell. Unambiguously, SH_0 mode can only be negatively refracted with an angle of 29° denoted as the green dashed line in figure 1.22(c). The perpendicular polarization of the negatively refracted beam overlaps with both A_0 (17.2°) and S_0 (54.9°) modes to produce the complex displacement pattern in the right panel of figure 1.22(a). Instead, the in-plane displacement component u_x mainly contains SH_0 mode leading to the plane wave front in the negatively refracted beam. This is further confirmed by the two-dimensional Fourier transform of the in-plane displacement component u_x at frequency 5.33MHz, recorded in the rectangle area drawn in figure 1.17(a) and shown in the left panel of figure 1.22(c). The refracted angle derived from the two-dimensional Fourier transform is in very good agreement with the result from the EFCs analysis. The right panel of figure 1.22(c) depicts the two-dimensional Fourier transform of the in-plane displacement component u_y. It can be seen that the positive refraction only includes A_0 mode whereas the negative refraction combines A_0, S_0 and

SH_0 modes. The two-dimensional Fourier transform performed at frequency 5.31MHz (not shown here) confirms that S_0 mode does not appear in the negative refraction part of the in-plane displacement component map. Further, table 1.1 summarizes all the refracted angles of A_0, S_0 and SH_0 modes.

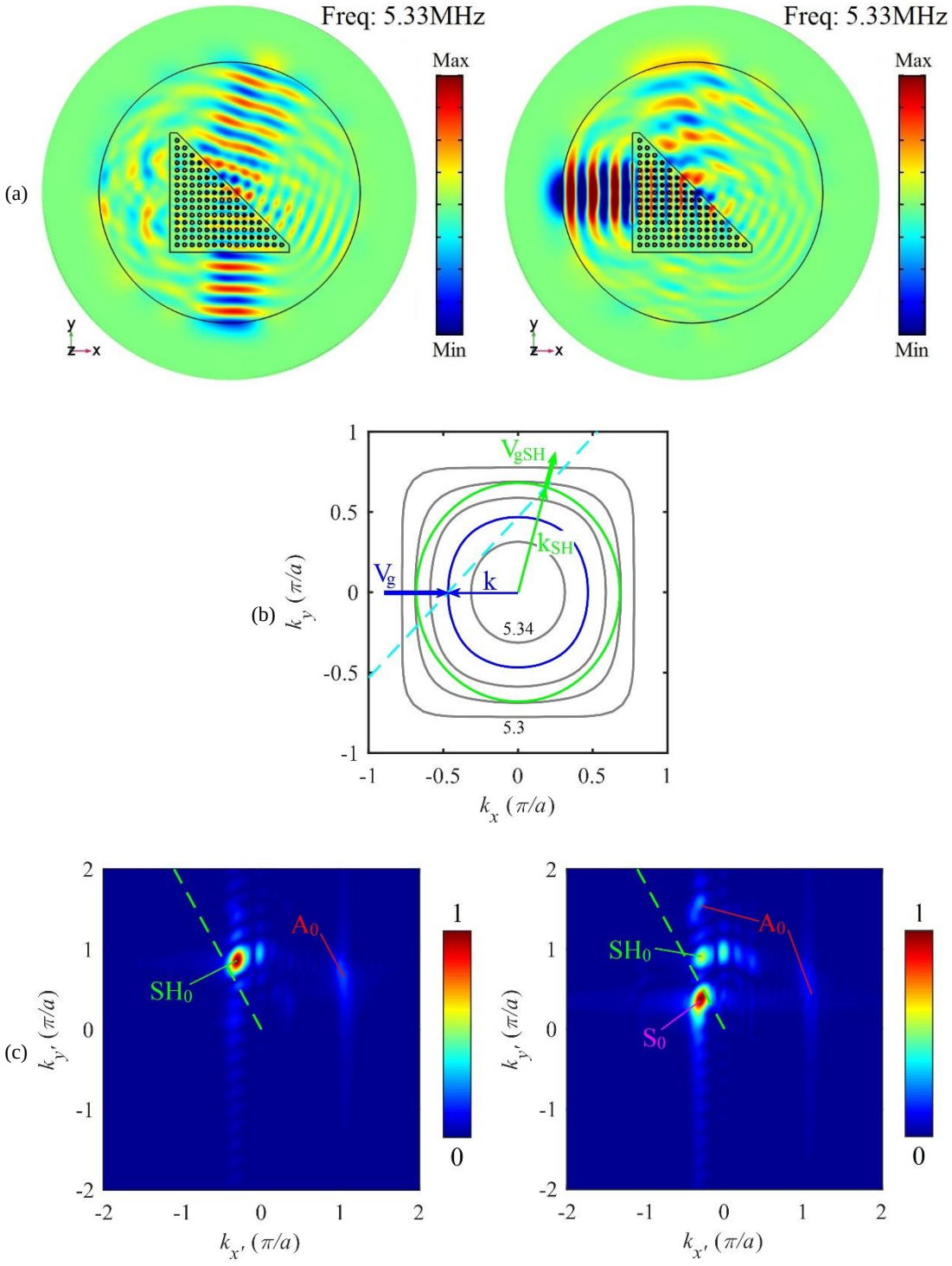

Figure 1.22: (a) Plots of the in-plane displacement components u_x (left panel) and u_y (right panel) on the top surface of the plate under the excitation of an incident SH_0 mode at frequency 5.33MHz. (b) EFCs analysis of the refraction

at the outlet interface at frequency 5.33MHz. The transmitted wave is assumed to be SH_0 mode only. (c) Two-dimensional Fourier transform of the in-plane displacement components u_x (left panel) and u_y (right panel) in the red rectangle dashed area shown in figure 1.17(a) at frequency 5.33MHz. The green dashed line depicts its refracted angle calculated from the EFCs analysis.

Table 1.1: Summary of the refracted angles when the transmission wave is assumed to be A_0, S_0 and SH_0 waves separately at frequencies 5.31MHz and 5.33MHz. The signs (+) and (–) refer to the positive and the negative refraction respectively.

Frequency	A_0 (–)	A_0 (+)	S_0 (–)	S_0 (+)	SH_0 (–)	SH_0 (+)
5.31MHz	25.9°	56.2°	/	/	45.9°	/
5.33MHz	17.2°	75.7°	54.9°	/	29°	/

1.5.1.2 Symmetric double-sided pillared metamaterial supercell

In this part, the prism-shaped supercell is replaced by the symmetric double-sided pillared metamaterial to demonstrate the doubly negative property in that configuration. The frequency of the exciting waves was set to the middle value of the peak in the isolated branch, namely 3.55MHz. At this frequency, the wavelength of the symmetric (antisymmetric) Lamb mode is about eight (three) times the lattice constant which is actually in the deep subwavelength scale.

The out-of-plane displacement component under the excitation of an incident S_0 Lamb wave is plotted in figure 1.23(a). It is clear that the excited S_0 mode propagates into the supercell and gets negatively refracted at the outlet interface. This result demonstrates that both the second-order symmetric bending resonance (B_S) related to the negative effective mass density and the first-order symmetric compressional resonance (C_S) related to the negative effective Young's modulus are simultaneously excited, thus allowing in turn the propagation in the supercell. One should also notice that, as a resonant process, even the small out-of-plane displacement of S_0 Lamb mode is able to excite C_S resonance. When the negative refraction results from the band folding at frequencies larger than the Bragg gap, it is generally accompanied with a high level of reflection at each interface between the phononic crystal and the background that may constitutes a severe drawback in many applications. It is worth mentioning that this is not the case here. To show this, we have computed the transmission coefficient of S_0 Lamb wave impinging at normal incidence a structure made of eleven unit cells along the *x*-axis and infinite along the *y*-axis. The result displayed in figure 1.23(b) indicates that the transmission coefficient is equal to unity in the whole double-negative branch.

The result is totally different for an incident A_0 Lamb mode as plotted in figure 1.23(c). Actually, for this polarization the wave cannot propagate into the metamaterial and is totally reflected at the inlet interface.

This comes from the symmetry of this mode that cannot couple neither to the resonance C_S nor to the resonance B_S of the double-sided pillars and therefore prevents the occurrence of the doubly negative property for the propagation to be allowed.

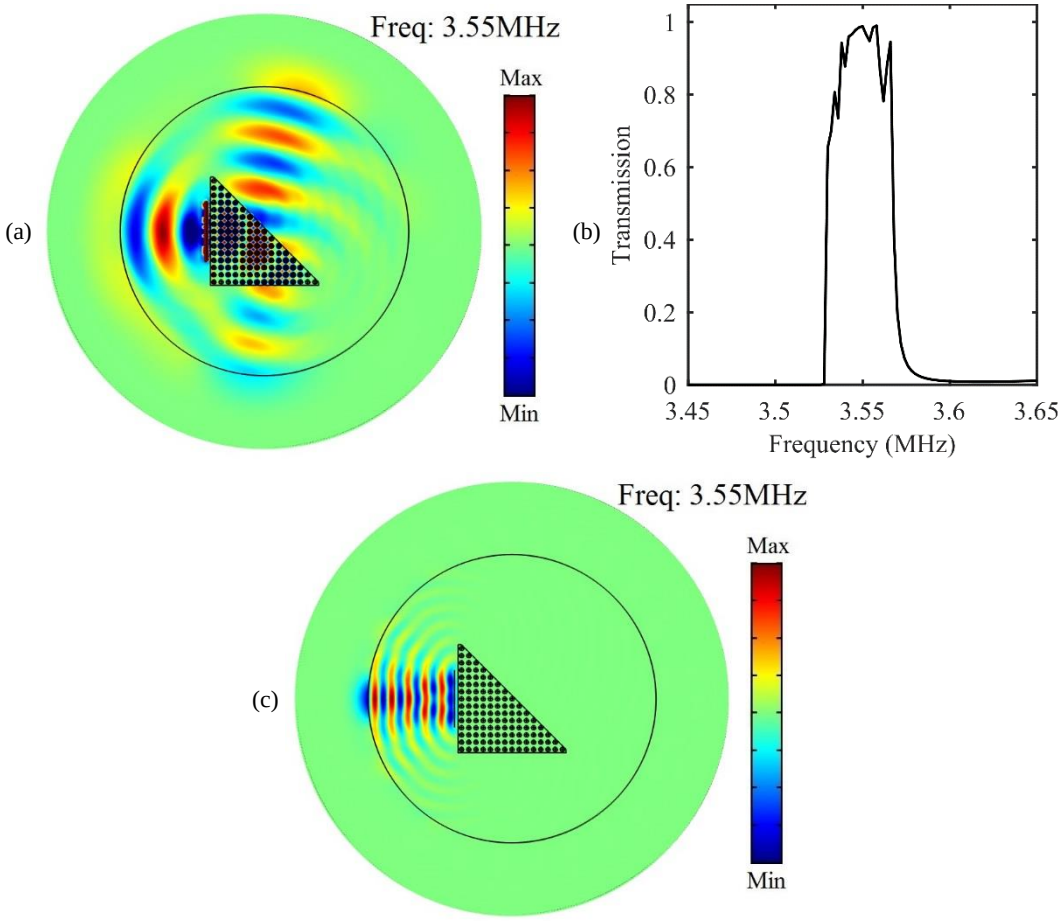

Figure 1.23: (a) Plot of the out-of-plane displacement under the excitation of incident S_0 (a) and A_0 (c) Lamb waves at frequency 3.55MHz. (b) Transmission coefficient of S_0 Lamb wave impinging a phononic crystal built by eleven unit cells along the *x*-axis and infinite along the *y*-axis at normal incidence.

1.5.2 Cloaking effect in a rectangular supercell with void

Another current topic is the implementation of acoustic cloaking based on a zero-index metamaterial and much work has been devoted to this research since a few years [24,60,104,105]. This exciting phenomenon can be ascribed to the effective phase velocity that tends towards to be infinite if the effective mass density is close to zero. Therefore, an alternative method to obtain a refractive index with a null value consists in combining an infinite effective modulus and a finite effective mass density. In what follows, the cloaking effect in both the chiral asymmetric double-sided pillared metamaterial and the symmetric double-sided pillared metamaterial is investigated. The finite element mode is displayed in figure 1.24. The rectangular supercell consists of 132 unit cells and features a $7a \times 3a$ rectangular void in its center. An incident Lamb

wave was excited at a distance of 1000μm far away from the left edge of the metamaterial and perfectly matched layers are implemented on each side of the sample to eliminate any reflection from the boundaries. Periodic boundary conditions are applied on the other two edges.

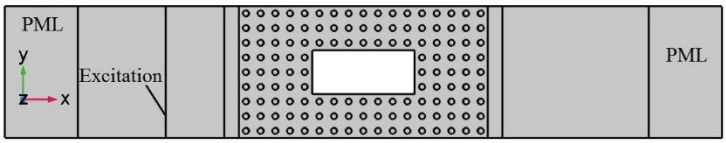

Figure 1.24: Finite elements model implemented to verify the cloaking effect.

1.5.2.1 Chiral asymmetric double-sided pillared metamaterial supercell

As demonstrated in figure 1.11, the proposed chiral double-sided pillared metamaterial exhibits the doubly negative property in between 5.37MHz and 5.41MHz. In the vicinity of the torsional resonance of the pillars (5.41MHz), the effective shear modulus turns to be infinite. Therefore, the frequency of the excited wave is fixed to be 5.4MHz where the infinite shear modulus can be guaranteed. Besides, the doubly negative property can also be excited by an incident S_0 or A_0 Lamb waves propagating along ΓX direction. Considering an incident A_0 Lamb wave at frequency 5.4MHz, the out-of-plane displacement on the top surface of the plate is displayed in the top panel of figure 1.25. It can be seen that the wave front keeps plane upon transmission through the sample except the area around the void where scattering effects are observed. As a consequence of the infinite effective shear modulus and finite effective mass density in the supercell, the phase velocity gets nearly infinite and there is no phase change for an incident A_0 Lamb wave propagating in the supercell, thus allowing for the cloaking effect in this system. The decrease of the amplitude of the transmitted wave is related to mode conversion from A_0 mode to S_0 and SH_0 modes. In contrast, when the working frequency is tuned to be 6MHz, *i.e.* a frequency where the effective shear modulus and mass density are positive, the incident A_0 Lamb wave undergoes strong scattering around the void, giving rise to the distorted wave front observed in the bottom panel of figure 1.25. This simple analysis of the transmission through the chiral pillared system unambiguously reveals that the shielding of substructures at specific frequencies may be achieved with this geometry.

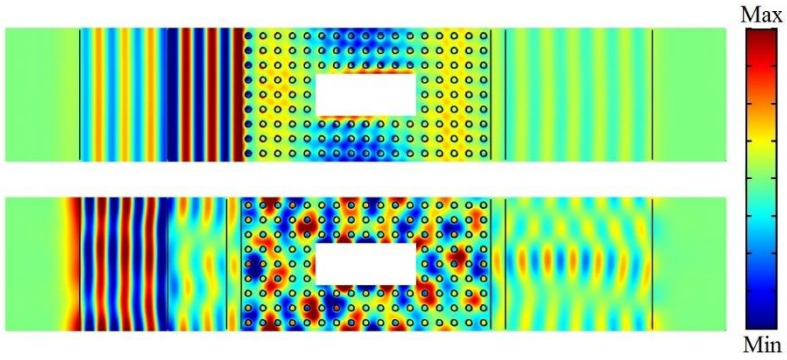

Figure 1.25: Plots of the out-of-plane displacement on the top surface of the plate upon an incident A_0 mode at frequencies 5.4MHz (top panel) and 6MHz (bottom panel).

1.5.2.2 Symmetric double-sided pillared metamaterial supercell

As for the symmetric double-sided pillared metamaterial, the first-order symmetric compressional resonance C_S contributes to the negative effective Young's modulus with an infinite value when the excitation frequency is equal or quite close to 3.57MHz. Whereas the effective density keeps a negative but still finite value at this frequency, thus the zero-index behavior should be observed. Replacing the rectangular supercell as shown in figure 1.24 with the symmetric double-sided pillared metamaterial, an incident S_0 Lamb wave at frequency 3.57MHz was launched. The out-of-plane displacement on the top surface of the plate is depicted in the top panel of figure 1.26. At this frequency, the wave front keeps plane upon transmission through the sample owing to the constant phase during the propagation. In contrast, when the excitation frequency is tuned to be 4MHz, *i.e.* a frequency where the effective Young's modulus and mass density are positive, the incident S_0 Lamb wave undergoes strong scattering around the void, thus leading to the distorted wave front in the bottom panel of figure 1.26.

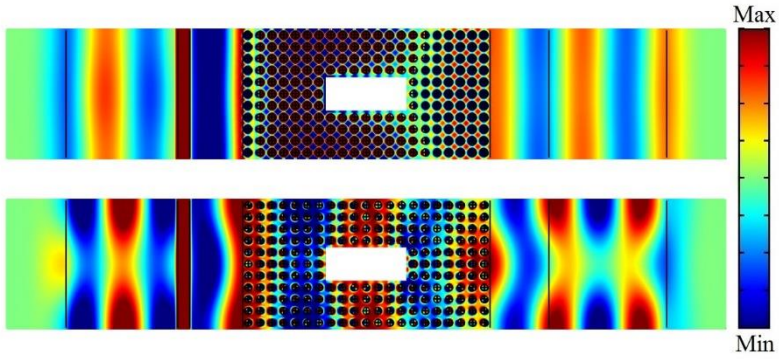

Figure 1.26: Plots of the out-of-plane displacement on the top surface of the plate upon an incident S_0 mode at frequencies 3.57MHz (top panel) and 4MHz (bottom panel).

1.6 Conclusion

In this chapter, we have numerically investigated the negative properties of two single-phase single-sided pillared metamaterials. It is found that the combination of the bending and the compressional resonances of the pillars can result in the negative effective mass density and the torsional resonance can lead to the negative effective shear modulus. Especially, at bending resonance, the vibration of the pillars may be broken down into a rotational and a translational motion induced by the internal moment and the traction force respectively. And we demonstrate that it is the latter that generates the negative effective mass density whereas the moment applied to the plate by the rotational motion is ineffective.

To achieve the doubly negative property, we have figured out two possible approaches. The mechanism is explained and discussed in details. The first scheme is to combine the torsional resonance of one pillar and the bending and the compressional resonances of another pillar. Then, simultaneously negative effective mass density and shear modulus can be obtained in the merged asymmetric double-sided pillared metamaterial. The formed double-negative branch is SH polarized and the bending mode of the pillar in the plane perpendicular to the direction of propagation accounts for the in-plane negative effective mass density whereas the torsional mode of the other pillar contributes to the negative effective shear modulus. In addition, we show that the width of the doubly negative branch can be enlarged by a factor of 3.7 by simply employing perforated holes into the plate. Considering the transmission through a structure that is finite along the *x*-axis and infinite along the *y*-axis, SH_0 mode has proven to be the most suitable candidate. The proposed asymmetric double-sided pillared metamaterial shows polarization dependence for the propagation along ΓX direction. At the doubly negative branch, an incident SH_0 wave propagates without any measurable attenuation whereas an incident A_0 (S_0) Lamb wave is totally reflected. Moreover, mode conversion is observed and studied by computing the displacement of the transmitted wave when the wave vector deviates from being along ΓX direction. To overcome the difficulty of exciting the pillar into the torsional vibration with A_0 (S_0) mode, we have introduced the chirality into the unit cell, causing that way an asymmetric deformation in the surrounding area of the pillars. The efficiency of this design is demonstrated by computing the transmission spectrum of an incident A_0 Lamb wave.

The second scheme is to employ the symmetric double-sided pillared metamaterial. It is shown that the negative effective mass density is achieved owing to the combination of the symmetric bending resonance and the antisymmetric compressional resonance of the pillars and the negative effective Young's modulus relates to the symmetric compressional resonance. Moreover, the double-sided pillared metamaterial has the advantage to allow separating the symmetric and antisymmetric modes which is not achievable with the single-sided configuration. The symmetric band is created by the close vicinity of a bending resonance and a compressional resonance that together allow for the opening of a narrow pass band. Furthermore, the

influence of the geometrical parameters of the unit cell on the width of both the band gap and the double-negative branch is studied. The band gap shifts downwards when increasing the height of the pillars or decreasing the diameter of the pillars, while the thickness of the plate merely affects the position of the band gap. More importantly, both the height of the pillars and the thickness of the plate have a strong impact on the width of the double-negative branch. By carefully designing the unit cell, the width can be significantly enlarged. In particular, equation (1.12) demonstrates that materials with large Poisson's ratio allow for larger width.

To evidence the occurrence of the doubly negative property, the refraction at the outlet interface between a prism-shaped supercell and its surrounding plate is discussed. As for the asymmetric double-sided pillared metamaterial, interestingly, both positive and negative refractions are observed. The physical explanation of this behavior is analyzed in details with the help of the EFCs analysis. We show that the out-of-plane displacement in the positive refraction domain only involves A_0 mode. As for the negative refraction, at frequency 5.33MHz it involves both A_0 and S_0 modes, whereas at frequency 5.31MHz only A_0 mode is refracted while S_0 mode is reflected. Regarding the symmetric double-sided pillared metamaterial, the phenomena turn much simpler. S_0 Lamb wave at a frequency in the double-negative branch can propagate within the supercell whereas the propagation of A_0 Lamb mode is forbidden. Finally, zero-index refraction is carried out in both the chiral asymmetric double-sided pillared metamaterial and the symmetric double-sided pillared metamaterial. And the cloaking effect of a void inside the rectangular supercell is well observed.

Chapter 2

2 Topological transport of Lamb waves in pillared phononic crystals

2.1 Introduction

Realization of topologically protected edge states has provided an intriguing approach to manipulate the wave propagation in both the photonic crystals [39,40,113–116,41,106–112] and the phononic crystals [29,31,119–128,32,129,34–37,44,117,118]. One-way propagation immune to the defects and disorders at the domain wall between two topologically distinct configurations can be achieved. The essence of such fascinating phenomenon origins from the topological phase which was firstly investigated in quantum systems. Given its great potentials in the unidirectional transport with negligible attenuation, it has been quickly employed in the photonic and phononic crystals to robustly guide the electromagnetic, acoustic and elastic waves. In this chapter, emphasize is placed on the elastic phononic crystals.

On the whole, there are three kinds of topological phononic crystals that are in analogy to quantum Hall effect (QHE), quantum spin Hall effect (QSHE) and quantum valley Hall effect (QVHE) respectively. Firstly, to mimic QHE, active components should be involved to break the time-reversal symmetry in the system, leading to the nonzero Chern number, and then topological chiral edge states can be achieved [29,30,42,117,118,130–134]. Regarding the elastic topological phononic crystals, for example, Wang *et al.* [29] investigated both square and hexagonal lattice phononic crystals with gyroscopes connected to each mass at the lattice points. Owing to the gyroscopic inertial effects, the time-reversal symmetry in the system is broken and the Chern numbers turns to 1 or 2, indicating single or multimode chiral edge states. The suppression of reflected waves at both the sharp corners and the line defection has been numerically demonstrated. Thereafter, Nash *et al.* [30] experimentally observed the unidirectional wave propagation in such system. Concerning the acoustic topological phononic crystals, Yang *et al.* [117] incorporated circulating flows into a triangular lattice acoustic structure to break the time-reversal symmetry. The unidirectional transport against the cavity and Z-shape corners has been numerically demonstrated. Similarly, the chiral edge states in the honeycomb and square lattice counterparts have been developed by Ni *et al.* [132] and Chen *et al.* [133] respectively. Recently, an experimental demonstration of acoustic Chern insulator by using an angular-momentum-biased resonator array with the broken Lorentz reciprocity has been carried out by Ding *et al.* [31]. Overall, this kind of topological phononic crystal imposes great challenges on practical applications due to the system complexity.

Secondly, when emulating QSHE with the time-reversal symmetry reserved in the system, it only involves passive components, whereas it requires intricate designs to achieve a double Dirac cone. Wu *et al.* [107] presented the realization in the topological photonic states purely based on the conventional dielectric material and the unidirectional propagation by injecting electromagnetic wave with positive or negative angular momentum. By transforming a honeycomb lattice of cylinders into a triangular lattice of cylinder hexagons, the Dirac cone at point K (K') of the honeycomb lattice is folded to a double Dirac cone at point Γ which is further referred as zone folding mechanism. The topological phase transition can be achieved by contracting or expanding the hexagonal clusters, leading to the nonzero spin Chern number. Afterwards, this mechanism is extended to the acoustic [32,135–137] and elastic [124,126,138–142] topological phononic crystals respectively. Except that, a double Dirac cone can also occur at point K (K') of the BZ. In the photonic crystals, it can be achieved by overlapping two single Dirac cones, each created by the transverse-electric and transverse-magnetic modes respectively, at the same frequency [43]. While in the elastic phononic crystals, Mousavi *et al.* [33] employed a dual scale patterning into a phononic crystal slab to degenerate the symmetric and antisymmetric Lamb modes. Such design is of significant complexity and challenging to implement. Furthermore, a more feasible design was proposed by Miniaci *et al.* [143] where exploited the sensitivity to macroscopic modifications in the unit cell introduced by the through or blind holes, which breaks the mirror-symmetry and induces the spin-orbit coupling interaction.

Thirdly, in analogy to QVHE, it exploits the valley degree of freedom, labelling as energy extrema of quantum states in momentum space, which gains much attention owing to its potentials as a new type of information carrier like spins in spintronics. Extending the valley concept into classical waves, the occurrence of the valley-like dispersion curves has been made possible by the band folding in the artificial crystals arranged in the honeycomb lattice [144,145]. After that, a great deal of acoustic [35,36,119,146–151] and elastic [152,153,162,163,154–161] topological phononic crystals have been reported and the valley-protected edge states were theoretically predicted and experimentally observed. For example, Lu *et al.* [35,119] firstly introduced this concept into the acoustic phononic crystals which consist of triangular rods in a two-dimensional wave guide within which symmetries can be characterized by the rotation of the rods. Dirac cones would occur upon reservation of the C_{3v} symmetry. Once the symmetry is broken by rotating the rods, the Dirac cone is lifted and the vortex revolution (clockwise and anticlockwise) at each valley plays the role of the valley degree of freedom. With regard to the elastic configurations, Pal *et al.* [153,162] theoretically studied the valley-protected edge states in a honeycomb lattice discrete system and experimentally observed the unidirectional propagation of the flexural wave. Compared to the previous two categories, the valley Hall topological phononic crystal features significantly reduced geometrical complexity and the topological phase transition can be achieved by merely breaking the space-inversion

symmetry in the unit cell, leading to the nonzero valley Chern number. However, to suppress the inter-valley scattering, the large separation between the opposite valleys should be ensured.

Very recently, the topologically protected edge state, combining both pseudospin and valley degrees of freedom, has gained more and more interest. Specifically, it has been reported that the pseudospin-valley combined edge states can occur at the domain wall constructed by two distinct systems each supporting QSHE and QVHE respectively [38–41,43,44]. For instance, Kang *et al.* [39] juxtaposed a rod-collar photonic crystal emulating QVHE and a triangle-prism photonic crystal mimicking QSHE that possess a common topological band gap. By pushing the rods in contact with either one bounding copper plate or lying in between the plates that breaks the mirror-symmetry in the system, the in-phase and out-of-phase combination of the transverse-electric and transverse-magnetic modes in the eigenmodes define the pseudospin up and down states, resulting in the nonzero spin Chern number. Besides, rotating the triangle prisms can contribute to the nonzero valley Chern number. Then, the bulk-edge correspondence principle ensures the occurrence of the topological edge states owing to the difference in the topological invariant across the interface. The propagation of these edge states depends on both the pseudospin and valley states. Based on this property, valley-dependent wave guiding at a Y-junction has been demonstrated. However, the aforementioned two topological crystals supporting QVHE and QSHE respectively involve totally different geometries which renders their designs very complex. Therefore, designing an adjustable platform that allows for swapping between QSHE and QVHE is of primary importance for this research field.

In this chapter, we present another approach to manipulate the propagation of Lamb wave in the pillared phononic crystals (PPnCs), namely the topologically protected transport of Lamb waves between two topologically distinct systems. The discussion is organized as follows. In Sec. 2.2, we briefly introduce the process to create a single Dirac cone and a double Dirac cone occurring at point K (K') of the BZ. Subsequently, we discuss in Sec. 2.3 the topological propagation of Lamb waves in elastic wave guides constructed by two honeycomb lattice asymmetric double-sided PPnCs which extends the work about the double-negative branch in the square lattice system demonstrated in the previous chapter. In Sec. 2.4, we concentrate on a honeycomb lattice symmetric double-sided PPnC and investigate the occurrence of the topological edge state at different domain walls and the refraction patterns at the zigzag and armchair terminations. Finally, it ends with the general conclusion in Sec. 2.5.

2.2 Constructing a single Dirac cone and a double Dirac cone

It is well known that a single Dirac cone and a double Dirac cone are prerequisite to emulate QVHE and QSHE and then investigate the topologically protected edge states. As demonstrated in Ref. [135], a single Dirac cone can be judiciously realized by transforming a triangular lattice structure to a honeycomb lattice

arrangement that results in a perfect folding of the band structure. Here, we briefly recall this process. In figure 2.1(a), it shows a triangular array of soda cans which can be recognized as subwavelength resonators and the first branch of the band structure. Above this branch, there is a low frequency band gap associated with the negative effective bulk modulus contributed by the Helmholtz resonances. Then, the distance between nearest neighbors is kept the same as the one in the triangular pattern and rearrange in the honeycomb lattice [see figure 2.1(b)]. The honeycomb unit cell (green dashed box) can be viewed as the union of two triangular unit cells (blue dashed box), offsetting with respect to each other along ΓM2 direction. These two sub unit cells can form an equidistant Bragg planes along ΓK2 (ΓK2') direction that folds the first branch in the triangular lattice. Then, a single Dirac cone occurs at point K2 (K2') of the BZ. What's more, the size of the BZ is now one-third of the one in figure 2.1(a). Further, additional point degeneracies can be obtained by considering a supercell containing a full hexagonal resonators [see red dashed box in figure 2.1(c)] instead of only two resonators. Thanks to this mathematic band folding, the single Dirac cone located at point K2 (K2') of the BZ are now folded into point Γ, thus creating a double Dirac cone. By analogy with these, both a single Dirac cone and a double Dirac cone in the elastic configuration can be obtained.

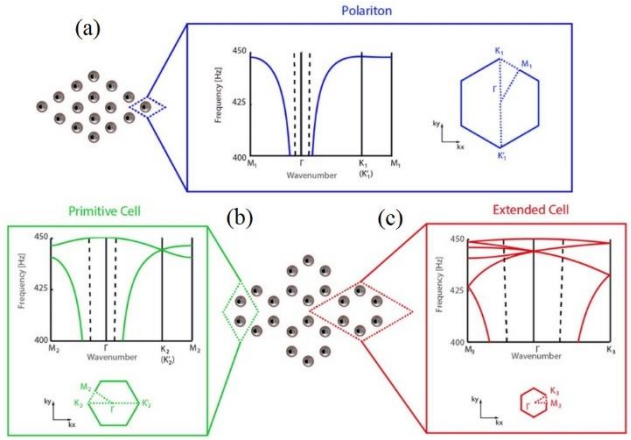

Figure 2.1: (a) A triangular array of Helmholtz resonators and its corresponding band structure. (b) A honeycomb lattice Helmholtz resonators and its corresponding band structure. (c) A triangular lattice phononic crystal with hexagonal resonators inside the unit cell and its corresponding band structure. [135]

As for a double Dirac cone, it can also occur at point K (K') of the BZ instead of the center point Γ as mentioned in figure 2.1. Specifically, in the elastic systems, it can be realized by designing a dual-scale phononic crystal plate as shown in figure 2.2(a) [33]. Owing to the symmetry about the mid-plane of the plate in the unit cell, the eigenmodes can be decomposed into symmetric and antisymmetric modes according to the symmetry of the deformed displacement fields. Two scales of patterning are intentionally designed for different purposes. The larger wavelength patterning is adopted to fold the symmetric and antisymmetric branch to construct two separated single Dirac cones. The smaller deep-subwavelength

patterning yields extreme elastic anisotropy that can ensure the overlap of the two aforementioned Dirac cones with simultaneously matched frequency and group velocity, as shown in figure 2.2(b), which is usually unachievable because of the drastically different dispersion relations. Such complex designs impose great challenge on the applications. After that, a more feasible approach is proposed in Ref. [143] [see figure 2.3(a)]. It involves through holes in the triangular-hole patterned phononic crystal plate to degenerate the symmetric and antisymmetric modes at the same frequency as illustrated in figure 2.3(b) and (c) to form a double Dirac cone. Then, by replacing the through holes with blind holes to break the mirror-symmetry, the double Dirac cone is lifted as depicted in figure 2.3(d) and the spin-orbit coupling interaction can be emulated. Similarly, by degenerating the transverse-electric and transverse-magnetic modes in the photonic crystals, a double Dirac cone occurring at point K (K') of the BZ can also be realized [106].

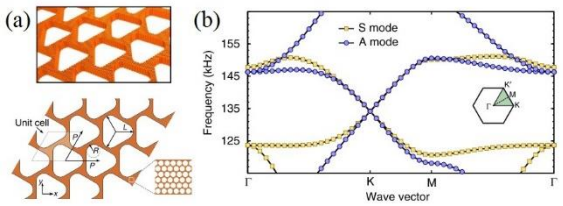

Figure 2.2: (a) A dual-scale phononic crystal plate and (b) its corresponding band structure. [33]

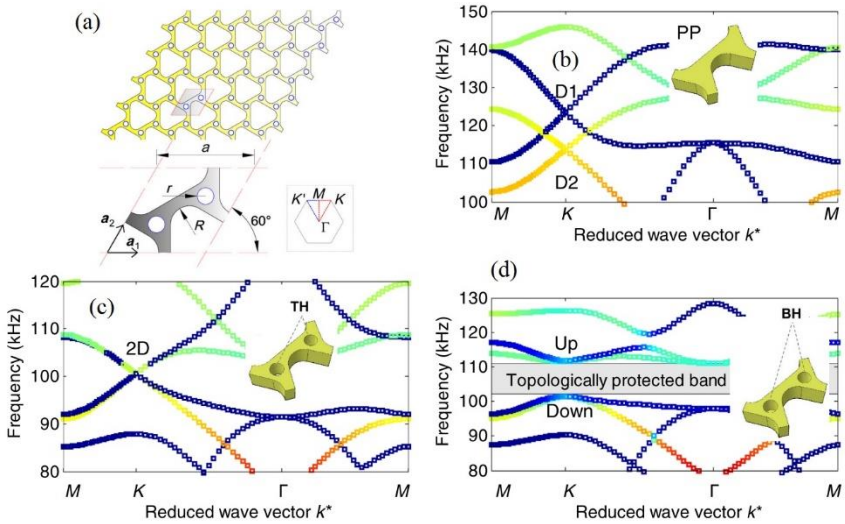

Figure 2.3: (a) A triangular-hole patterned phononic crystal plate. Perspective view of the patterned unit cells and the corresponding band structures: (b) patterned plate (PP), (c) plate with additional circular holes drilled through the thickness (TH) and (d) with blind holes (BH). [143]

2.3 Topological transport in an asymmetric double-sided PPnC

As discussed in chapter 1, in the low frequency regime, A_0 and S_0 Lamb waves propagating in the plate can be modulated by the bending and the compressional vibration of the pillars. With regard to SH_0 mode, its in-plane polarization is perpendicular to the propagation direction that can be well coupled into the torsional

motion of the pillars. We have demonstrated that a double-negative branch can occur in a square lattice asymmetric double-sided PPnC by assembling the bending, the compressional and the torsional modes into a common frequency interval [19]. Besides, the wave propagation along ΓX direction at a frequency where the doubly negative property occurs is polarization-dependent. It can be considered as a propagative band for an incident SH_0 wave, while it turns to be a forbidden one for an incident A_0 (S_0) Lamb wave. What's more, unlike the respective intersection of the other dispersion curves, it is totally isolated inside a complete band gap that can simplify the discussion significantly. In this part, we develop a honeycomb lattice asymmetric double-sided PPnC and investigate the occurrence of the topological edge state in analogy to QVHE in this system.

2.3.1 Artificially folding and polarization-dependent propagation

Firstly, we consider an asymmetric double-sided PPnC arranged in a triangular lattice. The corresponding elementary unit cell together with its first irreducible BZ are displayed in figure 2.4(a). Two distinct pillars denoted as pillar A and pillar B are concentrically connected to a thin plate. The lattice constant and the thickness of the plate are chosen to be a = 231μm and e = 100μm. Pillar A is designed to form a low frequency band gap that features the negative effective mass density by combining the bending and the compressional resonances. The diameter and the height are d_A = 120μm and h_A = 268μm. Further, the frequency of the torsional resonance of pillar B is optimized to occur inside the above band gap whose diameter and height are d_B = 140μm and h_B = 160μm. Then, the doubly negative property can be achieved. Afterwards, the band structure is computed and displayed in figure 2.4(b). As expected, a negative-slope branch exists in between 4.408MHz and 4.486MHz. And it would disappear when considering the single-sided PPnC constructed merely by pillar A or pillar B. Therefore, it is exactly a double-negative branch that possesses simultaneously negative effective mass density (in between 4.176MHz and 4.643MHz) and shear modulus (in between 4.408MHz and 4.486MHz). To give more evidences, the eigenmodes at points C, D and E labelled in figure 2.4(b) are depicted in figure 2.4(c). Clearly, the eigenmode at point C is the first-order torsional resonance of pillar B that contributes to the negative effect shear modulus. The eigenmodes at points D and E are the second-order bending resonance and the first-order compressional resonance of pillar A respectively. Their combination accounts for the negative effective mass density. The color bar shown in figure 2.4(b) depicts the weighting of the torsional deformation of pillar B along the z-axis computed by

$$\xi = \frac{\iiint_{\text{Pillar B}} \left(\text{curl } \mathbf{U}\right)_z^2 dV}{\iiint_{\text{Pillar B}} \left(\text{curl } \mathbf{U}\right) \cdot \left(\text{curl } \mathbf{U}\right) dV}, \tag{2.1}$$

where $(\mathrm{curl}\,\mathbf{U})$ denotes the curl vector of the displacement field **U** and V represents the volume of the unit cell. Inside the double-negative branch, intuitively, the torsion along the z-axis is the dominant deformation especially at the wave vectors around the corners of the BZ. Subsequently, the transmission spectra for incident A_0, S_0 and SH_0 waves along ΓK1 and ΓM1 directions are calculated and represented by the black, the red and the blue solid lines in figure 2.4(d) and (e) respectively. It can be seen that the double-negative branch functions as a forbidden band for an incident A_0 (S_0) Lamb waves whereas an incident SH_0 wave can propagate with negligible attenuation along both primary directions. Therefore, it might be interesting to create a Dirac cone with such double-negative branch that has potentials in realizing the topologically protected SH_0 wave.

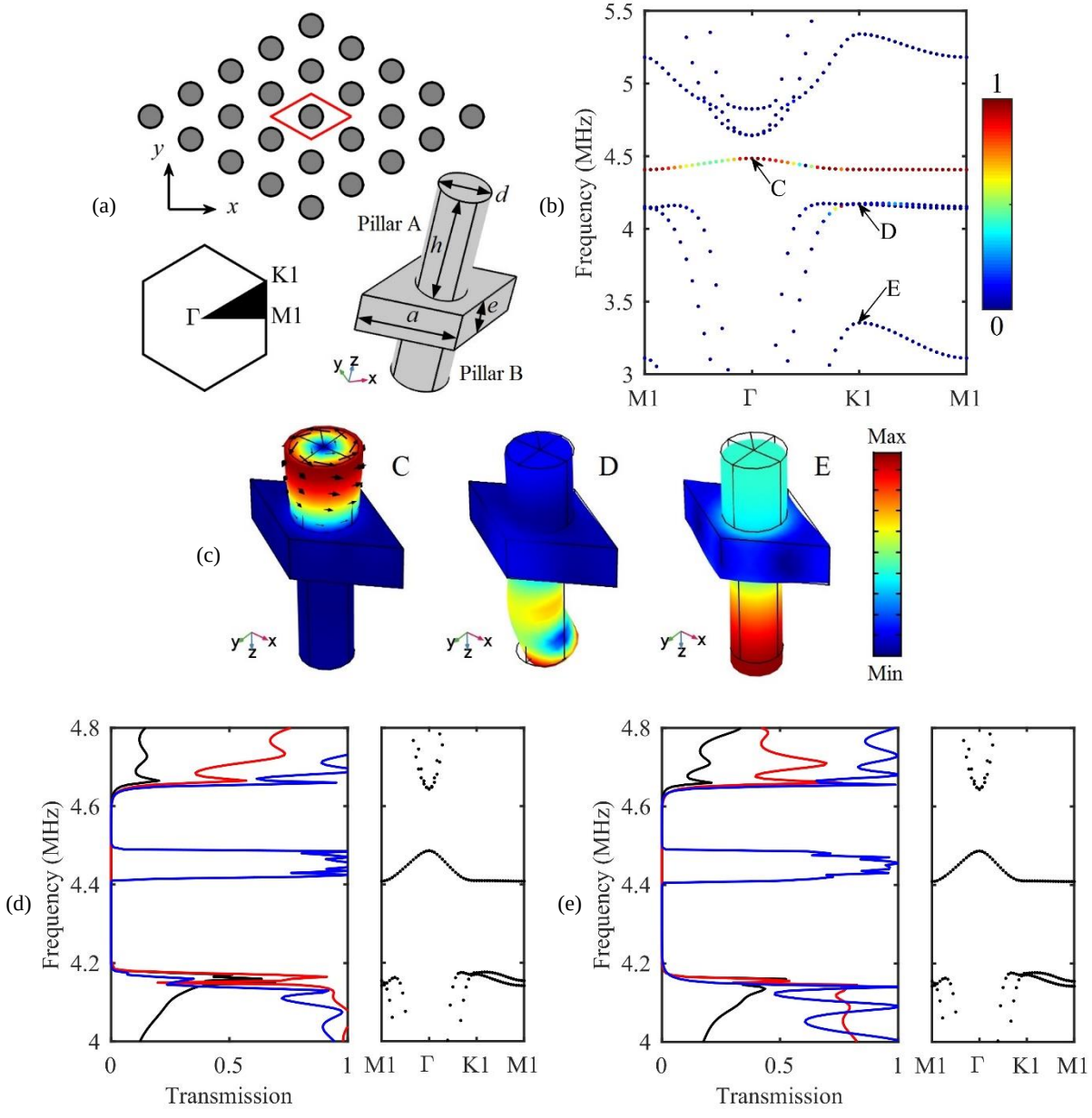

Figure 2.4: (a) Schematic of the proposed asymmetric double-sided PPnC arranged in the triangular lattice and (b) the corresponding band structure. (c) Eigenmodes at points C, D and E labelled in (b) and the black arrows represent the elastic deformation vectors. Transmission spectra of incident A_0 (black), S_0 (red) and SH_0 (blue) Lambs wave propagating along (d) ΓK1 and (e) ΓM1 directions.

Secondly, to construct a Dirac cone with the aforementioned double-negative branch, we resort to a honeycomb arrangement as shown in figure 2.5(a). Two pairs of the asymmetric double-sided pillars are assembled into one honeycomb unit cell. To keep the distance between the nearest neighbors the same as the one in the triangular lattice in figure 2.4(a). The lattice constant is adjusted to be a = 400μm. Besides, we prefabricate four through holes with diameter d = 240μm at the four corners of the unit cell. These patterned holes can soften the plate and the band structure would be slightly changed [77].

The corresponding band structure ranging from 3MHz to 5.5MHz is shown in figure 2.5(b). It is found that a partial forbidden band opens in between 4.302MHz and 4.344MHz along ΓM2 direction. Two eigenmodes degenerate at frequency 4.318MHz forming a single Dirac cone at point K2 (K2') of the BZ. The group velocity is 56.138m/s. Figure 2.5(c) displays the eigenmodes at points F, G, H1 and H2 labelled in figure 2.5(b). Regarding the eigenmode at point F, pillar BL and pillar BR exhibit in-phase torsional resonance which suggests the reservation of the negative effective shear modulus that results in the negative group velocity around point F. As for the eigenmode at point G, pillar BL and pillar BR exhibit out-of-phase torsion which comes from the band folding directly. Concerning the eigenmodes at points H1 and H2, the torsion along the *z*-axis in pillar BL and pillar BR are the dominant deformation. According to $\mathbf{k} \cdot \mathbf{p}$ perturbation theory, once the Dirac cone is lifted by imposing the space-inversion symmetry breaking perturbation, the newly eigenmodes at the bounding can be well approximated by a linear combination of the degenerate eigenmodes [42]. Therefore, it can be speculated that the torsion of pillar BL and pillar BR along the *z*-axis will still play an important role in the perturbed configuration. Figure 2.5(d) displays the transmission spectra along ΓK2 direction of incident A_0 (black), S_0 (red) and SH_0 (blue) Lamb waves respectively. The corresponding computational mode is depicted on the top. The excitation is placed at the left of the supercell and two perfectly match layers are placed at two ends respectively to eliminate the reflected waves from the boundaries. Periodic conditions are applied along the *y*-axis. The higher branch (upper cyan region in between 4.318MHz and 4.353MHz) is a propagative band for an incident SH_0 wave and whereas a forbidden one for an incident A_0 (S_0) Lamb wave. While at the lower branch (lower cyan region in between 4.141MHz and 4.318MHz), the contrary polarization-dependent propagation can be observed. What's more, in between 4.302MHz and 4.344MHz (magenta region), all Lamb modes are propagative owing to the mixture of the in-phase and out-of-phase deformation. Figure 2.5(e) displays the transmission spectra along ΓM2 direction. It can be seen that only SH_0 wave can propagate at both the lower

and higher branches. It can be well understood by considering the symmetry about the *xz*-plane of the model depicted on the top.

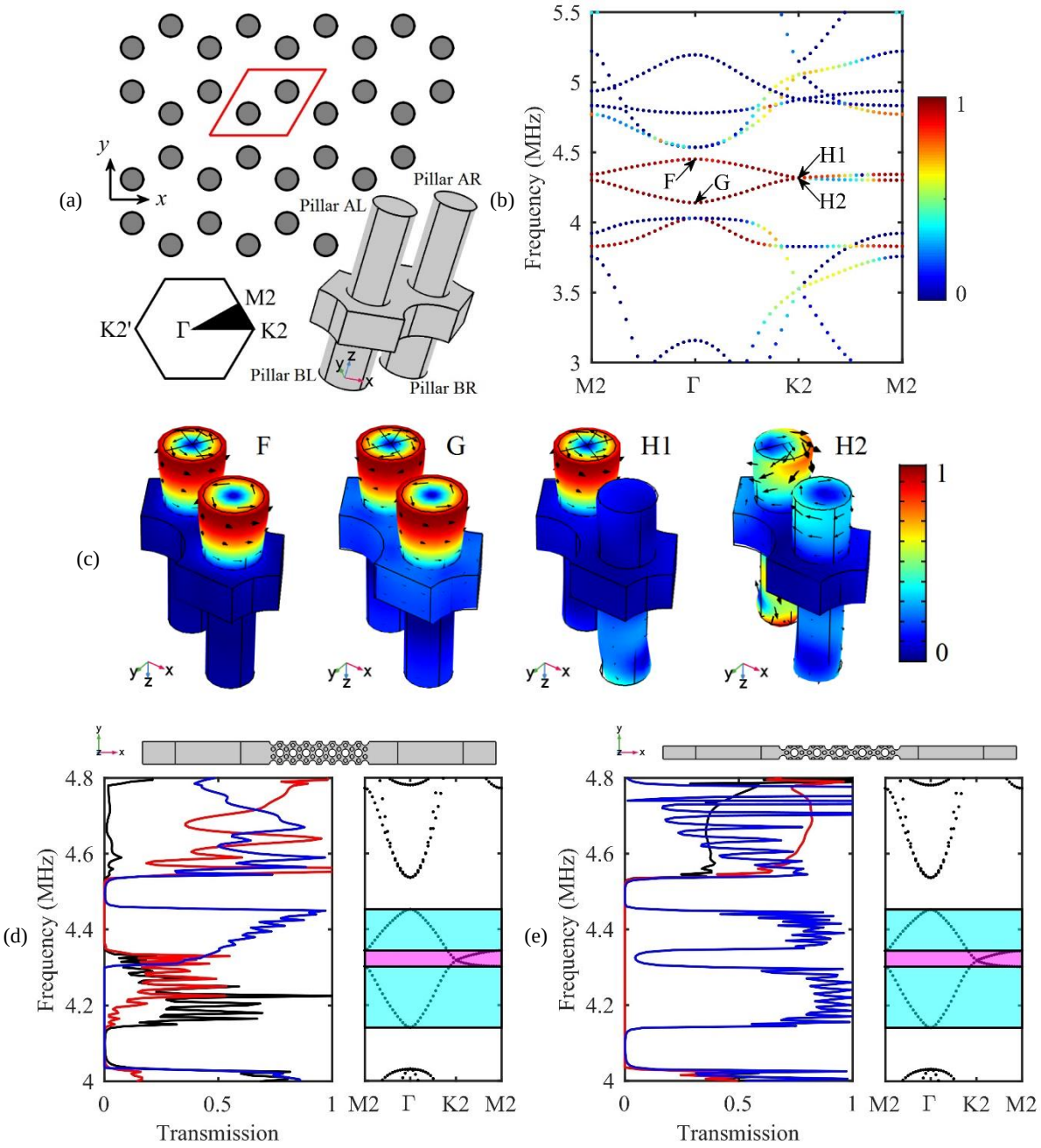

Figure 2.5: (a) Schematic of the proposed asymmetric double-sided PPnC arranged in the honeycomb lattice and (b) the corresponding band structure. (c) Eigenmodes at points F, G, H1 and H2 labelled in (b) and the black arrows represent the elastic deformation vectors. Transmission spectra of incident A_0 (black), S_0 (red) and SH_0 (blue) Lamb waves propagating along (d) ΓK2 and (e) ΓM2 directions.

2.3.2 Emulating QVHE

2.3.2.1 Topological phase transition

In order to mimic QVHE, we need to impose the space-inversion symmetry breaking perturbation on the honeycomb unit cell to lift the Dirac cone and introduce the topological phase transition. Thus, a nonzero valley Chern number can be obtained together with the occurrence of a reopened band gap at the valleys. Practically, it can be done by varying the height or the diameter of the asymmetric double-sided pillars. During this process, C_{3v} symmetry is broken because of the violation of the mirror-symmetry about lattice vectors while C_3 symmetry is still preserved in the perturbed configuration.

As discussed in Sec. 2.3.1, the torsional vibration of the lower pillars has significant contribution to the formation of the constituent branches of the Dirac cone. Therefore, the perturbation in the height of the lower pillars (pillar BL and pillar BR) with $h_{\mathrm{BL}} = h_{\mathrm{B}} + \Delta h_V$ and $h_{\mathrm{BR}} = h_{\mathrm{B}} - \Delta h_V$ is firstly taken into consideration. The band structure with the height perturbation $\Delta h_V = 1\mu\mathrm{m}$, hereafter referred as type-I, is displayed in figure 2.6(a). It can be seen that the Dirac cone is lifted and an omnidirectional band gap ranging from 4.301MHz to 4.335MHz reopens. To reveal the vortex chirality at the valley K2, on the top surface of the plate the phase distribution of the out-of-plane displacement is evaluated and plotted in figure 2.6(b). The top and bottom panels display the phase fields at the higher (4.335MHz) and lower (4.301MHz) bounding respectively. In the top panel, the phase field decreases gradually in anticlockwise direction at the center of pillar AL which can be recognized as the valley pseudospin up state while it keeps constant at the position of pillar AR. In the bottom panel, a uniform distributed phase field can be observed at the position of pillar AL and the phase field decreases gradually in clockwise direction at the center of pillar AR which can be recognized as the valley pseudospin down state. Owing to the reservation of the time-reversal symmetry in the system, these valley pseudospin states will be inverted at the valley K2'. It is also noted that a specific valley state can be selectively excited by involving proper chirality in the source to match the valley pseudospin state of the desired valley [119,164–166].

In order to visualize the impact of the height perturbation on the reopened band gap, the evolution of the pseudospin up and down states at the valley K2 represented by the red and black circles respectively is shown in figure 2.6(c). Clearly, when the height perturbation Δh_V becomes nonzero, the Dirac cone is lifted and a band gap reopens. And the width of the band gap is almost proportional to the height perturbation. More importantly, the band gap will firstly close and then reopen again when the height perturbation Δh_V crosses zero. Meanwhile, the frequency order of the pseudospin up and down states is inverted that signals the topological phase transition. Considering another perturbed configuration with the height perturbation $\Delta h_V = -1\mu\mathrm{m}$ (type-II), it is exactly the space-inverted counterpart of type-I PPnC. Even if they have the

same dispersion curves, they are absolutely distinct from the topological point of view. Secondly, the perturbation in the height of the upper pillars (pillar AL and pillar AR) with $h_{AL} = h_A + \Delta h_V$ and $h_{AR} = h_A - \Delta h_V$ is also investigated and the evolution of the pseudospin up and down states is plotted in figure 2.6(d) represented by the red and black crosses respectively. In comparison, the width of the reopened band gap is more sensitive to the height perturbation of the lower pillars.

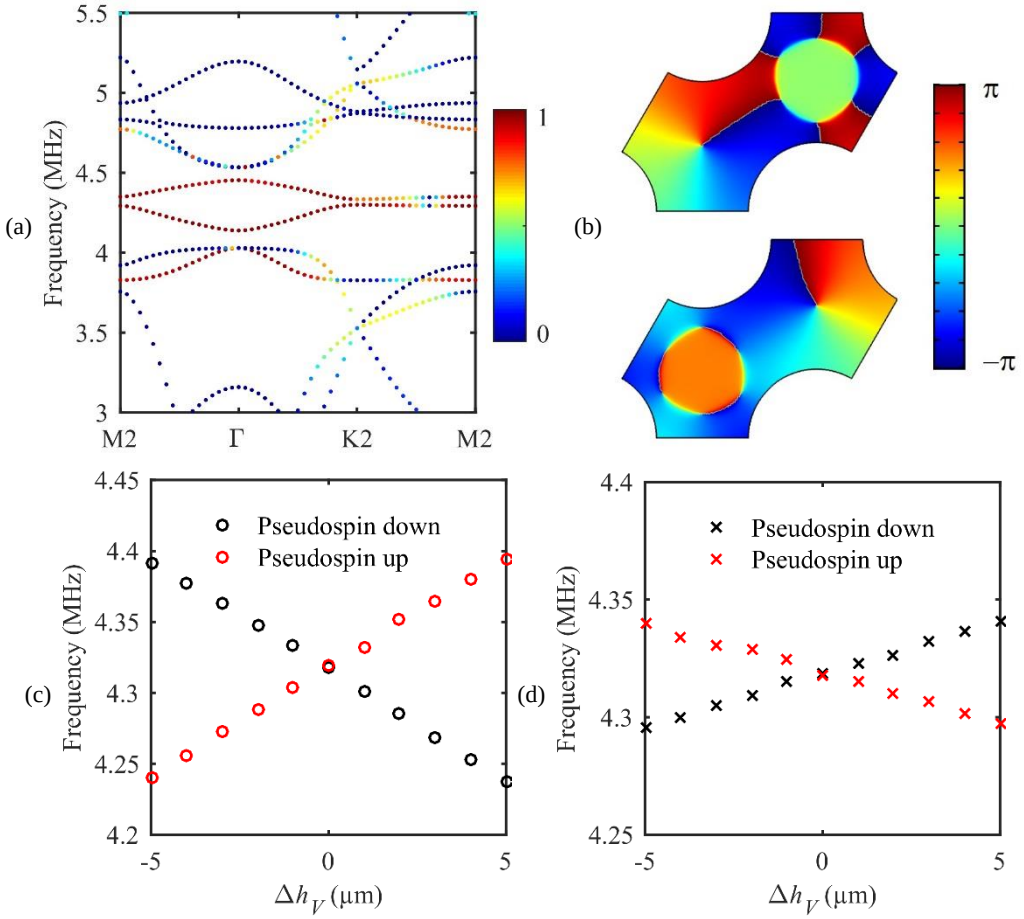

Figure 2.6: (a) Band structure of the perturbed PPnC with the height perturbation $\Delta h_V = 1\mu m$. (b) Phase distribution of the out-of-plane displacement on the top surface of the plate at the higher (top panel) and lower (bottom panel) bounding of the lifted Dirac cone. Evolution of the pseudospin up and down states at the valley K2 against the height perturbation Δh_V in the (c) lower (red and black circles) and (d) upper (red and black crosses) pillars.

To represent the topological feature involved in type-I PPnC after lifting the Dirac cone, the topological invariant defined as the integral of the Berry curvature over a portion of the BZ is numerically studied. The Berry curvature of nth band at a given wave vector **k** can be calculated from

$$\Omega_n(\mathbf{k}) = \nabla_{\mathbf{k}} \times \left\langle \mathbf{u}_n(\mathbf{k}) \middle| i\, \nabla_{\mathbf{k}} \middle| \mathbf{u}_n(\mathbf{k}) \right\rangle \cdot \hat{\mathbf{z}}, \tag{2.2}$$

where $\mathbf{u}_n(\mathbf{k})$ is the periodic part of the displacement field in the unit cell at the given wave vector $\mathbf{k} = (k_x, k_y)$. Owing to the reservation of the time-reversal symmetry, the Chern number defined by integrating the Berry curvature over the whole BZ will be expected to be zero. As for the perturbed PPnC with the space-inversion symmetry broken, the Berry curvature of the lower bounding of the lifted Dirac cone at the valley K2 (K2') can be analytically expressed as [110,155,157]

$$\Omega(\mathbf{k}) = \pm \frac{m v_g^2}{2\left(|\delta\mathbf{k}|^2 v_g^2 + m^2\right)^{-2/3}}, \tag{2.3}$$

where $\delta\mathbf{k} = \mathbf{k} - \mathbf{k}_{K2/K2'}$ is the relative wave vector with respect to the valley K2 (K2') and v_g is the group velocity at the Dirac cone. m denotes the effective mass and is proportional to the frequency interval between the pseudospin up and down states. It is also directly related to the height perturbation Δh_V and can represent the space-inversion symmetry breaking strength. Generally, in a small space-inversion symmetry breaking case, the Berry curvature will be highly localized around the valley K2 (K2'). The well-known valley Chern number defined as the local integral of the Berry curvature in the vicinity of the valley will converge quickly to a nonzero quantized value which can be theoretically derived as [110,153]

$$C_V\left(\mathrm{K2/K2'}\right) = \frac{1}{2\pi}\int \Omega(\mathbf{k})\, d^2\mathbf{k} = \pm\frac{1}{2}\mathrm{sgn}(m). \tag{2.4}$$

It can be seen that the valley Chern number only depends on the sign of the effective mass m. Besides, in equation (2.3), it is clear that the distribution of the Berry curvature becomes broader as the effective mass m increases and the interference of the Berry curvature between two opposite valleys might occur. Then, the assumption of the small space-inversion symmetry breaking is no long valid, instead, it turns to a large space-inversion symmetry breaking case. In that situation, when directly integrating equation (2.3) in the vicinity of the valley [163] to calculate the valley Chern number, a huge deviation from the theoretical values ±1/2 might arise because of the destructive interference of the Berry curvature between the two opposite valleys.

To identify the strength of the space-inversion symmetry breaking in type-I PPnC, the distribution of the Berry curvature around the valley is numerically obtained [110,155]. In figure 2.7(a), the black dotted line represents the numerical results along ΓK2 direction at the wave vectors varying from $k_x = 2\pi/3a$ to $k_x = 10\pi/3a$ and $k_y = 0$. For comparison, the theoretical values predicted by equation (2.3) is depicted as the red solid line. It can be seen that the results obtained from these two different methods are in good agreement in between $k_x = 4\pi/3a$ to $k_x = 8\pi/3a$, *i.e.* along the high symmetry boundaries K2-M2-K2' of the BZ. While in between $k_x = 2\pi/3a$ to $k_x = 4\pi/3a$ the numerical result decreases quickly than the theoretical prediction.

After that, the anisotropy around the valley K2 is also evaluated and illustrated in figure 2.7(b). The black, red and blue solid lines denote the absolute values of the Berry curvature at the wave vectors with distances $|\boldsymbol{\delta k}| = 0.05|\Gamma K2|$, $0.1|\Gamma K2|$ and $0.2|\Gamma K2|$ away from the valley K2. The Berry curvature exhibits a circular shape when the wave vectors are very close to the valley K2 which can be considered to be isotropic. However, it turns to the triangular shape as the distance $|\delta k|$ increases to be $0.1|\Gamma K2|$. And once the distance $|\delta k|$ is set to be $0.2|\Gamma K2|$, it changes to the clover-like shape and decreases much more quickly when the wave vector deviates from the high symmetry boundaries K2-M2-K2' of the BZ which might be related to the steep dispersion curve around the lifted Dirac cone. The distribution becomes strongly anisotropic. To calculate the valley Chern number, the Berry curvature around the valley K2 is numerically obtained and shown in figure 2.7(c). The integration of the Berry curvature over this reciprocal space is −0.22 which has a huge discrepancy from the theoretical value −1/2. Therefore, the height perturbation $\Delta h_V = 1\mu m$ in the type-I PPnC can be recognized as a large space-inversion symmetry breaking case. The space-inversion symmetry breaking strength would become stronger if increasing the height perturbation. Figure 2.7(d) depicts both the numerical (black dotted line) and theoretical (red solid line) results of the Berry curvature when the height perturbation is set to be $\Delta h_V = 2\mu m$. The profile of the Berry curvature is much broader and the integral at the valley K2 turns to be −0.08. In between $k_x = 4\pi/3a$ and $k_x = 8\pi/3a$, the Berry curvature associated with the valley K2 and K2' tends to connect directly (see the slope) suggesting the possibility of the very strong inter-valley scattering.

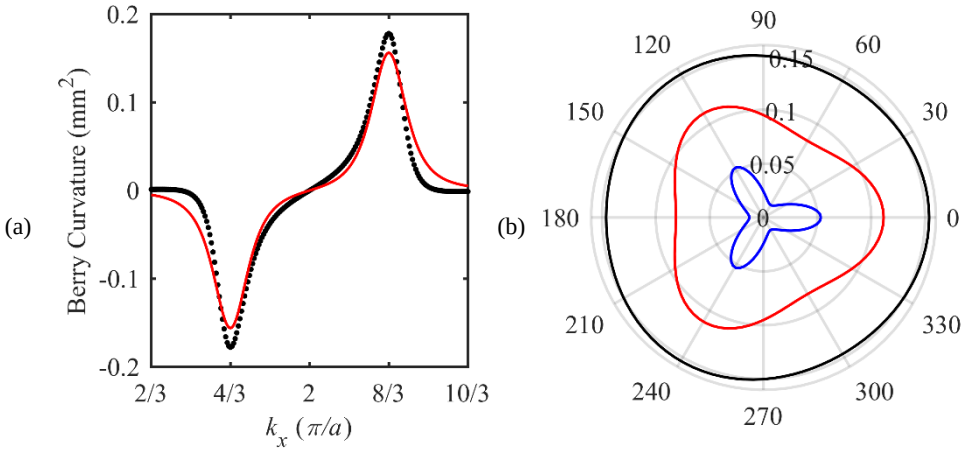

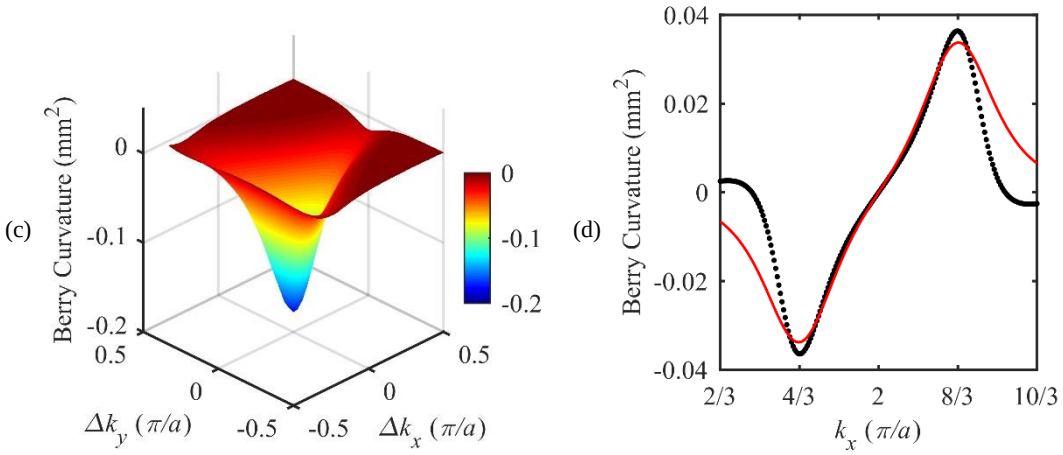

Figure 2.7: Numerical (black) and theoretical (red) values of the Berry curvature along ΓK2 direction at the wave vectors varying from $k_x = 2\pi/3a$ to $k_x = 10\pi/3a$ and $k_y = 0$ when the height perturbation is set to be (a) $\Delta h_V = 1\mu m$ and (d) $\Delta h_V = 2\mu m$. (b) Absolute values of the Berry curvature at the wave vectors with distances $|\delta k| = 0.05|\Gamma K2|$ (black), $0.1|\Gamma K2|$ (red) and $0.2|\Gamma K2|$ (blue) respectively away from the valley K2. (c) Distribution of the Berry curvature in the vicinity of the valley K2 with Δk_x varying from $-0.5\pi/a$ to $0.5\pi/a$ and Δk_y varying from $-0.5\pi/a$ to $0.5\pi/a$.

2.3.2.2 Valley-protected edge states

The above analysis indicates the existence of the valley-protected edge states at the domain walls formed by the topologically distinct type-I and type-II PPnCs. To verify this, we consider a three-layers ribbon supercell as modelled in figure 2.8(a), sandwiching eight unit cells of type-II PPnC in between two sets of six unit cells of type-I PPnC. Two zigzag domain walls are formed and zoomed in the side views, namely LDW and SDW with the height of the adjacent lower pillars at the interface increased and decreased by 1μm respectively. The dispersion curves of the ribbon supercell are displayed in figure 2.8(b) ranging from 4.25MHz to 4.4MHz. The black dotted lines represent the bulk modes. The red and blue dotted lines represent the edge state occurring at LDW and SDW respectively. It should be pointed out that the projection of the valleys K2 and K2' onto these two zigzag domain walls is $k_x = -2\pi/3a$ and $k_x = 2\pi/3a$. At the valley K2, the group velocity of the edge state localized at LDW is negative which can also be predicted by considering the change of the valley Chern number from type-I to type-II PPnC as $C_V^{\text{Type-I}}(\text{K2}) - C_V^{\text{Type-II}}(\text{K2}) = -1$. In contrast, the group velocity turns positive at the valley K2'. The bottom views of the eigenmodes at points M (4.316MHz) and N (4.323MHz) are displayed in the left and right panels of figure 2.8(c). The red arrows denote the elastic deformation vectors. The adjacent lower pillars at LDW exhibit the antisymmetric torsion about the interface and the adjacent upper pillars feature the antisymmetric bending. However, at SDW the torsion of the lower pillars and the bending of the upper pillars are symmetric about the interface. It has been reported that the antisymmetric edge state would turn to be a dead band due to the mismatch in the spatial parity between the eigenmode and the elastic

deformation caused by the incident wave [35,167]. However, it is not that case in this system and it can be well excited in our system when considering an incident SH_0 wave which will be demonstrated in the following discussion.

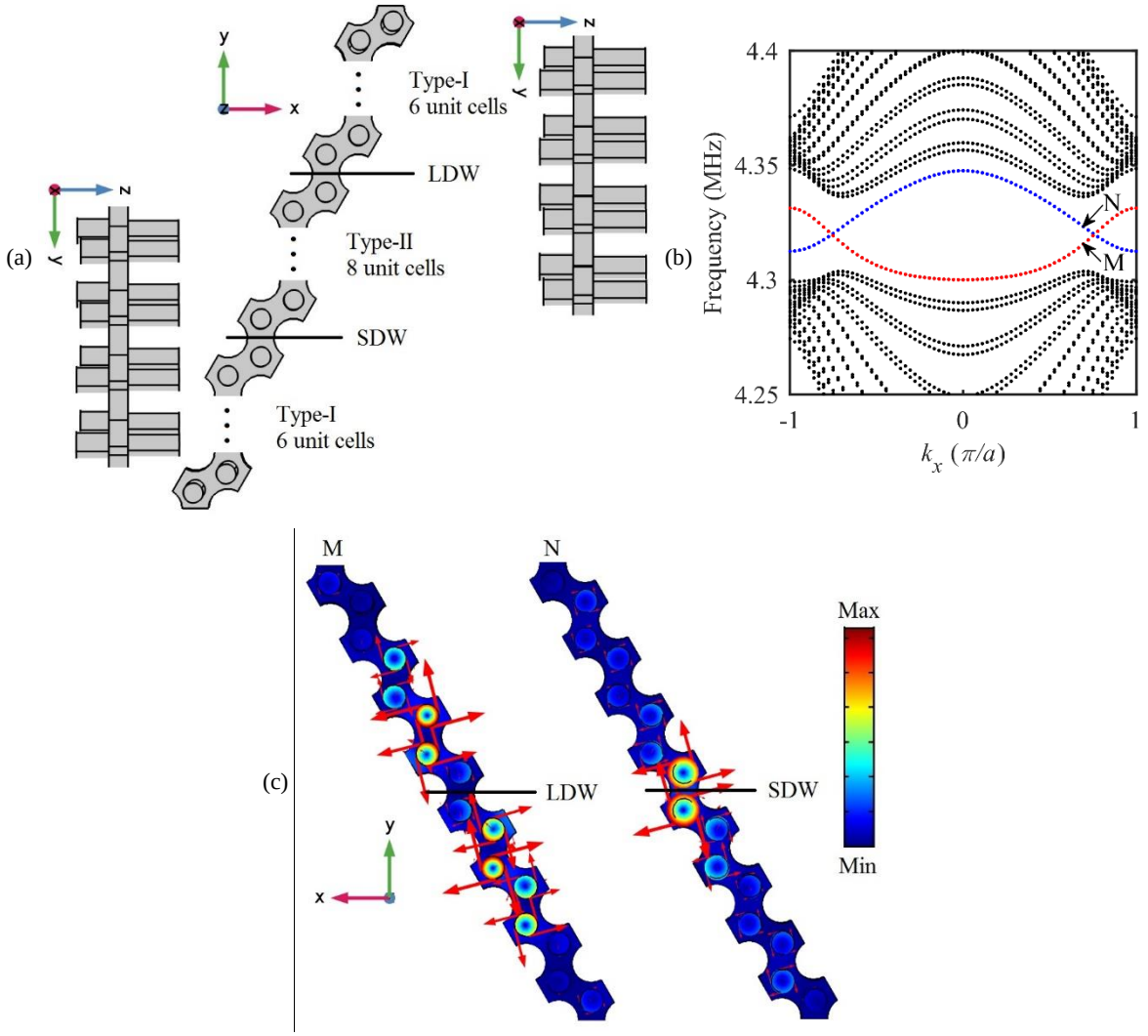

Figure 2.8: (a) Schematic of the proposed three-layers ribbon supercell constructed by sandwiching eight unit cells of type-II PPnC in between two sets of six unit cells of type-I PPnC and zoomed side views of two zigzag domain walls. (b) Dispersion curves of the proposed ribbon supercell. (c) Bottom views of the eigenmodes at points M and N labelled in (b).

To verify the unidirectional transport of the valley-protected edge states, the wave propagation in the straight wave guide as sketched in figure 2.9(a) built by 24×20 unit cells is investigated. The upper and lower domains are made of type-I and type-II PPnCs respectively that forms a LDW at the interface. Perfectly match layers (PMLs) are employed to enclose the whole model to eliminate the reflected waves. Two sources with phase difference $\pi/3$ separated by a distance a are placed at the red point to excite the right-going K2'-polarized edge state [157]. At this domain wall, the edge state features the antisymmetric

deformation about the interface. Firstly, an incident SH_0 wave at frequency 4.314MHz was launched by applying the *y*-axis polarized traction forces. Figure 2.9(b) plots the magnitude of the out-of-plane displacement on the top surface of the plate. The excited wave propagates along the positive *x*-axis which is in agreement with the positive group velocity at the valley K2'. At the right zigzag termination, the K2'-polarized SH_0 wave gets both positively and negatively refracted. To quantitatively discuss the ability to suppress backscattering waves, the ratio between the magnitude of the out-of-plane displacement at the left and right ends is introduced, namely $\eta = A_{\text{Left}}/A_{\text{Right}}$ and is equal to 0.064 in this situation. It slightly deviates from zero, but we can still conclude that in this large space-inversion symmetry breaking case the backscattering wave can be well suppressed at the right zigzag outlet. Secondly, an incident A_0 Lamb wave at the same frequency was launched by applying the *z*-axis polarized forces. The distribution of the magnitude of the out-of-plane displacement is displayed in figure 2.9(c). It can be seen that the injected energy is highly localized around the sources and cannot propagate along the domain wall. Because the generated elastic field cannot match the antisymmetric deformation of the edge state [see the left panel of figure 2.8(c)]. Therefore, it actually turns to be a forbidden band for an incident A_0 (S_0) Lamb wave.

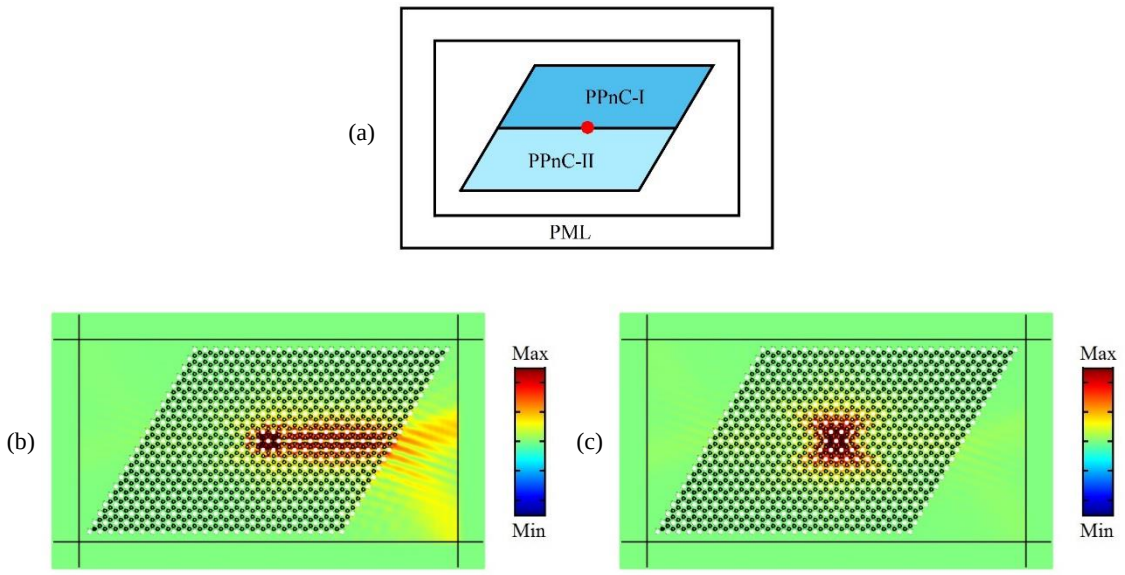

Figure 2.9: (a) Schematic of the straight wave guide featuring a LDW at the interface constructed by placing type-I and type-II PPnCs in the upper and lower domains respectively. The red point represents the position of two phase-matched sources. Plots of the magnitude of the out-of-plane displacement on the top surface of the plate under the excitation of the K2'-polarized (b) SH_0 and (c) A_0 Lamb waves at frequency 4.314MHz.

By inverting the position of type-I and type-II PPnCs as plotted in figure 2.9(a), we can construct another straight wave guide forming a SDW at the interface. At this domain wall, the edge state features the symmetric deformation about the interface. Similarly, both incident K2'-polarized SH_0 and A_0 Lamb waves at frequency 4.325MHz are taken into consideration. The plots of the magnitude of the out-of-plane

displacement on the top surface are displayed in figure 2.10(a) and (b) respectively. It can be seen that the excited SH_0 wave is localized around the sources whereas the excited A_0 Lamb wave can propagate along the negative *x*-axis. These wave propagation phenomena can be understood by considering the spatial parity between the elastic field generated by the sources and the symmetric deformation of the edge state at this domain wall [see the right panel of figure 2.8(c)]. Only A_0 Lamb mode can match the required symmetric displacement field and its propagation along the negative *x*-axis is in agreement with the negative group velocity of the edge state at the valley K2'.

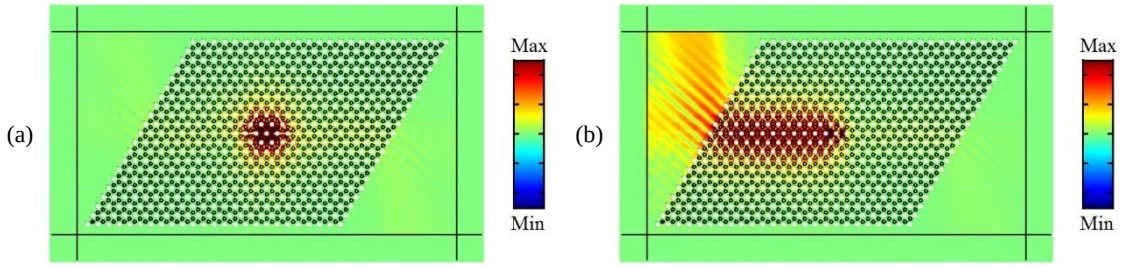

Figure 2.10: Plots of the magnitude of the out-of-plane displacement on the top surface of the plate under the excitation of the K2'-polarized (a) SH_0 and (b) A_0 Lamb waves at frequency 4.325MHz. The straight wave guide is constructed by inverting the position of type-I and type-II PPnCs as illustrated in figure 2.9(a).

In addition, the propagation of the edge state in a Z-shape wave guide featuring two 60° sharp bending corners as sketched in figure 2.11(a) is investigated. This Z-shape wave guide is formed by placing type-I and type-II PPnCs in the upper and lower regions. According to the previous discussion, only SH_0 wave can propagate along this domain wall. A right-going K2'-polarized SH_0 wave at frequency 4.314MHz was launched. The displacement field is plotted in figure 2.11(b). The refracted waves appear at the left outlet which indicates the occurrence of the inter-valley scattering of the edge state at the bending corners. Comparatively, the magnitude at the left end is much smaller than the one at the right end that suggests the weak inter-valley scattering. The magnitude ratio between two outlets is 0.279 which is much larger than the one in the straight wave guide. Therefore, in this large space-inversion symmetry breaking case, the bending corners can result in the weak inter-valley scattering, however, most of the injected energy can propagate smoothly through the Z-shape wave guide.

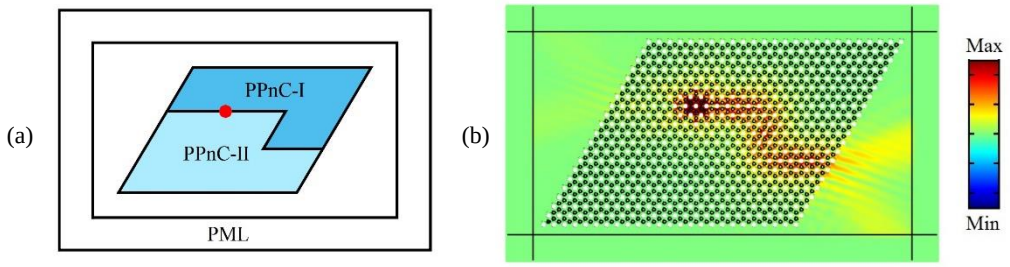

Figure 2.11: Schematic of the Z-shape wave guide constructed by placing type-I and type-II PPnCs in the upper and lower domains respectively. The red point represents the position of two phase-matched sources. (b) Plot of the magnitude of the out-of-plane displacement on the top surface of the plate under the excitation of the K2'-polarized SH_0 wave at frequency 4.314MHz.

Further, the propagation of the edge states in the larger space-inversion symmetry breaking situation is studied. Considering another ribbon supercell with the increased height perturbation Δh_V = 2μm, the dispersion curves are depicted in figure 2.12(a). The red and blue solid lines represent the edge states occurring at LDW and SDW respectively. Compared to the ones displayed in figure 2.8(b), these two newly edge states have the similar profiles, but are totally gapped. To examine the occurrence of the topological protection, the propagation of the K2'-polarized SH_0 wave at frequency 4.304MHz in both the straight and Z-shape wave guides is studied. The results are shown in figure 2.12(b) and (c) respectively. The reflected wave from the zigzag outlet and bending corners can be unambiguously observed. The magnitude ratios are 0.228 for the straight wave guide and 0.943 for the Z-shape wave guide. Therefore, it can be concluded that the topological protection of the edge state cannot be guaranteed any more in this larger space-inversion symmetry breaking case with gapped edge states.

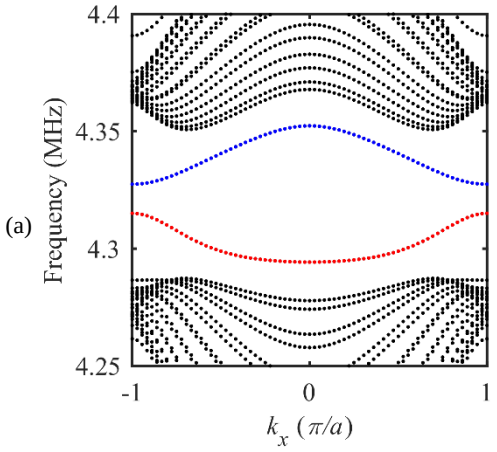

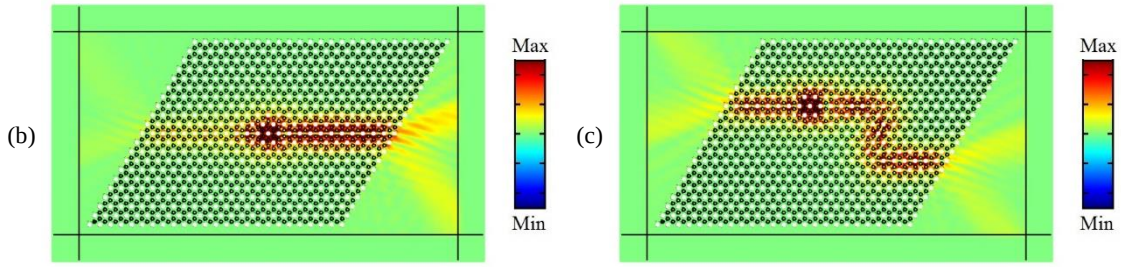

Figure 2.12: (a) Dispersion curves of the proposed three-layers ribbon supercell with the increased height perturbation Δh_V = 2µm. Plots the magnitude of the out-of-plane displacement on the top surface of the plate under the excitation of the K2'-polarized SH_0 wave at frequency 4.304MHz in the (b) straight and (c) Z-shape wave guides.

2.4 Topological transport in a symmetric double-sided PPnC

2.4.1 Occurrence of the Dirac cones and its evolution against the height of the pillars

In this part, the topological transport of Lamb waves in a symmetric double-sided PPnC is presented. Thanks to the symmetry about the mid-plane of the plate in the unit cell, the symmetric and antisymmetric Lamb modes can be well decoupled, providing the opportunities to investigate their associated topological nature respectively. The elementary unit cell together with the BZ are displayed in figure 2.13(a). Two identical arrays of pillars are arranged concentrically over a thin plate. Four through-thickness holes are drilled at the corners of the honeycomb unit cell. The lattice constant and the thickness of the plate were chosen to be a = 400µm and e = 100µm. The diameter and the height of the pillars are $d_A = d_B = d_C = d_D = D$ = 120µm and $h_A = h_B = h_C = h_D = H$ = 160µm. The diameter of the holes is d_H = 280µm. It should be pointed out that the reported phenomena in what follows also apply to any other single-phase systems.

The band structure of the proposed symmetric double-sided PPnC is displayed in figure 2.13(b) that can be decomposed into the symmetric (red dotted lines) and antisymmetric (blue dotted lines) subcomponents owing to the mirror-symmetry in the unit cell. To help to distinguish this, the eigenmodes at points labelled from E1 to E6 are depicted in figure 2.13(b). At points E1 and E2, the double-sided pillars exhibit the symmetric bending. At points E3 and E4, the antisymmetric bending can be observed. At points E5 and E6, the deformation is the mixture of the symmetric bending and symmetric torsion. For the symmetric band structure subcomponent, the deformation of the eigenmodes is symmetric about the mid-plane of the plate that can be well excited by S_0 or SH_0 waves propagating in the plate. Regarding the antisymmetric band structure subcomponent, the deformation of the eigenmodes is antisymmetric about the mid-plane of the plate that can well couple into A_0 Lamb wave propagating in the plate.

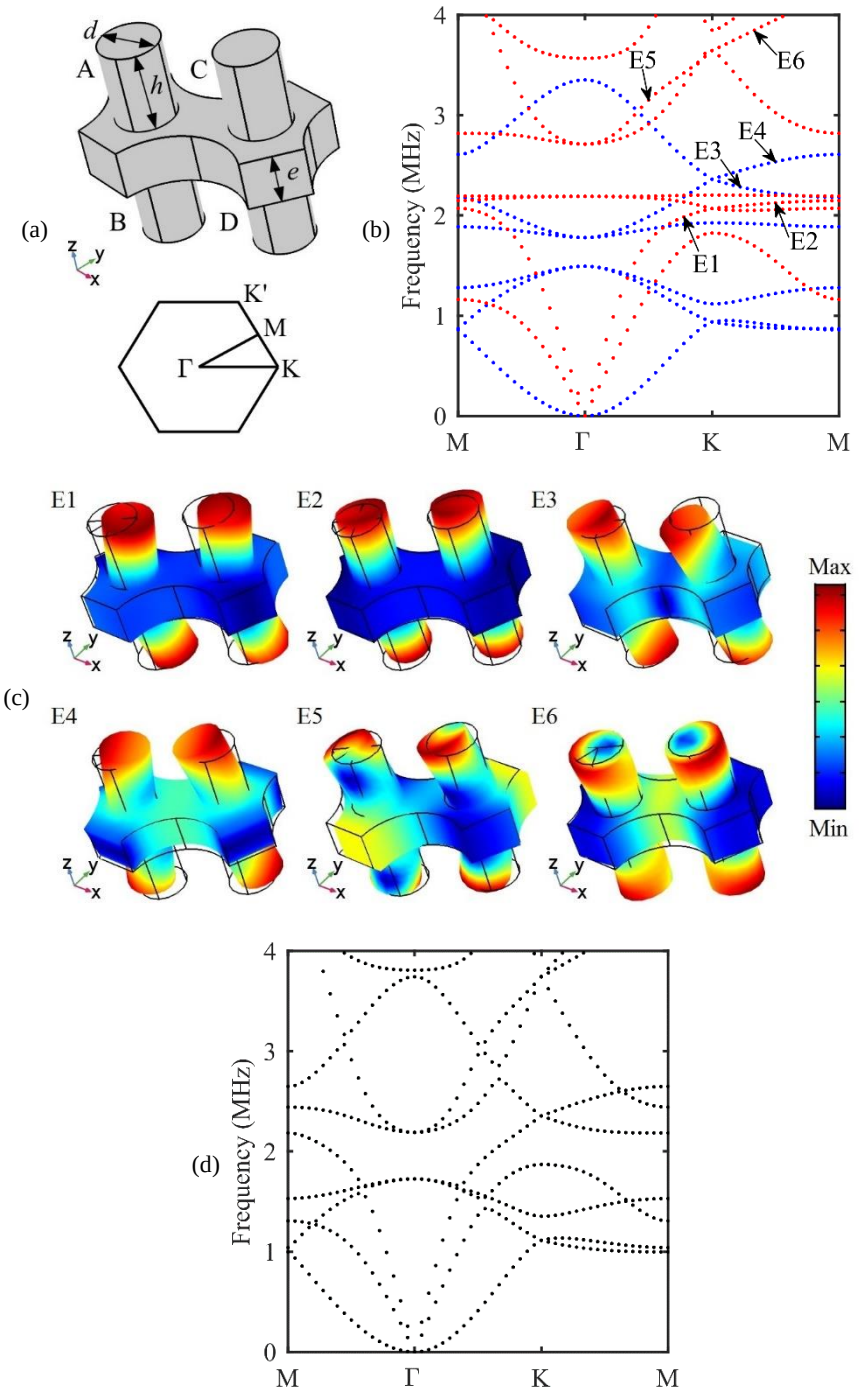

Figure 2.13: (a) Elementary unit cell of the proposed symmetric double-sided PPnC and (b) the corresponding band structure. (c) Eigenmodes at points labelled from E1 to E6 in (b). (d) Band structure of the single-sided PPnC by removing all the pillars on one side of the plate.

For comparison, the band structure of the single-sided PPnC, obtained by removing all the pillars on one side of the plate, is illustrated in figure 2.13(c). Two Dirac cones formed by the antisymmetric branches at 0.937MHz and 2.361MHz that can be seen in figure 2.13(b) at point K (K') of the BZ persist upon removing

all the pillars on one side, unlike the Dirac cone at 2.068MHz created by the symmetric branches. Considering the wavelengths of both Lamb modes involving the symmetric displacements, *i.e.* 2557 and 1513μm for S_0 and SH_0 modes respectively which are 6.393 and 3.783 times the lattice constant, therefore, the Dirac cone at 2.068MHz occurs in the deep subwavelength scale and should be attributed to the local resonances of the pillars.

To illustrate the tunable ability of this symmetric double-sided PPnC, the evolution of the band structure against the height of the pillars is studied. Figure 2.14 displays the band structures with the height of the pillars set to be 80μm, 120μm, 160μm and 200μm respectively. Globally, the band structure shifts to the lower frequency regime while increasing the height of the pillars and the interval between the first Dirac cone constructed by the symmetric branches and the second Dirac cone constructed by the antisymmetric branches can be judiciously tailored. Further, we will demonstrate that these two single Dirac cones can even overlap at the same frequency creating a double Dirac cone with optimized parameters. More specifically, a second Dirac cone formed by the symmetric branches occurs at frequency 5.916MHz (4.32MHz) when the height of the pillars is chosen to be 80μm (120μm).

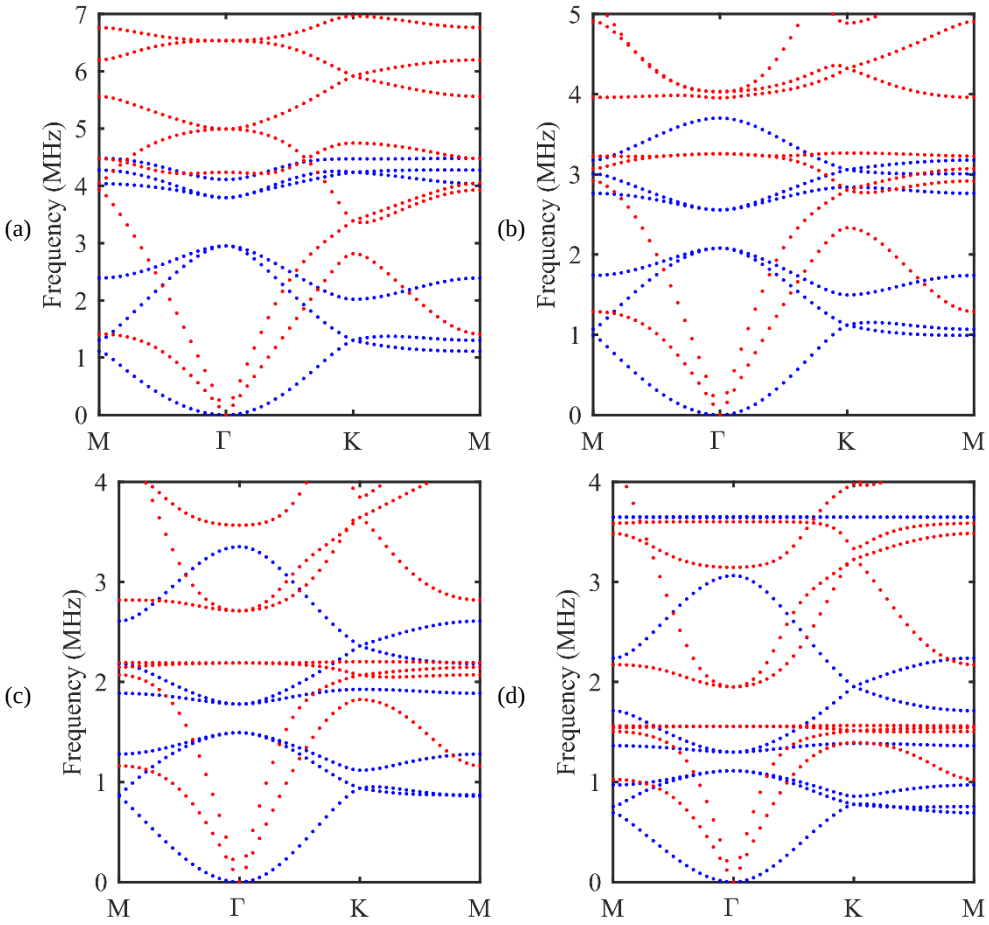

Figure 2.14: Band structures of the symmetric double-sided PPnCs with the height of the pillars set to be (a) 80μm, (b) 120μm, (c) 160μm and (d) 200μm respectively.

2.4.2 Emulating QVHE

2.4.2.1 Topological phase transition

As mentioned in Sec. 2.3.2, the space-inversion symmetry breaking perturbation must be imposed on the unit cell to introduce the topological phase transition. In this symmetric double-sided system, it can be realized by perturbing either the height or the diameter of the pillars while always reserving the mirror-symmetric about the mid-plane of the plate. Firstly, the diameter perturbation with $d_A = d_B = D + \Delta d_V$ and $d_C = d_D = D - \Delta d_V$ is imposed. For example, the band structure with the diameter perturbation $\Delta d_V = 4\mu m$, which can be recognized as a small space-inversion symmetry breaking strength, is displayed in figure 2.15(d). Two Dirac cones get lifted, thus leading to two nontrivial band gaps. Afterwards, the energy flux together with the phase distribution of the out-of-plane displacement at the bounding of the lifted Dirac cones are shown in figure 2.15(b) and (c) for the symmetric and antisymmetric band structure subcomponents respectively. Unambiguously, the clockwise and anticlockwise vortex chirality can be observed which can be recognized as the valley pseudospin down and up states. Considering the time-reversal symmetry in the system, at the opposite valley K' the valley pseudospin states are inverted. Figure 2.15(d) depicts the evolution of the valley pseudospin states against the diameter perturbation. The red and blue crosses (circles) represent the valley pseudospin down (up) states. When crossing zero, their frequency order is inverted and the band gap firstly closes and then reopens which is the signature of the topological phase transition. Besides, upon the same perturbation, a relatively broader band gap reopens for the antisymmetric band structure subcomponent that suggests its sensitivity to the diameter perturbation. Secondly, the perturbation in the height of the pillars with $h_A = h_B = H + \Delta h_V$ and $h_C = h_D = H - \Delta h_V$ is applied. Figure 2.15(e) plots the dependence of the valley pseudospin states on the height perturbation. In contrast, the symmetric band structure subcomponent has a broader reopened band gap.

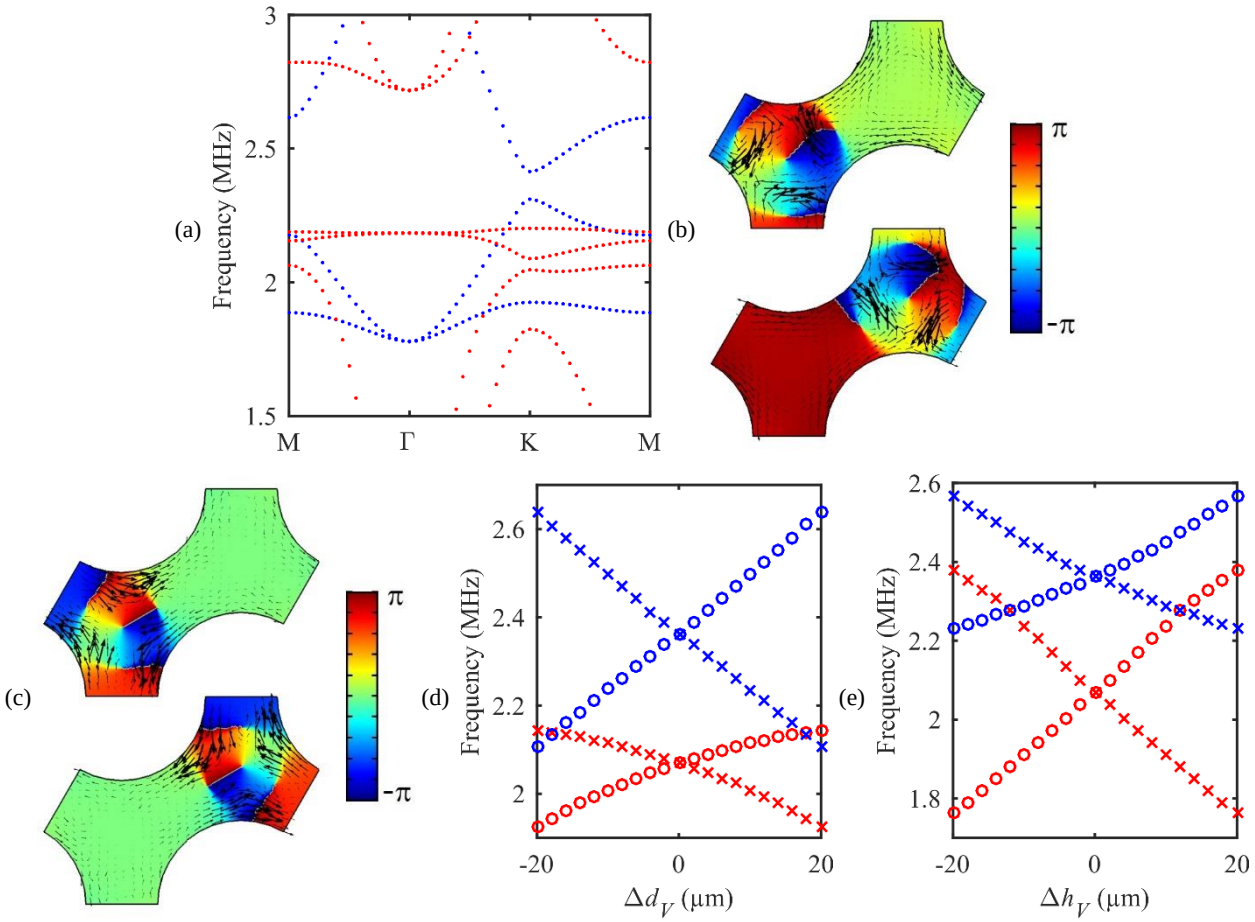

Figure 2.15: Band structure of the perturbed PPnC with the diameter perturbation Δdv = 4μm. Energy flux (black arrows) and phase distribution of the out-of-plane displacement at the lower (bottom panel) and higher (top panel) bounding of the lifted Dirac cone at the valley K for the (b) symmetric and (c) antisymmetric band structure subcomponents. Evolutions of the valley pseudospin states against the (d) diameter and (e) height perturbation at the valley K.

Subsequently, the Berry curvature is numerically computed. Figure 2.16(a) and (b) show the results at the lower bounding for the antisymmetric and symmetric band structure subcomponents at the wave vectors varying from $k_x = 2\pi/3a$ to $k_x = 10\pi/3a$ and $k_y = 0$. Two opposite valleys are well separated that suggests the suppression of the inter-valley scattering. Figure 2.16(c) and (d) display the distribution of the Berry curvature in the vicinity of the valley K. Theoretically, it converges quickly to $C_V(\mathrm{K/K'}) = \mp 1/2$. As for the higher bounding of the lifted Dirac cone, the results will change the sign to be positive [see figure 2.17(a) and (b)]. With regard to the antisymmetric band structure subcomponent, the peak values at the lower and higher bounding are exactly consistent. Nevertheless, for the symmetric band structure subcomponent, the peak value at the lower bounding changes slightly from the one at the higher bounding.

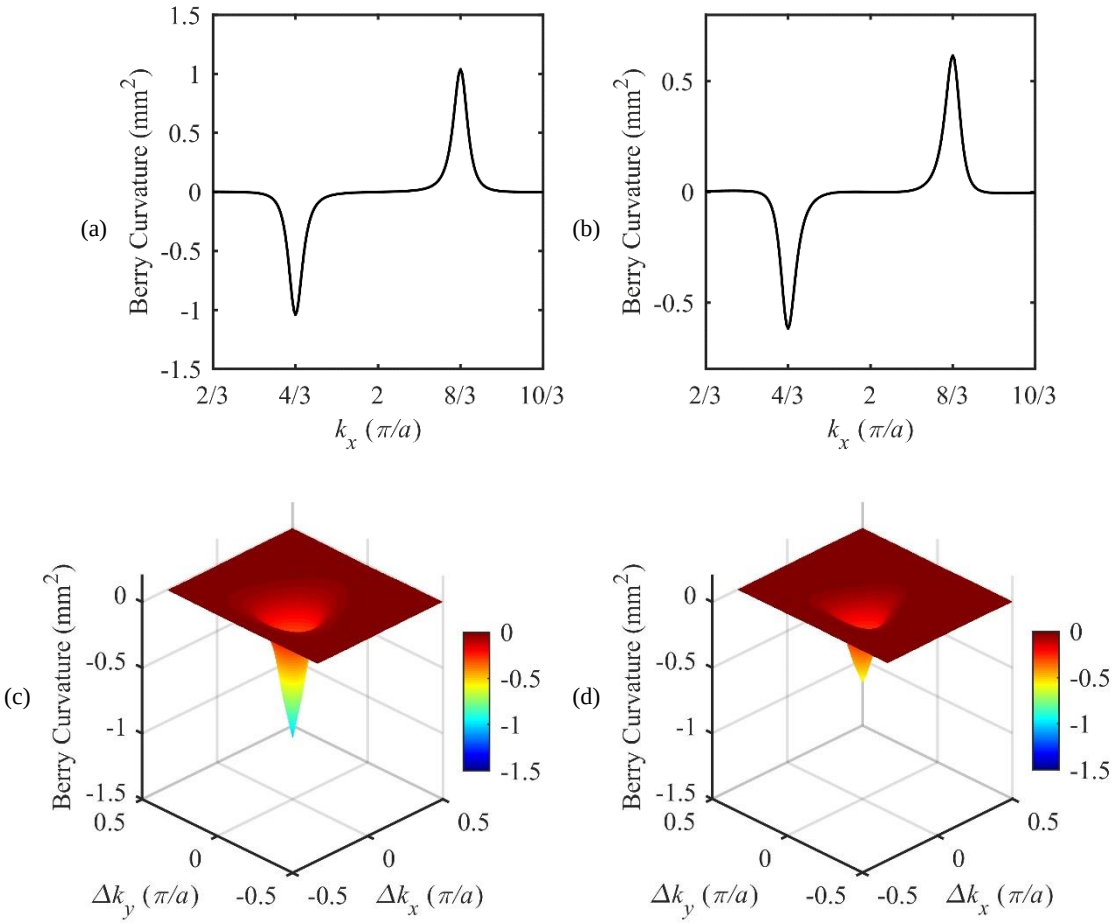

Figure 2.16: Numerical results of the Berry curvature of the lower bounding of the lifted Dirac cones: at the wave vectors varying from $k_x = 2\pi/3a$ to $k_x = 10\pi/3a$ and $k_y = 0$ for the (a) antisymmetric and (b) symmetric band structure subcomponents and in the vicinity of the valley K for the (c) antisymmetric and (d) symmetric band structure subcomponents.

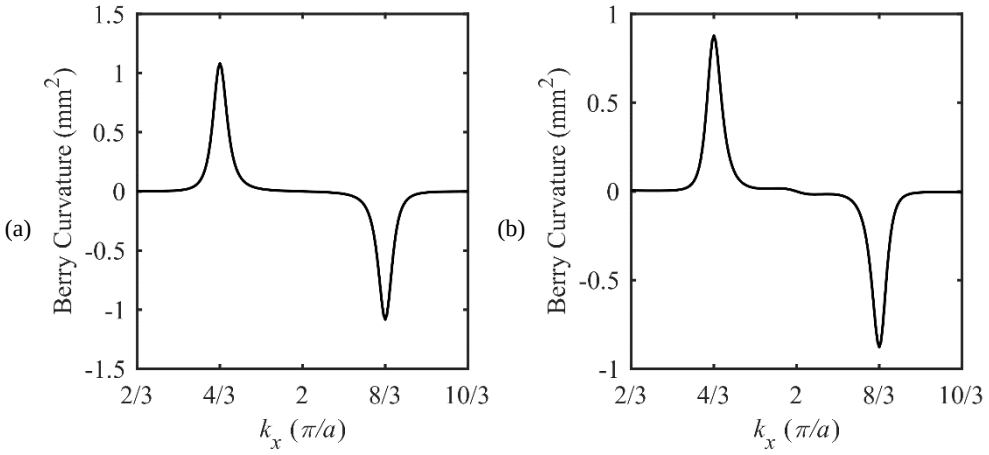

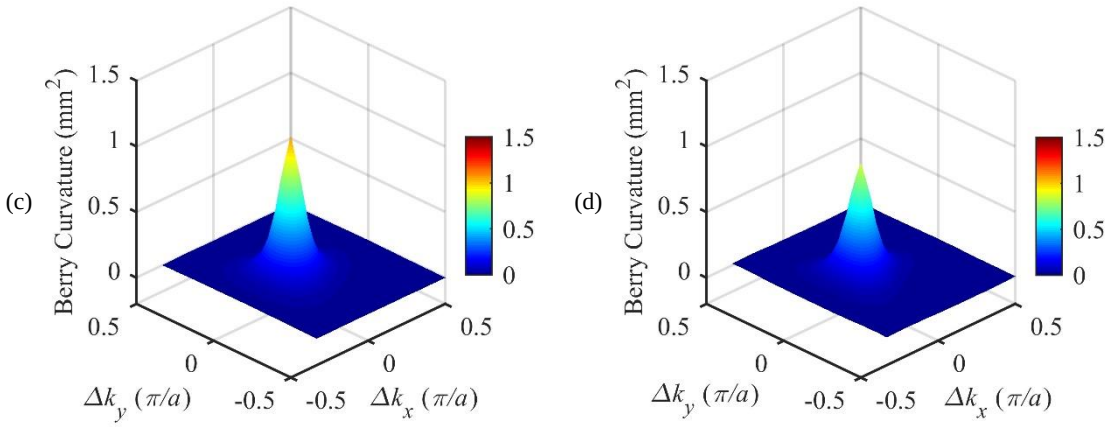

Figure 2.17: Numerical results of the Berry curvature of the higher bounding of the lifted Dirac cones: at the wave vectors varying from $k_x = 2\pi/3a$ to $k_x = 10\pi/3a$ and $k_y = 0$ for the (a) antisymmetric and (b) symmetric band structure subcomponents and in the vicinity of the valley K for the (c) antisymmetric and (d) symmetric band structure subcomponents.

2.4.2.2 Valley-protected edge states of the antisymmetric dispersion curves

To study the associated topologically protected edge states, we construct a three-layers ribbon supercell as sketched in figure 2.18(a). It sandwiches eight unit cells with the diameter perturbation $\Delta d_V = -10\mu m$ (type-IV) in between two sets of six unit cells with the diameter perturbation $\Delta d_V = 10\mu m$ (type-III). It should be mentioned that the larger diameter perturbation is applied to reopen a relatively broader band gap. Two zigzag domain walls are formed. The diameter of the adjacent pillars is decreased at SDW and increased at LDW. Firstly, we concentrate on the antisymmetric dispersion curves of the ribbon supercell as depicted in figure 2.18(b). Three newly branches can span through the reopened band gap. The eigenmodes of the magenta, the cyan and the black branches at the wave vector $k_x = 0.5\pi/a$ are presented in figure 2.18(c). It is found that the magenta and cyan dotted lines represent the edge states occurring at SDW and LDW respectively whereas the black dotted line denote the locally resonant mode at the top end where the pillars with small diameter are placed at the extreme end of the supercell. The edge state at SDW features the symmetric deformation about the interface, while the one at LDW the localized deformation turns antisymmetric. In this situation, the projection of the valleys K and K' on these two zigzag domain walls are $k_x = -2\pi/3a$ and $k_x = 2\pi/3a$ respectively. At the valley K, the edge state at SDW has a positive group velocity which is consistent with the valley Chern number difference of the higher bounding across the interface, *i.e.* $C_V^{\text{Type-III}}(\text{K}) - C_V^{\text{Type-IV}}(\text{K}) = 1$. Whereas at the valley K', the group velocity becomes negative.

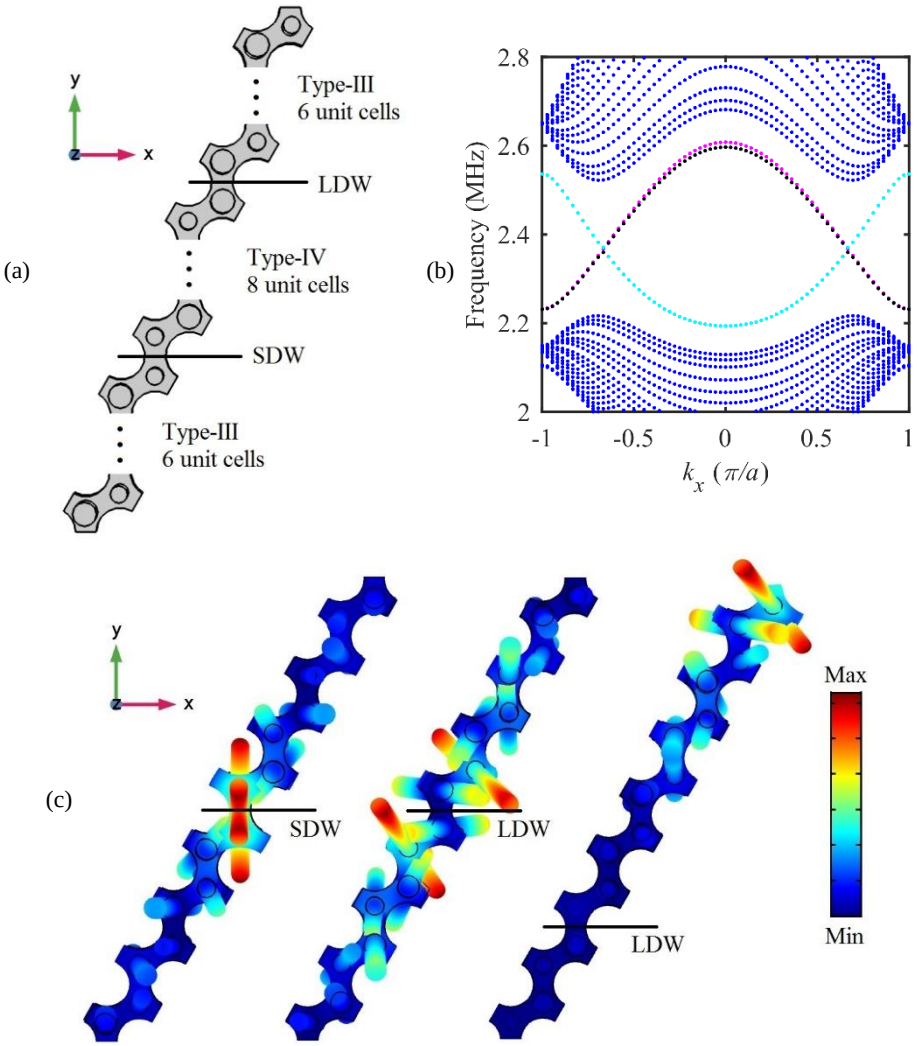

Figure 2.18: (a) Schematic of the proposed three-layers ribbon supercell constructed by sandwiching eight unit cells of type-IV PPnC in between two sets of six unit cells of type-III PPnC. (b) Antisymmetric dispersion curves of the ribbon supercell. (c) Eigenmode of the edge states (magenta and cyan branches) and locally resonant mode (black branch) at the wave vector $k_x = 0.5\pi/a$.

Thereafter, the propagation of the K-polarized edge state in the wave guide in figure 2.19(a) is studied. Type-III and type-IV PPnCs fill in the lower and upper regions respectively forming a SDW at the interface. A right-going wave at frequency 2.368MHz was launched by two phase-matched sources in the middle of the domain wall (red point). Figure 2.19(b) plots the out-of-plane displacement on the top surface of the plate. The edge state gets refracted at the right zigzag termination without any reflection which is guaranteed by the small space-inversion symmetry breaking strength and the valley conservation at the zigzag termination. Two refracted beams at the right outlet can be observed. Based on the relative position of the edge state and the refracted beams to the normal to the zigzag termination, they can be recognized as a positive one (on two sides of the normal) and a negative one (on the same side of the normal) respectively.

To interpret such refracted pattern, the equifrequency contours (EFCs) analysis is carried out as shown in figure 2.19(c). The edge states are locked to the valley K (three black dots) of the BZ (black solid line). The blue solid line represents the EFC of A_0 Lamb wave at the same frequency in the plate. The cyan dashed lines depict the normal to the right outlet. Owing to the conservation of the component of the wave vector parallel to the right outlet, two refracted wave vectors are graphically obtained (blue bold arrows) which are in good agreement with the displacement fields in figure 2.19(c). As mentioned in Sec. 2.4.1, the position of the Dirac cones can be modulated by the height of the pillars. It suggests that the refractive angles of the two refracted beams can be judiciously tuned as depicted in figure 2.19(d). Both the refractive angles increase as the height of the pillars grows, especially the negatively refractive one that quickly reaches the maximum value (90°) and then vanishes. To testify this, the height of the pillars was chosen to be $h_A = h_B = H = 220\mu m$. Upon the same diameter perturbation $\Delta d_V = 10\mu m$, the frequency of the K-polarized edge state decreases to 1.809MHz. The refraction pattern at the right zigzag outlet and the EFCs analysis are depicted in figure 2.19(e) and (f). Clearly, only one positively refracted A_0 Lamb wave remains.

From another point of view, owing to the time-reversal symmetry in the system, perfect coupling into the desired valley-polarized edge state can also be achieved by properly selecting an incident wave impinging from the surrounding plate to the zigzag termination. Depending on the height of the pillar, either one or two possible wave vectors is available.

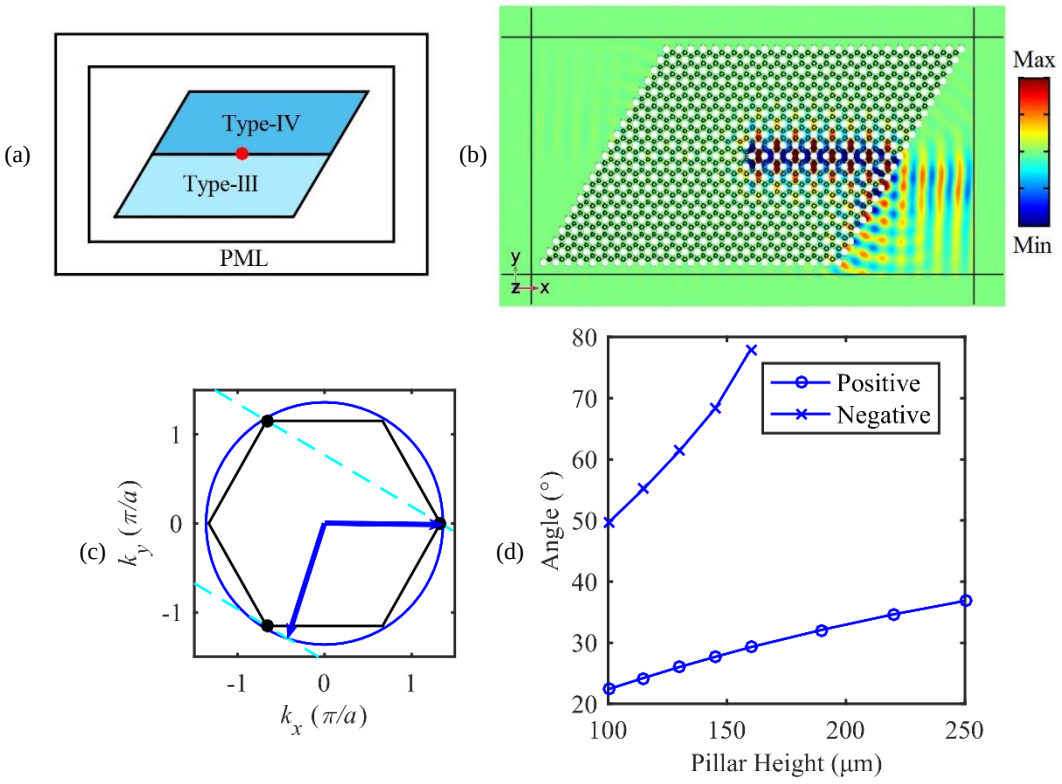

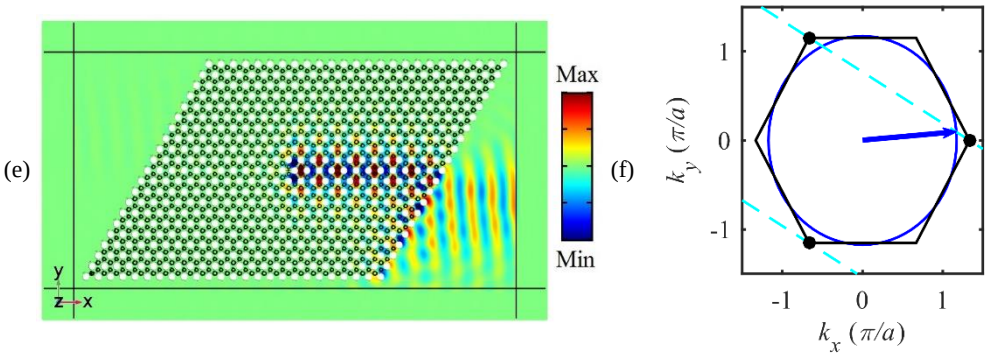

Figure 2.19: (a) Schematic of the straight wave guide constructed by placing type-III and type-IV PPnCs in the lower and upper regions respectively. (b) Plot of the out-of-plane displacement on the top surface of the plate under the excitation of the right-going edge state at frequency 2.368MHz that was launched in the middle. (c) EFCs analysis of the refracted pattern at the right zigzag termination. (d) Evolution of the refractive angles against the height of the pillars. (e) Plot of the out-of-plane displacement under the excitation right-going edge state at frequency 1.809MHz with the height of the pillars set to be $h_A = h_B = H = 220\mu m$ and the diameter perturbation $\Delta d_V = 10\mu m$. (f) Refracted pattern predicted by the EFCs analysis at frequency 1.809MHz.

The interaction between the right-going K-polarized edge state and the armchair termination [see figure 2.20(a)] is studied. Figure 2.20(b) plots the out-of-plane displacement field. Reflection at the right armchair outlet occurs owing to the breaking of the valley conservation. Thus, the left-going K'-polarized edge state is generated and gets refracted at the left outlet. More interestingly, three transmitted beams at the right outlet can be observed. This peculiar pattern can be well predicted by the EFCs analysis in figure 2.20(c). The blue bold wave vectors match the transmitted field very well. Besides, the EFC of A_0 Lamb wave in the plate (blue solid circle) will shrink if the frequency of the valley-polarized edge state decreases. When it locates inside the BZ, then the inclined transmitted beams will disappear. To evidence that, the evolution of the inclined angle against the height of the pillars predicted by the EFCs analysis is computed and displayed in figure 2.20(d). It is found that the angle increases as the height of the pillars grows. When the height of the pillars grows to be $h_A = h_B = H = 250\mu m$, only one transmitted beam remains which contains all the transmitted elastic energy as demonstrated in figure 2.20(e). The excitation frequency is set to be 1.651MHz.

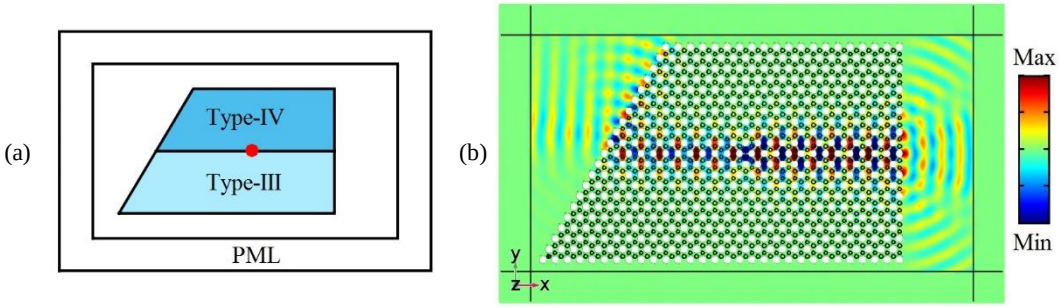

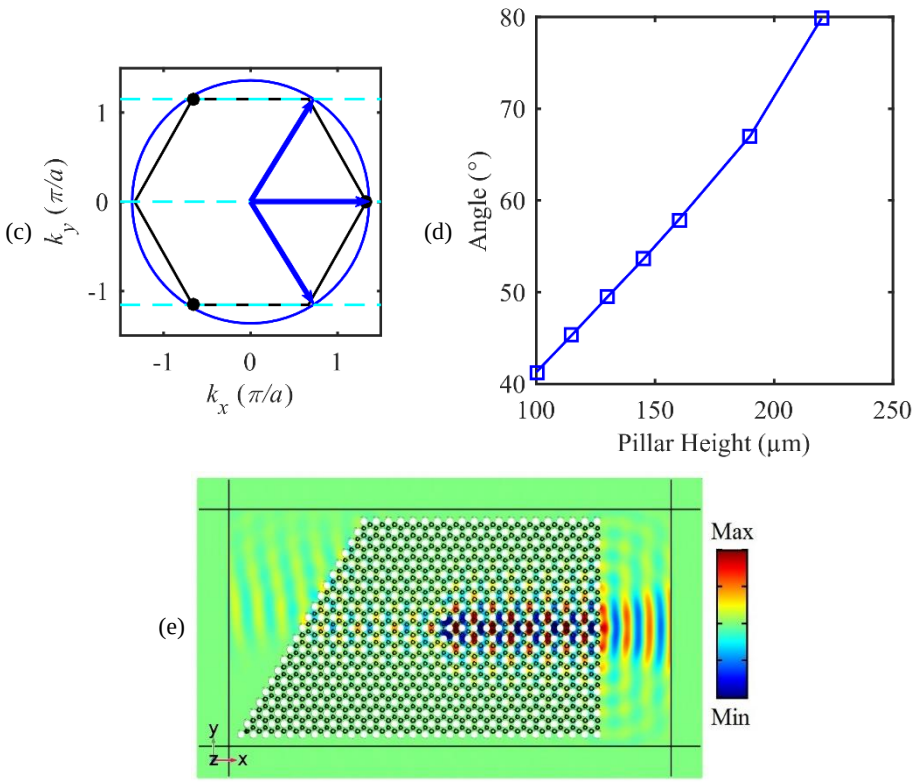

Figure 2.20: (a) Schematic of the straight wave guide constructed by placing type-III and type-IV PPnCs in the lower and upper regions respectively with the right termination set to be armchair type. (b) Plot of the out-of-plane displacement on the top surface of the plate understand the excitation of the right-going edge state at frequency 2.368MHz that was launched in the middle. (c) EFCs analysis of the transmitted pattern at the right armchair outlet. (d) Evolution of the inclined angles against the height of the pillars. (e) Plot of the out-of-plane displacement under the excitation of the K-polarized edge state at frequency 1.651MHz with the height of the pillars set to be $h_A = h_B = H = 250\mu m$ and the diameter perturbation $\Delta d_V = 10\mu m$.

2.4.2.3 Valley-protected edge states of the symmetric dispersion curves

Secondly, in this part, we are going to discuss the topologically valley-protected edge state associated with the symmetric Lamb modes. Figure 2.21 displays the symmetric dispersion curves of the ribbon supercell. Three newly branches appear in the reopened band gap. The eigenmodes of the magenta, the cyan and the black branches at the wave vector $k_x = 0.5\pi/a$ are shown in figure 2.21(b). As stated by the deformation in the eigenmodes, the magenta and cyan dotted lines represent the edge states occurring at SDW and LDW respectively whereas the black dotted line denotes the locally resonant mode at the bottom end where the pillars with large diameter are placed at the extreme end of the supercell. Besides, the adjacent pillars exhibit the symmetric deformation about the interface at SDW and the antisymmetric deformation about the interface at LDW. However, the edge states could not span the whole reopened band gap and leave a completely forbidden band in between 2.083MHz and 2.121MHz.

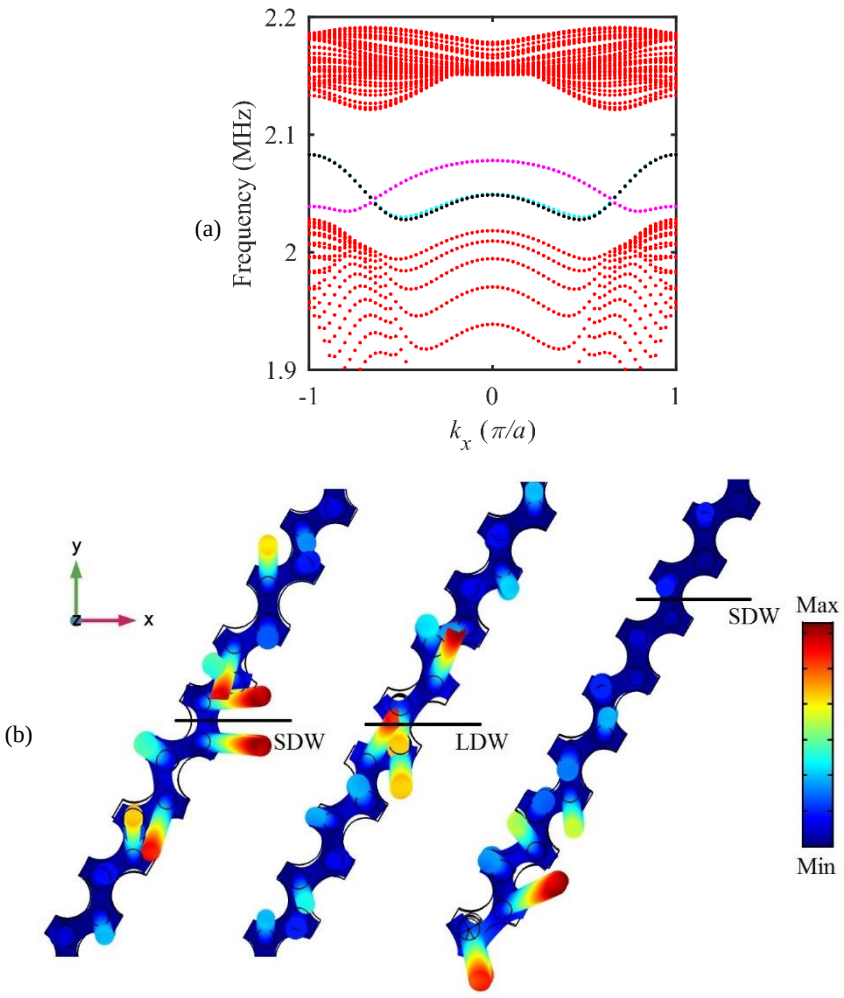

Figure 2.21: (a) Symmetric dispersion curves of the ribbon supercell. (b) Eigenmode of the edge states (magenta and cyan branches) and locally resonant mode (black branch) at the wave vector $k_x = 0.5\pi/a$.

As mentioned before, the original Dirac cone occurs in the deep subwavelength scale and the wavelengths of S_0 and SH_0 waves at the same frequency in the plate are much larger than the lattice constant. It will play an important role in understanding the abnormal wave patterns at the zigzag termination. The propagation of the topological edge state in the wave guide in figure 2.20(a) is analyzed. A K'-polarized left-going wave at frequency 2.042MHz was launched in the middle of the domain wall. The magnitude of the in-plane displacement and the out-of-plane displacement on the top surface of the plate are displayed in the left and right panels of figure 2.22(a) respectively. In the left panel, the black arrows render its polarization that reveals its SH polarized feature. The edge state turns downwards and mostly remains localized at the zigzag outlet, even though some elastic energy spreads across the plate and a small portion propagates along the bottom interface. In the right panel, similar phenomenon can be observed. Most of the energy is localized at the interface. More interestingly, a circular shape wave field occurs in the plate that suggests the topologically protected edge state actually performs as point sources at the end of the wave guide.

The EFCs analysis depicted in figure 2.22(c) can help to interpret the wave pattern in the outer plate. The red and green solid lines are the EFCs for S_0 and SH_0 modes in the plate at the same frequency. The edge state is locked to the valley K' (three black dots) of the BZ (black solid line). Owing to the extremely small wave vector of S_0 and SH_0 waves in the plate, the refracted wave vector becomes imaginary and therefore the refracted wave would turn to be evanescent. However, at the zigzag outlet interface, due to the coupling with the locally resonant mode occurring at the edge ending with pillars having a large diameter [see the zoomed view of the left bottom corner in figure 2.22(d)], the evanescent wave is strongly enhanced. In contrast, there is no vibration enhancement if the resonant pillars (highlighted in blue in the zoomed view) are removed as shown in figure 2.22(b). This well explains that the magnitude at the bottom interface is nearly zero.

From another point of view, the extremely small group velocity at the original Dirac cone can lead the edge states to attenuate very quickly into the neighboring PPnCs according to the decay factor derived in Ref. [42]. Therefore, the edge state would be strongly localized around the domain wall. When compared to the much larger wavelengths in the plate, it can be well understood that the edge state should function as point sources when it arrives at the end of the domain wall and the interference of the wave fields generated by these neighboring point sources contributes to the different wave patterns in the plate. Therefore, it can be stated in the deep subwavelength scale that the valley-protected edge state can convert to the evanescent wave and also behaves as point sources when it arrives the end of the domain wall.

(a)

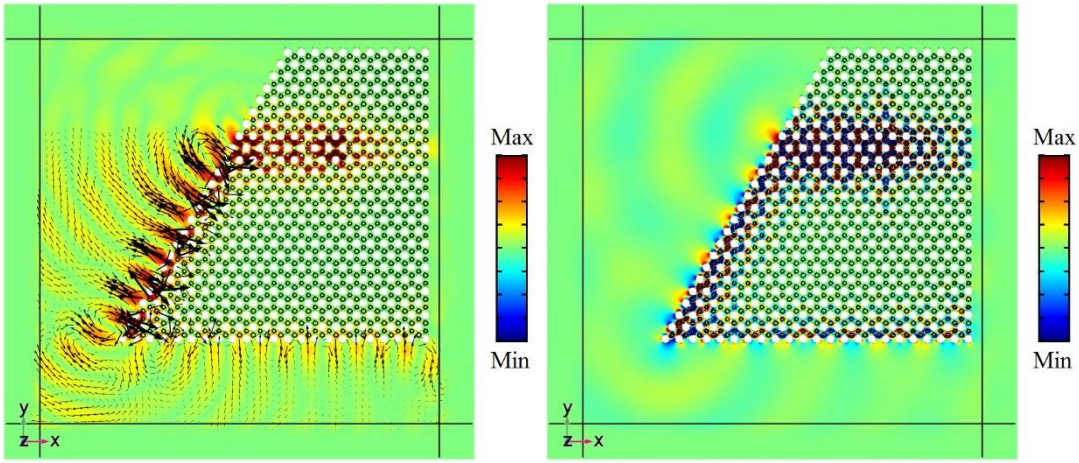

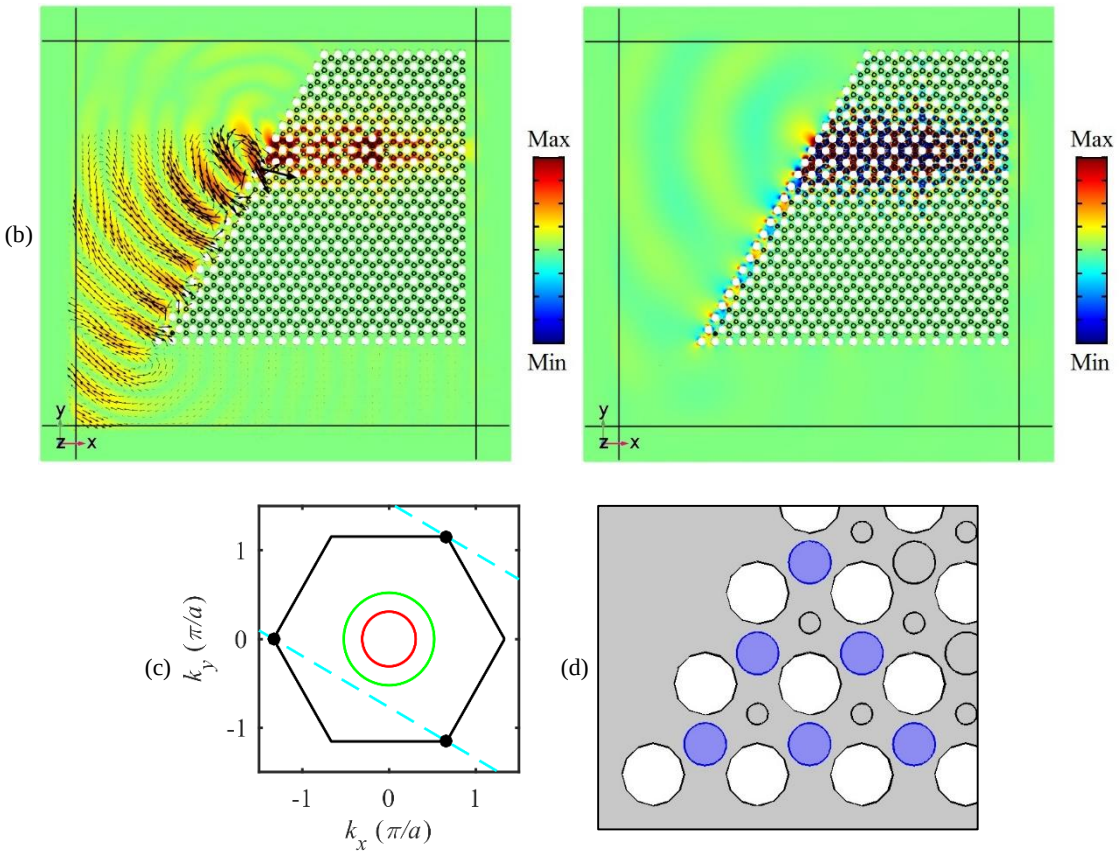

Figure 2.22: Plots of the magnitude of the in-plane displacement (left panel) and the out-of-plane displacement (right panel) on the top surface of the plate under the excitation of the left-going K'-polarized edge state at frequency 2.042MHz that was launched in the middle (a) with and (b) without the resonant pillars. (c) EFCs analysis of the refracted pattern at the left zigzag termination. (d) Zoomed view of the left bottom corner in (a) and (b).

Considering the time-reversal symmetry in the system, the evanescent wave propagating at the interface might be capable to convert to the topological edge state. A point source is placed at the bottom interface and a z-polarized harmonic force at frequency 2.042MHz is applied, thus can generate the evanescent wave propagating along the interface. The left and right panels in figure 2.23 display the magnitude of the in-plane displacement and the out-of-plane displacement respectively. In both panels, the evanescent wave localized at the interface turns upwards and couples to the right-going K-polarized edge state which provides a fascinating way to collect the evanescent wave.

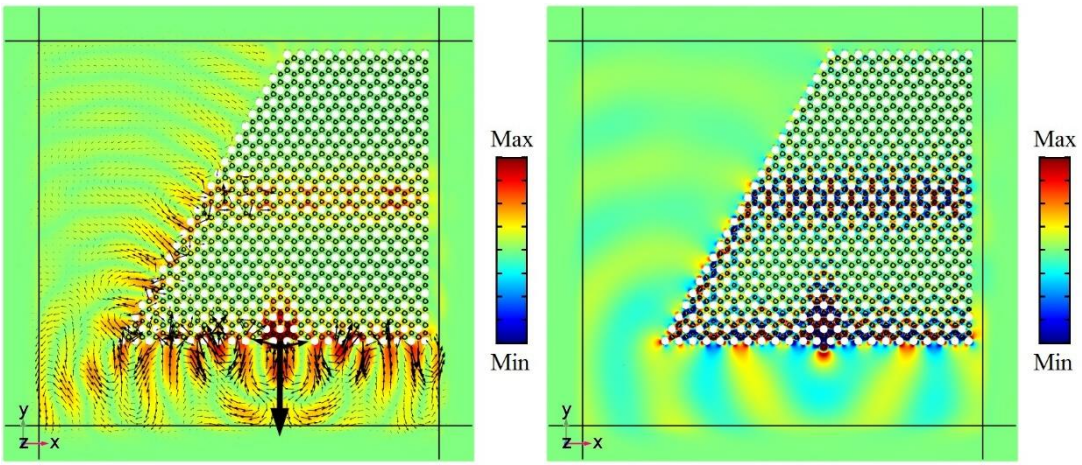

Figure 2.23: Plots of the magnitude of the in-plane displacement (left panel) and the out-of-plane displacement (right panel) on the top surface of the plate under the excitation of a *z*-polarized point source at the bottom interface.

In the following, the interaction between the K'-polarized edge state and the armchair termination is presented. Figure 2.24(a) plots the magnitude of the in-plane displacement and the out-of-plane displacement respectively. Even though the valley conservation at the left outlet is broken, most of the elastic energy gets transmitted directly regardless of the large impedance mismatch. Figure 2.24(b) and (c) show the transmitted pattern predicted by the EFCs analysis with the transmitted wave assumed to be SH_0 and S_0 modes separately. For each Lamb mode, only one transmitted beam can be obtained. However, the transmitted SH_0 mode would not occur because it is against the symmetry of the displacement field about the domain wall due to its specific polarization. It can be evidenced by the horizontal polarization vectors in the left panel of Figure 2.24(a). Moreover, the transmitted wave has almost a circular shape profile which is quietly different from the transmitted field of A_0 Lamb mode displayed in figure 2.20(b). It can be well explained by considering that the edge state acts at points sources [see the energy spots at the outlet in the left panel of figure 2.24(a)] once arriving at the armchair termination.

(a)

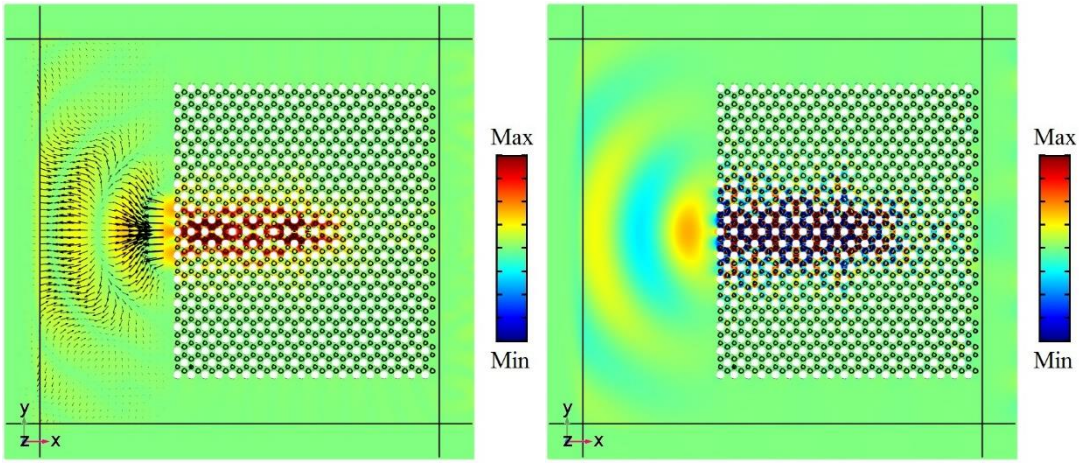

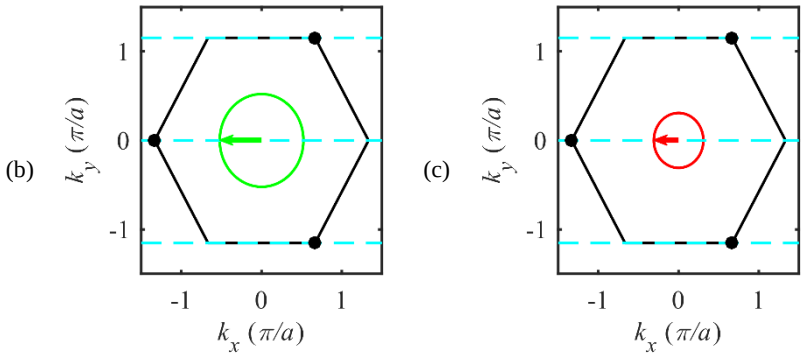

Figure 2.24: (a) Plots of the magnitude of the in-plane displacement (left panel) and the out-of-plane displacement (right panel) under the excitation of the K'-polarized edge state at frequency 2.042MHz. EFCs analysis of the transmitted pattern at the left armchair outlet with the transmitted wave assumed to be (b) SH_0 and (c) S_0 Lamb mode respectively.

As discussed above, the valley-polarized edge state cannot be refracted at the zigzag termination owing to the extremely small wave vector in the surrounding plate that might potentially restrict its practical application. To deal with this issue, one needs to increase the frequency of the edge state and ensure its occurrence in the high frequency regime. Here, we consider another configuration with the height of the pillars set to be $h_A = h_B = D = 80\mu m$. The band structure is already displayed in figure 2.14(a) where a second Dirac cone formed by the symmetric branches occurs at frequency 5.916MHz. After imposing the same diameter perturbation $\Delta d_V = 10\mu m$ (type-V), the higher Dirac cone gets lifted in figure 2.25(a) which leads to a nontrivial band gap ranging from 5.746MHz to 6.096MHz. Then, the juxtaposition with its inverted counterpart $\Delta d_V = -10\mu m$ (type-VI) allows for the occurrence of the topologically valley-protected edge state at the domain walls. To verify that, we consider a three-layers ribbon supercell by replacing type-III and type-IV PPnCs in figure 2.18(a) with type-V and type-VI PPnCs respectively. Figure 2.25(b) depicts the symmetric dispersion curves. Two topologically protected edge states labelled as the magenta and cyan dotted lines occur at SDW and LDW respectively and the black dotted line denotes the locally resonant mode at the top end where the pillars with decreased diameter are placed at the extreme end of the supercell. The eigenmodes of the edge states and the localized mode at the wave vector $k_x = 0.5\pi/a$ are illustrated in figure 2.25(c). It can be seen that the localized deformation is the mixture of the symmetric bending and torsion. Moreover, the localized elastic field is symmetric about the interface at SDW, whereas antisymmetric about the interface at LDW. It also suggests that an incident S_0 Lamb wave can propagate at SDW where an incident SH_0 wave will be totally reflected at the inlet. In contrast, the propagation of S_0 Lamb wave is forbidden at LDW and an incident SH_0 mode becomes propagative.

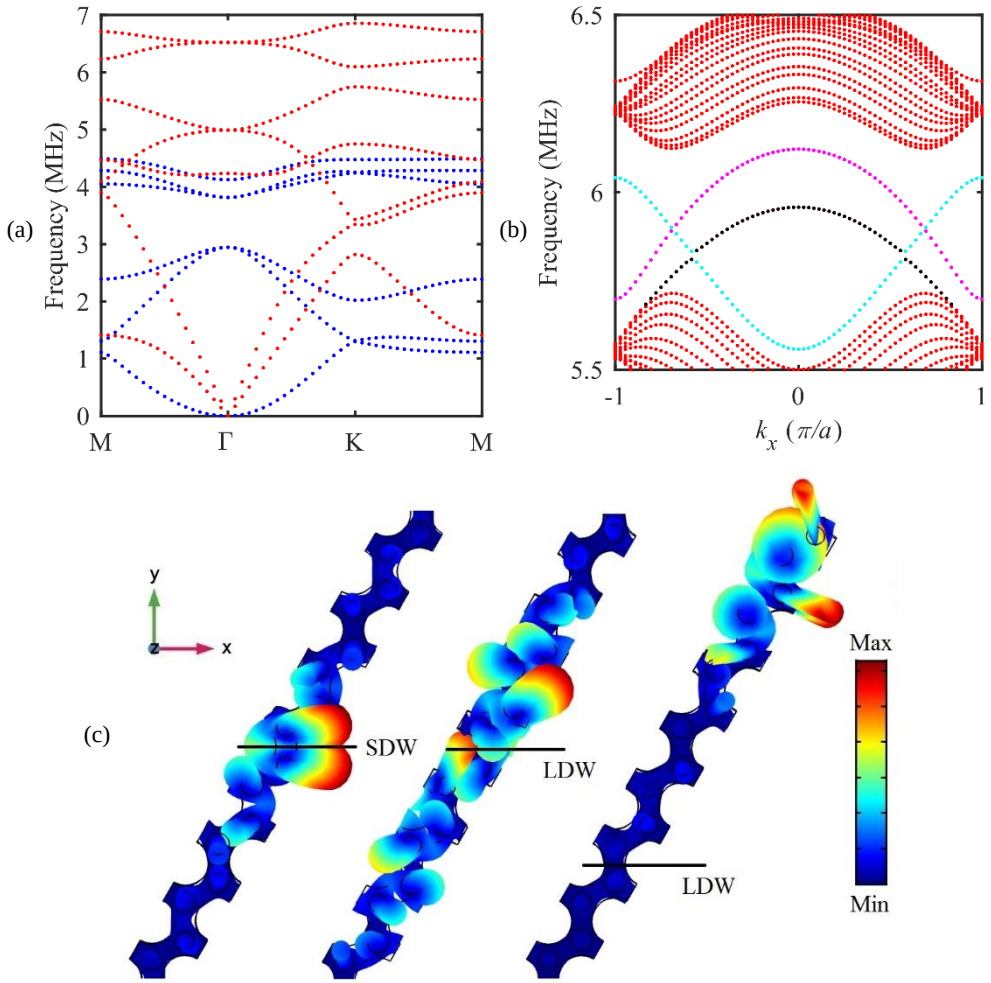

Figure 2.25: (a) Band structure of the perturbed PPnC with the diameter perturbation Δd_V = 10μm. (b) Symmetric dispersion curves of the ribbon supercell. (c) Eigenmodes of the edge states (magenta and cyan branches) and the locally resonant mode (black branch) at the wave vector $k_x = 0.5\pi/a$.

Considering the straight wave guide in figure 2.26(a) built by placing type-V and type-VI PPnCs in the lower and upper regions, thus it constructs a SDW at the interface. Both the left and right outlets are set to be zigzag type. Then, the propagation of the right-going K-polarized edge state at frequency 5.909MHz at the domain wall is studied. Figure 2.26(a) displays the in-plane displacement components u_x and u_y in the left and right panels respectively. In the left panel, two refracted beams can be observed. While in the right panel, it only contains one positively refracted wave. After that, we perform the EFCs analysis of the refraction at the right zigzag outlets and the results are shown in figure 2.26(b). Firstly, we assume the refracted wave to be only S_0 Lamb wave (see the left panel). A positively refracted S_0 Lamb mode (48°) occurs and denoted by the red bold arrow. Secondly, the refracted wave is assumed to be SH_0 wave. Both the positively (26.2°) and negatively (62°) refracted beams (green bold arrows) emerge as displayed in the right panel. Further, two-dimensional Fourier transform of the in-plane displacement components u_x and u_y

inside the red dashed rectangle sketched in figure 2.26(a) is performed to verify the above analysis and presented in figure 2.26(c). In the left panel, the positively refracted S_0 Lamb mode and the negatively refracted SH_0 mode occur. And in the right panel, the positively refracted SH_0 mode appears. Both the refractive angles are consistent with the results predicted by the EFCs analysis (red and green dashed lines).

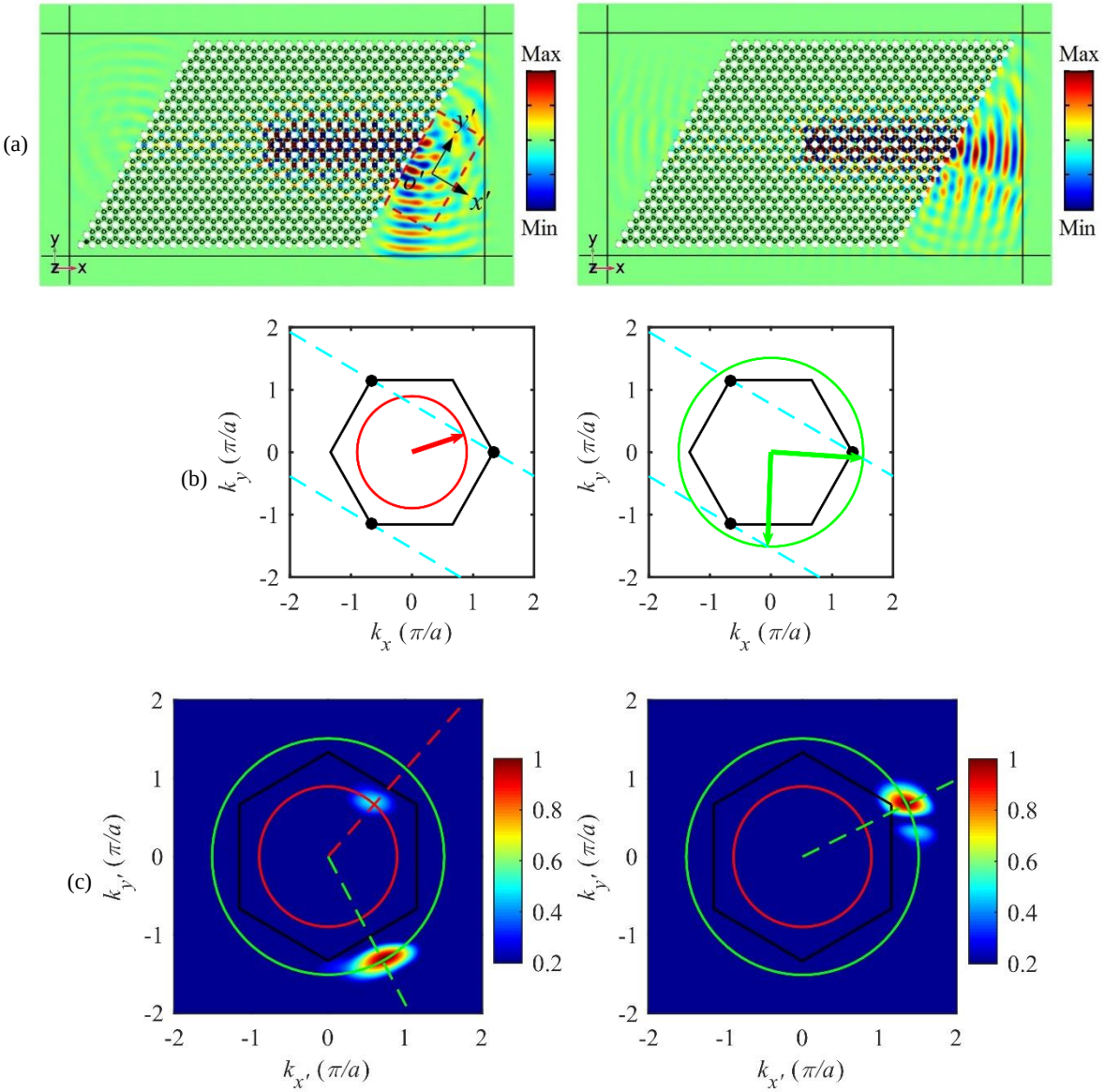

Figure 2.26: (a) Plots of the in-plane displacement components u_x (left panel) and u_y (right panel) on the top surface of the plate under the excitation of the right-going K-polarized edge state at frequency 5.909MHz. (b) EFCs analysis of the refraction at the right zigzag outlet with the refracted wave assumed to be only S_0 (left panel) and SH_0 (right panel) Lamb waves respectively. (c) Two-dimensional Fourier transform of the in-plane displacement components u_x (left panel) and u_y (right panel) shown in the red rectangle in (a).

Figure 2.27(a) plots the magnitude of the in-plane displacement and the out-of-plane displacement on the top surface of the plate when the K'-polarized left-going edge state at frequency 5.909MHz impinging on

the armchair termination. In the left panel, two main transmitted wave occurs in the plate which are mainly SH polarized. According to the EFCs analysis shown in figure 2.27(b), it consists of three transmitted SH_0 beams. Actually, only two inclined SH_0 modes will exist in the transmitted field and the one along the negative *x*-axis will not occur because it violates the symmetry of the displacement field about the domain wall. The inconsistency of the inclined angle can be attributed to the superposition with S_0 Lamb mode. In the right panel of figure 2.27(a), the out-of-plane displacement of the transmitted field exhibits three transmitted S_0 beams. As predicted by the EFCs analysis in figure 2.27(c), only one S_0 Lamb wave could exist. It is suggested that the other two beams might come from the interference of the point sources at the armchair outlet. To support this assumption, we consider three point sources with the interval 600μm symmetrically arranged at the end of the domain wall. The superposition of the generated wave field by these point sources is plotted in figure 2.27(d) that shows the similar profile with the one in the right panel of figure 2.27(a). At this point, it confirms with the previous conclusion that in the subwavelength scale the edge state performs as point sources at the outlet termination.

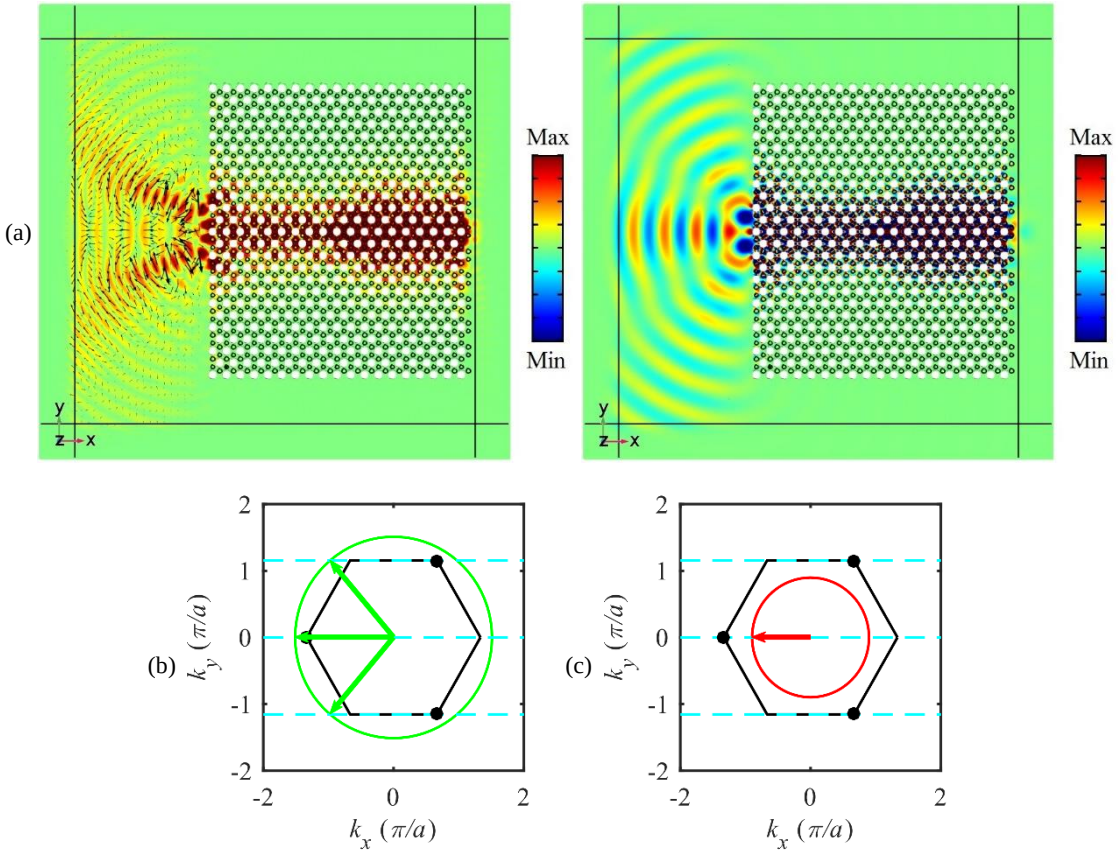

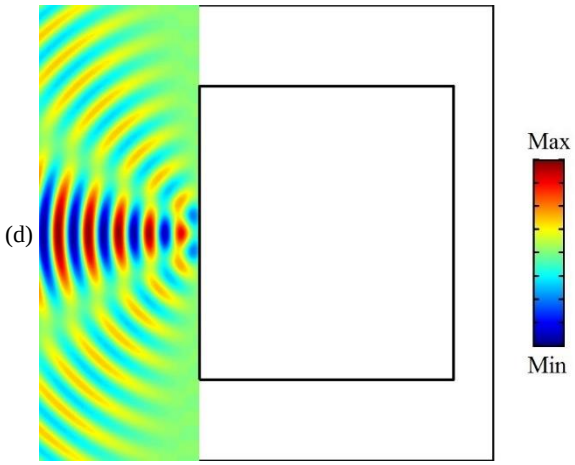

Figure 2.27: (a) Plots of the out-of-plane displacement (left panel) and the magnitude of the in-plane displacement (right panel) under the excitation of the K'-polarized edge state at frequency 5.909MHz. EFCs analysis of the transmitted pattern at the left outlet with the transmitted wave assumed to be (b) S_0 and (c) SH_0 mode respectively. (d) Generated wave field by assuming three point sources separated by 600μm at the interface.

2.4.3 Emulating QSHE

2.4.3.1 Topological phase transition

The proximity of the Dirac cones of the symmetric and antisymmetric band structure subcomponents in figure 2.14 suggests that they might overlap if the dimensions of the unit cell are properly designed, giving rise to a double Dirac cone and then to emulate QSHE. This is indeed the case when $d_A = d_B = d_C = d_D = D$ = 80μm, $h_A = h_B = h_C = h_D = H$ = 153.6μm, d_H = 320μm, and e = 70μm. The band structure is shown in figure 2.28(a). The double Dirac cone occurs at frequency 1.781MHz. As well known, to emulate QSHE, one needs to break the mirror-symmetry about the mid-plane of the plate. To achieve that, we impose the perturbation in the height of the pillars with $h_A = h_D = H + \Delta h_S$ and $h_B = h_C = H - \Delta h_S$. Then, the double Dirac cone is lifted and the symmetric and antisymmetric modes hybridize near the original double Dirac cone which can introduce the spin-orbit coupling interaction. Within this framework, the in-phase and out-of-phase hybridization can be adopted as the effective pseudospin up and down states respectively [33]. The band structure for Δh_S = 3μm (type-VII) is displayed in figure 2.28(b). The double Dirac cone splits into two single ones and a nontrivial complete band gap reopens in between 1.763MHz and 1.82MHz. Furthermore, the comparison with figure 2.28(a) reveals that the lower (upper) Dirac cone combines the lower (upper) symmetric and antisymmetric modes. Figure 2.28(b) and (d) illustrate the eigenmodes at the lower and higher Dirac cones which confirms the pairwise hybridization. Thereafter, the Berry curvature of the four constituent four branches of the original double Dirac cones in the vicinity of the valley K is numerical evaluated and shown in figure 2.29(a)-(d). It is found that the Berry curvature is strongly localized around the valley K which is quietly different from the broad distribution in figure 2.7 and figure 2.17. The

large separation between the opposite valleys can be always ensured in this situation that makes the corresponding topological edge states much more robust. By integrating the Berry curvature over the valley sectors, the spin Chern number converges theoretically to be $C_s^{\uparrow\downarrow}(\mathrm{K/K'}) = \mp 1/2$. When the height perturbation is changed to $\Delta h_S = -3\mu m$ (type-VIII), the spin Chern number will turn to be $C_s^{\uparrow\downarrow}(\mathrm{K/K'}) = \pm 1/2$.

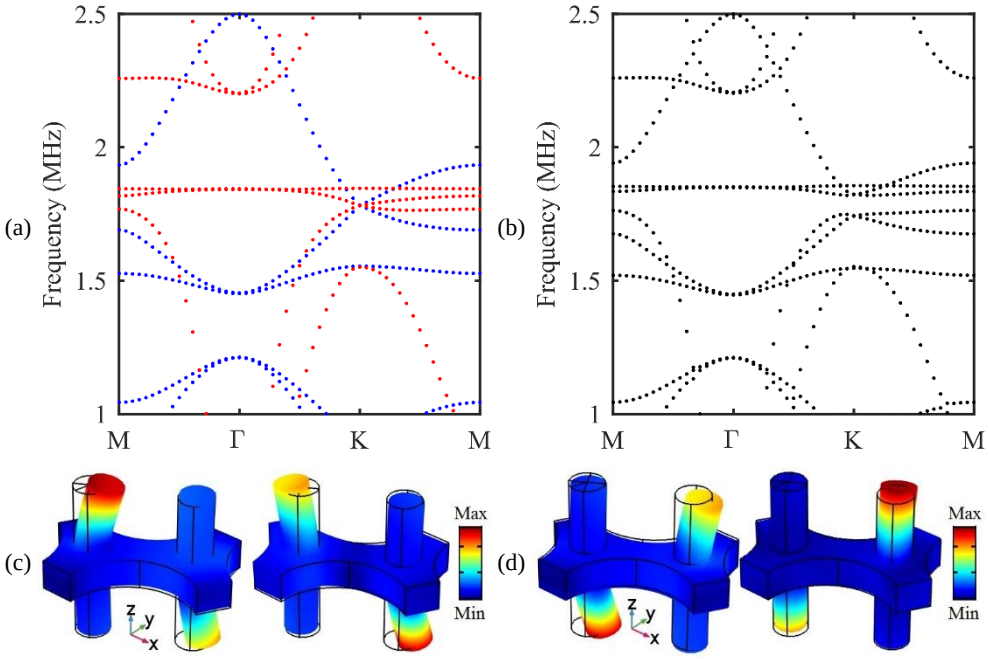

Figure 2.28: (a) Occurrence of the double Dirac cone. (b) Lifting of the double Dirac cone after imposing the height perturbation $\Delta h_S = 3\mu m$. Eigenmodes at the (c) lower and (d) higher Dirac cones respectively.

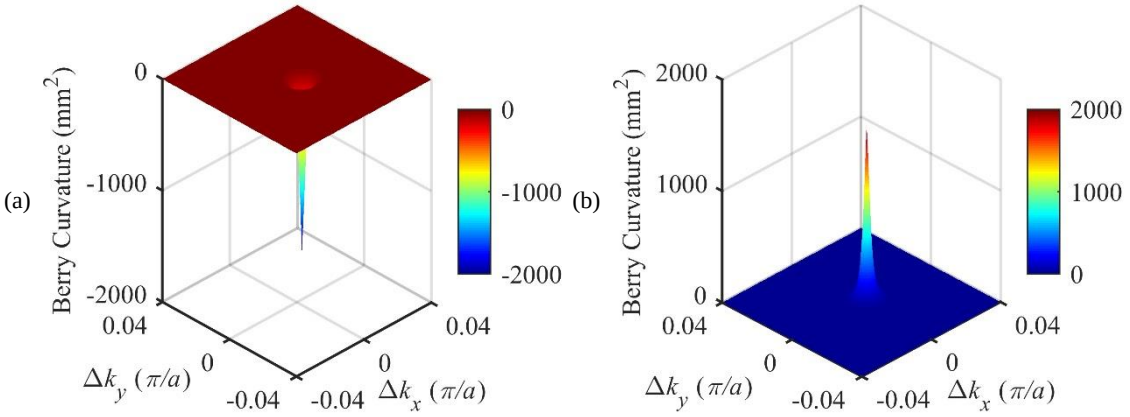

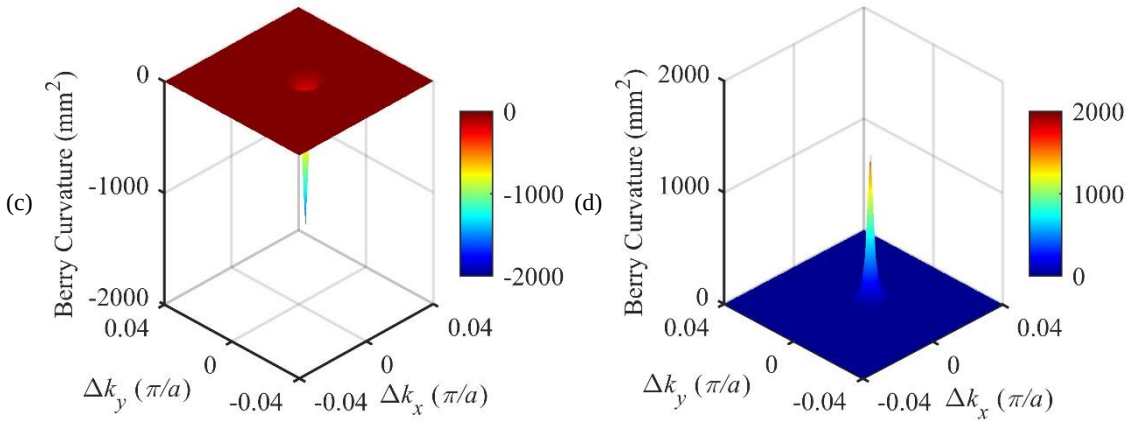

Figure 2.29: Distribution of the Berry curvature of the four constituent branches [from (a) to (d)] of the original double Dirac cone in the vicinity of the valley K. For each Dirac cone, the constituent branches have the opposite sign of the Berry curvature.

2.4.3.2 Pseudospin-protected edge states

To investigate the topologically pseudospin-protected edge state, we build a two-layers ribbon supercell as displayed in figure 2.30(a) constructed by juxtaposing ten unit cells of type-VII PPnC and ten unit cells of type-VIII PPnC vertically. According to the bulk-edge correspondence principle, the spin Chern number difference ±1 across the interface ensures the occurrence of the topologically protected edge states at DW1. Applying periodic conditions along the *x*-axis, the dispersion curves are numerically obtained and displayed in figure 2.30(b). Four pseudospin-locked edge states appear in the reopened band gap, namely a forward pseudospin down (↓) pair (cyan) and a backward pseudospin up (↑) pair (magenta). Figure 2.30(c) illustrates the eigenmodes of the magenta and cyan dotted line at the wave vector $k_x = 0.5\pi/a$. For each mode, the elastic deformation is localized around the domain wall. Especially, for the magenta branch, the displacement field is almost symmetric about the interface. In addition, it should be pointed out that when inverting the positions of type-VII and type-VIII PPnCs, the profiles of the topological edge states would keep the same, however, their associated pseudospin states are inverted.

In what follows, we are going to discuss the propagation of the pseudospin-protected edge states in the straight wave guide featuring a DW1 at the interface, built by placing type-VII and type-VIII PPnCs in the lower and upper regions. Two phase-matched *z*-polarized forces at frequency 1.782MHz are set in the middle of the domain wall to launch the K-polarized pseudospin-protected edge states. Figure 2.30(d) presents the out-of-plane displacement on the top surface of the plate. Both the left-going (pseudospin up) and right-going (pseudospin down) waves are generated, which is consistent with the two available edge states (pseudospin up state with negative group velocity and pseudospin down state with positive group velocity) at the valley K. The refracted patterns at the left and right zigzag outlets predicted by the EFCs

analysis are depicted in figure 2.30(e) and (f) respectively. Because S_0 (red) and SH_0 (green) Lamb modes in the plate at the same frequency have extremely small wave vectors, the edge state can only undergo refraction into A_0 Lamb modes (blue bold arrows). At the left zigzag outlet, it exists a negatively refracted beam (29.3°) and a positively refracted beam (78.2°). At the right zigzag termination, two refracted beams still exist and their refractive angles are inverted, *i.e.* 29.3° for the positively refracted one and 78.2° for the negatively refracted one. Both prediction is in very good agreement with the out-of-plane displacement fields at the left and right outlets.

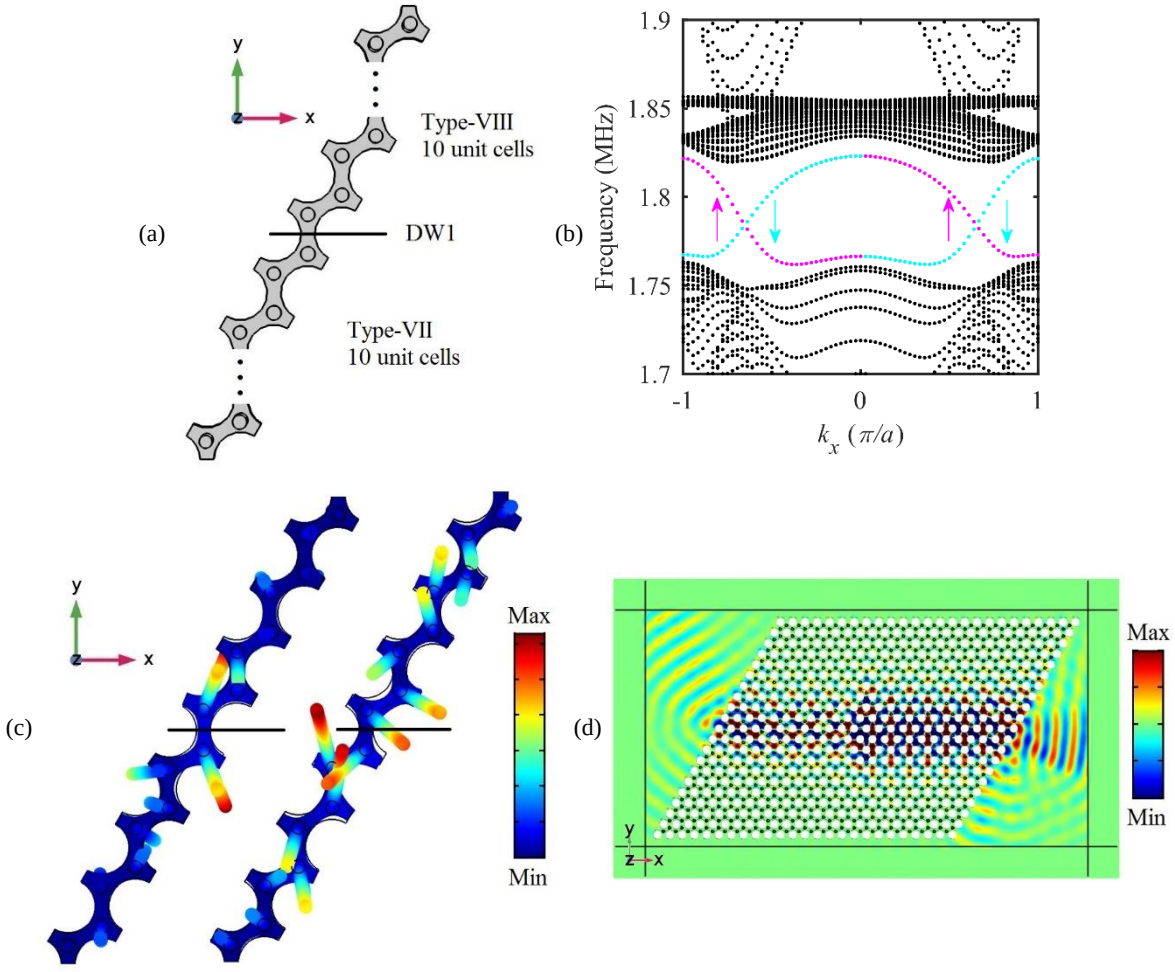

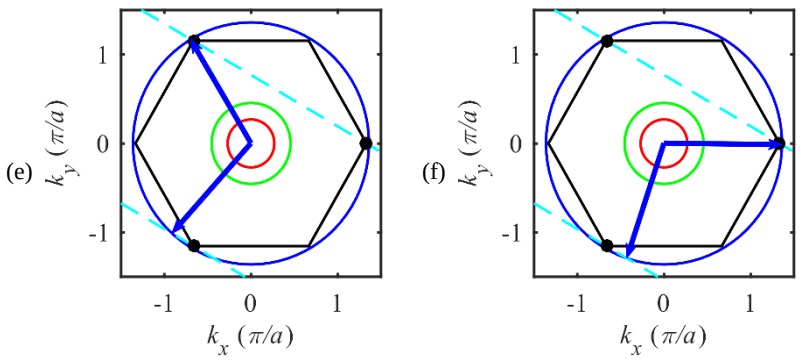

Figure 2.30: (a) Schematic of the proposed two-layers ribbon supercell constructed by juxtaposing ten unit cells of type-VIII PPnC and ten unit cells of type-VII PPnC vertically. (b) Dispersion curves of the ribbon supercell. (c) Eigenmodes of the magenta and cyan branches at the wave vector $k_x = 0.5\pi/a$. (d) Plot of the out-of-plane displacement on the top surface of the plate under the excitation of the K-polarized pseudospin-protected edge states at frequency 1.782MHz. EFCs analysis of the refracted patterns at the (e) left and (f) right zigzag terminations.

2.4.4 Pseudospin-valley combined edge states

As discussed in Sec. 2.4.2 and 2.4.3, depending on the perturbation imposed on the diameter or the height of the pillars, reserving or breaking the mirror-symmetry about the mid-plane of the plate, the proposed symmetric double-sided PPnC may emulate either QVHE or QSHE. Therefore, it provides a unique opportunity to investigate the pseudospin-valley combined edge state that utilizes both the pseudospin and valley degrees of freedom to control the wave propagation. Then, the propagation of the topologically protected edge states will depend on both the valley and pseudospin states unlike the valley-dependent propagation in Sec. 2.4.2 and the pseudospin-locked propagation in Sec. 2.4.3. To ensure the occurrence of the topological pseudospin-valley combined edge states, the two-layers ribbon supercell in figure 2.31(a) built by juxtaposing ten unit cells of type-VIII PPnC and ten unit cells of type-IX PPnC vertically is developed. Regarding the bottom layer, the height of the pillars was initially chosen to be $h_A = h_B = h_C = h_D = H = 152.5\mu m$. The diameter perturbation $\Delta d_V = -4\mu m$ (type-IX) is imposed on the ten unit cells to mimic QVHE. With regard to the top layer, it consists of ten unit cells with the height perturbation $\Delta h_S = -3\mu m$ (type-VIII) to simulate QSHE. The dispersion curves of the ribbon supercell are shown in figure 2.31(b). Remembering that the projection of the valleys K and K' on the zigzag domain wall is $k_x = -2\pi/3a$ and $k_x = 2\pi/3a$ respectively. At the valley K, the valley Chern number of type-IX PPnC is $C_V^{\uparrow\downarrow}(\mathrm{K}) = -1/2$ and the spin Chern number of type-VIII PPnC is $C_S^{\uparrow\downarrow}(\mathrm{K}) = \pm 1/2$. Therefore, the magenta dotted line denotes a backward pseudospin up edge state at DW2 due to the Chern numbers difference across the interface $C_S^{\uparrow}(\mathrm{K}) - C_V^{\uparrow}(\mathrm{K}) = -1$. Equally, at the valley K', the cyan dotted line represents a forward pseudospin down edge state occurring at the same domain wall. Therefore, the propagation of the edge states will depend on both the pseudospin and valley states. Besides, the grey dotted lines in the reopened band gap represent the

localized modes at the bottom end of the supercell. And the eigenmodes of the grey and cyan branches at the wave vector $k_x = 2\pi/3a$ are illustrated in figure 2.31(c) that unambiguously reveals the localized elastic energy.

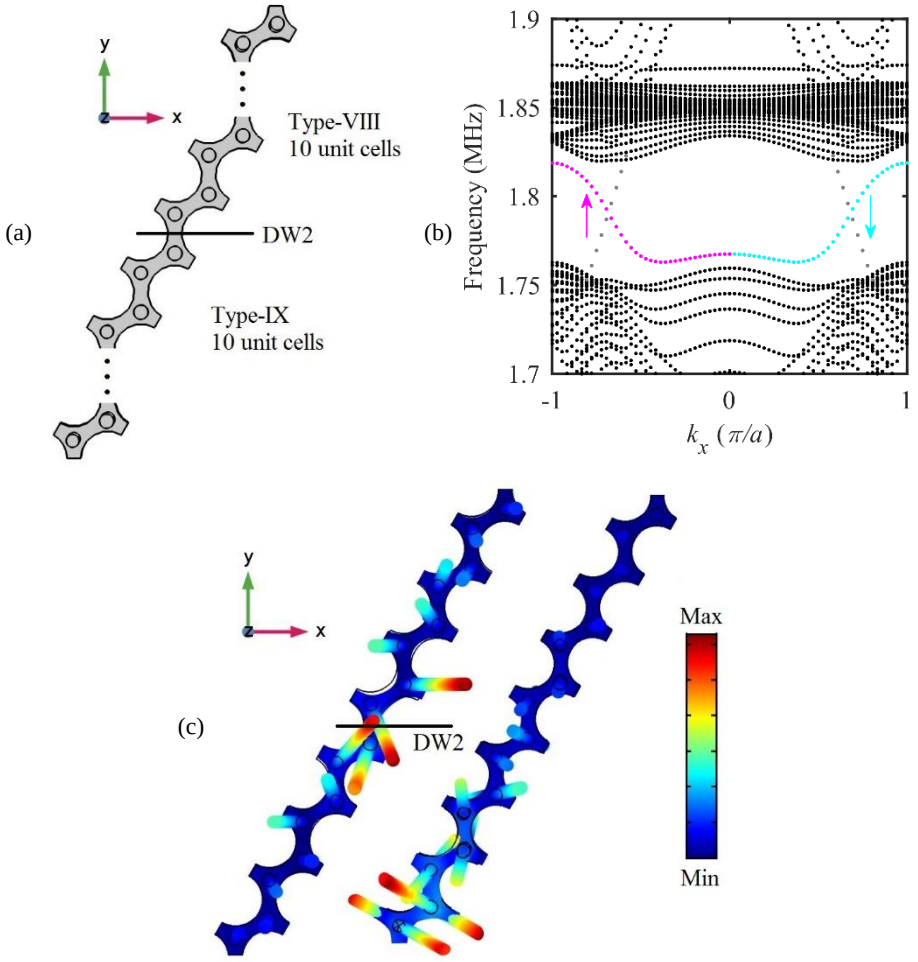

Figure 2.31: (a) Schematic of the proposed two-layers ribbon supercell constructed by juxtaposing ten unit cells of type-VIII PPnC and ten unit cells of type-IX PPnC vertically. (b) Dispersion curves of the ribbon supercell. (c) Eigenmodes of the grey and cyan branches at the wave vector $k_x = 2\pi/3a$.

Except that, we now consider another two-layers ribbon supercell constructed by juxtaposing PPnCs with the height perturbation Δh_S = 3μm (type-VII) and the diameter perturbation Δd_V = −4μm (type-IX) horizontally as shown in figure 2.32(a). Periodic condition along the *y*-axis is applied. The corresponding dispersion curves are displayed in figure 2.32(b). The eigenmodes of the cyan and grey branches at the wave vector $k_y = 2\pi/3a$ are illustrated in figure 2.32(c) which feature the localized resonant mode at the right end of the ribbon supercell and the topological edge state respectively. We mention that the projection of the valleys K and K' on this zigzag domain wall changes to $k_y = 2\pi/3a$ and $k_y = -2\pi/3a$ respectively. At the valley K', the valley Chern number of type-IX PPnC is $C_V^{\uparrow\downarrow}(\mathrm{K}') = 1/2$ and the spin Chern number of type-VII

PPnC is $C_S^{\uparrow\downarrow}(\mathrm{K}') = \mp 1/2$. The Chern numbers difference is $C_V^{\uparrow}(\mathrm{K}') - C_S^{\uparrow}(\mathrm{K}') = 1$ ensuring that a forward spin-up edge state (magenta) occurs at the valley K' at DW3. Analogously, a backward spin-down edge state (cyan) exists at the valley K.

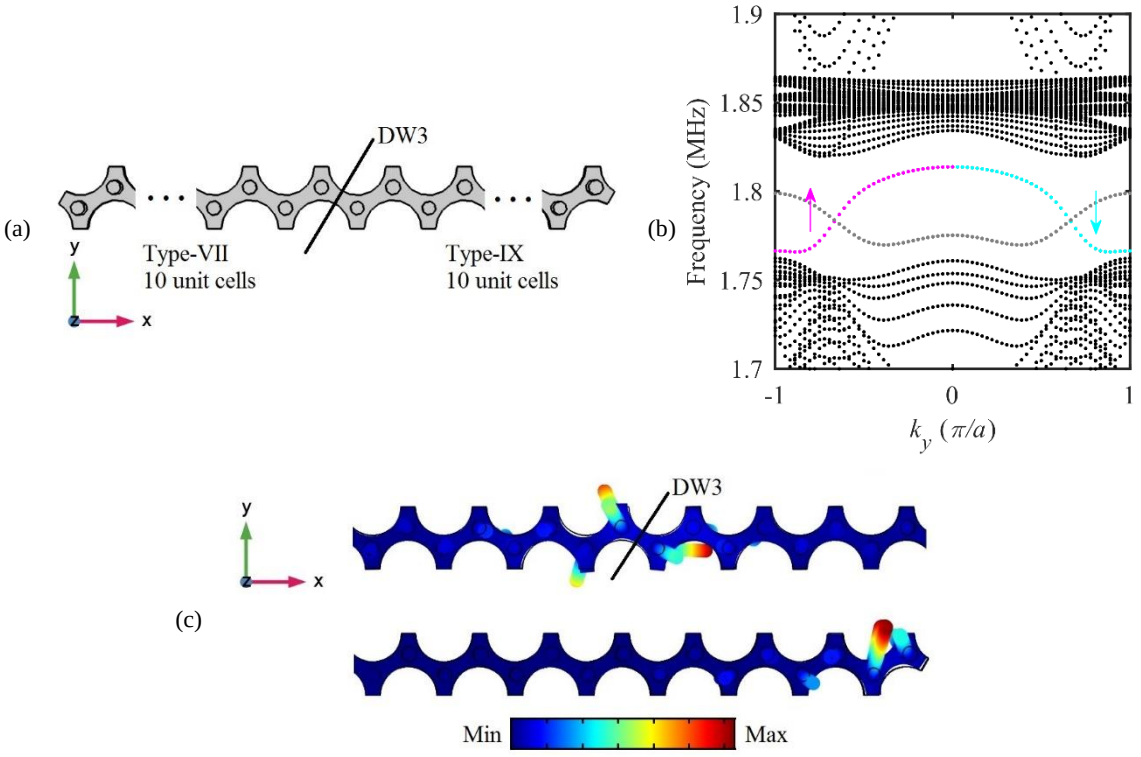

Figure 2.32: (a) Schematic of the proposed two-layers ribbon supercell constructed by juxtaposing ten unit cells of type-VII PPnC and ten unit cells of type-IX PPnC horizontally. (b) Dispersion curves of the ribbon supercell. (c) Eigenmodes of the cyan (top panel) and grey (bottom panel) branches at $k_x = 2\pi/3a$.

As demonstrated before, the propagation of the topological pseudospin down edge state at DW2 and DW3 depends on the specific valley. Therefore, the wave propagation path of the pseudospin down edge state at the intersection between DW2 and DW3 will be further decided by the associated valley. Figure 2.33(a) exhibits a T-shaped wave guide that assembles three different domain walls together, namely DW1, DW2 and DW3. As demonstrated in figure 2.30(b), at DW1, the pseudospin down edge state associated with either the valley K or K' can propagate, referred as $\Psi^{\downarrow}(\mathrm{K/K'})$. In comparison, at DW2, the pseudospin down edge state becomes propagative when it is locked to the valley K', referred as $\Phi^{\downarrow}(\mathrm{K}')$. Instead, it is associated with the valley K at DW3, denoted as $\Phi^{\downarrow}(\mathrm{K})$. Therefore, the valley based selection of the pseudospin down edge state should be expected at the junction. It is mentioned that the parameters for the perturbed PPnCs constructing the T-shaped wave guide is specifically designed to ensure the frequency of the topological edge state at the valleys occurring at the same frequency.

To confirm valley based path selection at the junction of three domain walls, the pseudospin protected edge states at frequency 1.782MHz associated with the valley K was selectively excited by two phase-matched sources placed in the middle of DW1. Figure 2.33(b) plots the out-of-plane displacement field on the top surface of the plate. At DW1, the pseudospin up edge state with negative group velocity is excited that propagates along the negative *x*-axis. And the pseudospin down edge state is simultaneously generated that possess positive group velocity, propagating along the positive *x*-axis. Upon encountering the junction, the pseudospin down edge state turns downwards and continues to propagate at DW3 owing to the conservation of the valley K. After that, by tuning the sources, we lock the wave vector to the valley K'. The distribution of the out-of-plane displacement is displayed in figure 2.33(c). The right-going pseudospin down edge state now only propagates at DW2 which is in good agreement with the theoretical prediction. Unambiguously, the proposed T-shaped wave guide allows for the valley based splitting of the pseudospin down edge states. Moreover, the pseudospin up edge states propagating at DW1 can also split by designing a similar T-shaped wave guide.

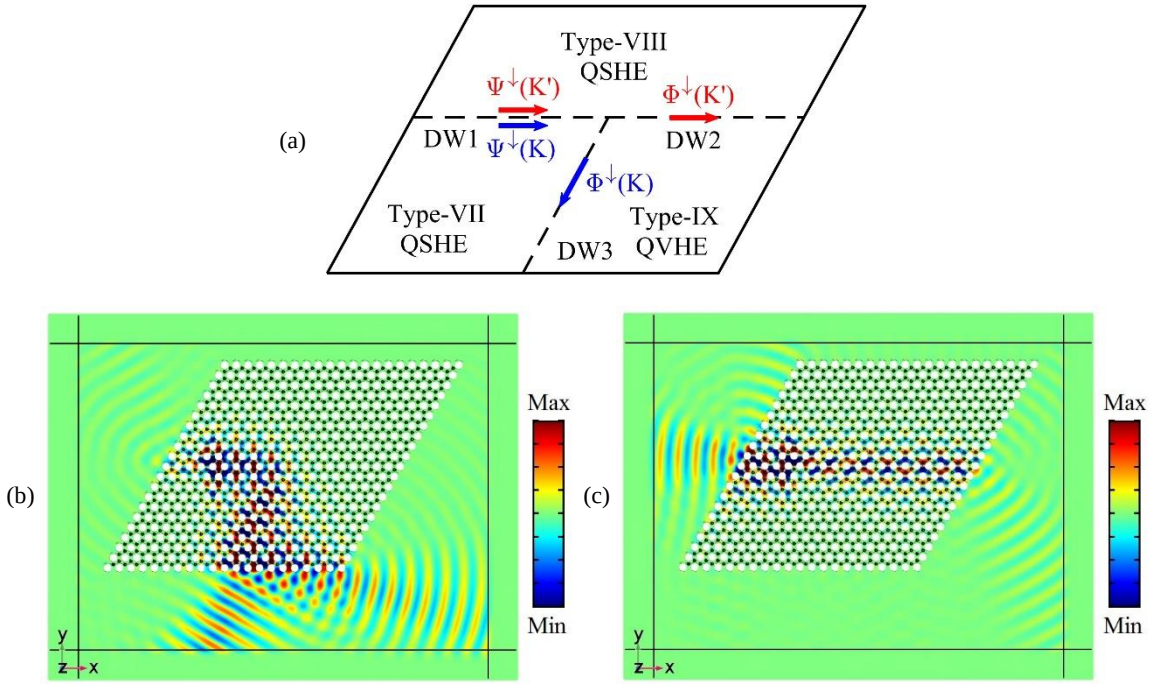

Figure 2.33: (a) Schematic of the T-shaped wave guide and the valley based splitting of the pseudospin down edge states. Plots of the out-of-plane displacement on the top surface of the plate while the pseudospin-protected edge states are locked to the valley (b) K and (c) K' respectively.

2.5 Conclusion

In this chapter, we have presented the realization of the topological transport of Lamb waves in both the asymmetric and symmetric double-sided PPnCs. Three different topological edge states, namely the valley-

protected, the pseudospin-protected and the pseudospin-valley combined, at different domain walls have been demonstrated. The interaction between the edge states and the zigzag or armchair terminations is analyzed in details, including the refracted and transmitted patterns.

In the asymmetric double-sided PPnC configuration, we extend our previous work about the double-negative branch in a square lattice pillared metamaterial. We have demonstrated that the mechanism also applies to the triangular lattice arrangement. Then, by transforming the triangular lattice to a honeycomb lattice design, the double-negative branch can be artificially folded to create a single Dirac cone. The constituent branches of the Dirac cone exhibit divergent polarization-dependent propagation behaviors along the primary directions of the BZ. When imposing the space-inversion symmetry breaking perturbation, the topological phase transition emulating QVHE is introduced. The Berry curvature around the valleys was numerically obtained. We show that the Berry curvature becomes strongly anisotropic when the wave vector gets far away from the valleys. Besides, we study the propagation of the topological edge states in different wave guides featuring two kinds of domain walls. At one domain wall, an incident A_0 (S_0) Lamb wave can propagate while the propagation of an incident SH_0 wave is forbidden. At the other domain wall, the contrary phenomena are observed. Except that, two large space-inversion symmetry breaking cases are taken into consideration. We show that in the case with gapless edge states the suppression of the inter-valley scattering at the zigzag termination can be achieved whereas weak inter-valley scattering occurs at the bending corners. In the other case with gapped edge states, strong reflection at both the zigzag termination and bending corners are observed which indicates that the topological protection is no longer guaranteed.

In the symmetric double-sided PPnC configuration, thanks to the mirror-symmetry about mid-plane of the plate, the symmetric and antisymmetric modes can be well decoupled which allows to investigate their topological features independently. By the judiciously choosing the height of the pillars, the Dirac cone can occur in the deep subwavelength scale or at the high frequency regime and even a double Dirac cone can be achieved. By perturbing the diameter or the height of the pillars while reserving the mirror-symmetry about the mid-plane of the plate, the topological phase transition emulating QVHE can be introduced. We show that the antisymmetric band structure subcomponent is more sensitive to the diameter perturbation and less sensitive to the height perturbation. Afterwards, we firstly investigate the topological edge states of the antisymmetric dispersion curves. It is found that the valley-polarized edge states can refracted into one or two A_0 Lamb waves at the zigzag outlet and one or three A_0 beams at the armchair termination depending on the height of the pillars. Secondly, we study the topological edge states of the symmetric dispersion curves. When occurring in the deep subwavelength scale, the valley-polarized edge state turns to be evanescent when propagating along the zigzag outlet and can be enhanced by the locally resonant modes. When arriving at the end of the domain wall, owing to the huge different between the wavelength and the

lattice constant, the topological edge state can behave as point sources whose interference results in the circular shape transmitted wave. After that, to ensure occurrence of the refraction at the zigzag termination, we reduce the height of the pillars that leads to a second Dirac cone occurring at the high frequency regime. The corresponding valley-polarized edge state can be refracted both positively and negatively. The negatively refracted beam only consists of SH_0 mode whereas the positively refracted beam is the combination of S_0 and SH_0 modes. Subsequently, we optimize the parameters of the unit cell to overlap the Dirac cones created respectively by the symmetric and antisymmetric modes to obtain a double Dirac cone. Then, by imposing perturbation on the height of the pillars, breaking the mirror-symmetry about the mid-plane of the plate, the topological phase transition emulating QSHE can be involved. And the propagation of the valley-polarized pseudospin-protected edge states is studied. Finally, we adopt both the pseudospin and valley degrees of freedom to investigate the pseudospin-valley combined edge state at the domain wall constructed by two topological distinct PPnCs each supporting QVHE and QSHE respectively. We evidence the valley-dependent feature of the pseudospin-valley combined edge states. Based on this property, we demonstrate the valley based splitting of the pseudospin down edge states in a T-shaped wave guide.

Chapter 3

3 Active control of transmission through a line of pillars

3.1 Introduction

As discussed in the previous two chapters, we provide two practical approaches in both the double-sided pillared metamaterials and the double-sided pillared phononic crystals to manipulate the propagation of Lamb waves in the plate. The first one can realize the negative refraction and acoustic cloaking in the subwavelength scale and polarization filtering which can be attributed to the occurrence of the doubly negative property contributed by the bending, the compressional and the torsional resonances of the pillars. The second one achieves the topologically protected transport in the wave guides built by two topologically distinct pillared systems. In both configurations the control of Lamb waves occurs in a very narrow frequency interval and the wave propagation behavior at a single frequency can be well designed, thus they are suitable for the predefined applications. However, regarding the quest for the time-dependent wave propagation modulation, these passive configurations are inefficient.

To overcome this difficulty, researchers resorted to the active metamaterials or phononic crystals. In these configurations, the external force originating from the electrical and/or mechanical devices is introduced which can receive the external information and make the timely response to modulate the propagating waves immediately. For example, Baz [47] proposed a one-dimensional active acoustic metamaterial with the programmable effective mass densities. It consists of an array of periodic fluid cavities separated by piezoelectric diaphragms that can be controlled to generate the constant mass densities over wide frequency intervals. By applying passive electric components, the effective mass densities can be orders of magnitudes lower or higher than the fluid medium. Acoustic cloaks can be implemented physically and objects treated with these active metamaterials can become acoustically invisible. Very recently, Baz [168] developed a disturbance rejection control strategy to achieve a closed-loop control of the effective mass density while rejecting the impact of the wave pressure disturbances. Popa *et al.* [48] described and experimentally demonstrated a systematic approach to design active acoustic metamaterials whose effective properties can be modulated independently in a wide range. The design consists of two transducers and an electronic circuit. The role of one transducer is to sense the pressure wave incident on the metamaterial. The other one is introduced to regenerate the acoustic response. These two transducers are connected by an electronic circuit which manages the electric signal produced by the first transducer and then drives the second one according

to the desired effective parameters. The active acoustic metamaterial can achieve not only the negative effective mass density, the non-unity bulk modulus and the negative refraction with tunable gain and absorption but also the non-reciprocal wave propagation [49,169]. Xiao *et al.* [170] proposed a membrane-type acoustic metamaterial which can be easily controlled by an external voltage. It employs a metal-coated central platelet and a rigid mesh electrode which is transparent to acoustic wave. It shows that DC voltage can modulate the resonant frequencies and tune the phase of the transmitted wave serving as an active phase modulator and AC voltage can provide an extra vibration that can act as an acoustic switch. Chen *et al.* [171] presented a tunable acoustic metamaterial, consisting of periodic membranes and side holes, featuring the doubly negative property. The tension and stiffness of the membranes are actively controlled by electromagnets that produces additional stresses, thus leading to the adjustable transmission and phase velocity. It is found that a tiny DC voltage can arise a significant shift of the double-negative pass band. Ning *et al.* [50] proposed an active system consisting of symmetric double Helmholtz cavities. The structure shows controllable effective bulk modulus, especially a negative value over a wide frequency interval, by changing external voltage with different piezoelectric diaphragm stiffness. The multilayered cloak can be achieved by implementing the active control on corresponding unit cells to exhibit desired distribution of the effective bulk modulus.

In the aforementioned configurations, the effective properties, including the negative effective mass density, the negative effective bulk modulus, the doubly negative property and the transmission can be effectively controlled by involving the external fields. Inspired by these, we attempt to introduce external sources into the pillared resonators to actively control the transmission of incident Lamb waves propagating through the pillared metamaterials. As mentioned before, the pillared resonator features the bending, the compressional and the torsional resonances. All these resonant frequencies can be independently tuned through a proper choice of the height and/or the diameter. Moreover, in some specific situation, the bending and the compressional modes can superimpose at the same frequency.

By analyzing the scattered Lamb waves by a line of pillars at resonance in Ref. [82], it has been shown that the transmitted wave in the far field can be considered as the superposition of the incident Lamb wave and the reemitted Lamb wave generated by the line of resonators. What's more, the transmission spectrum is quietly different depending on whether the bending resonance and the compressional resonance occur at the same frequency or not. When these two modes occur at different frequencies, two transmission dips would be formed, and even go to zero. This can be ascribed to the destructive interferences between the incident Lamb wave and the π-phase-shift reemitted Lamb wave, both having comparable amplitudes. In comparison, the amplitude of the reemitted Lamb wave increases significantly when the bending mode and the compressional mode occur at the same frequency. In that case, even though there is still a π-phase-shift

between the incident and reemitted Lamb waves, transmission of a substantial part of the elastic energy becomes possible.

In this chapter, we go a step further. We used numerical simulations to investigate the control over the transmission of an incident A_0 Lamb wave propagating through a line of pillars close to the resonance, with an external force applied on the top. The chapter is organized as follows. In Sec. 3.2, we identify the eigenmodes of the line of pillars by calculating the transmission spectrum and discuss the coupling between the neighboring pillars by comparing to the pillared metamaterials. After that, the properties of the reemitted Lamb wave generated by the line of pillars around the resonances are studied in Sec. 3.3. Two different lines of pillars with the bending resonance and the compressional resonance separated and superimposed are taken into consideration. Further, in Sec. 3.4, by employing external force applied on the top ends of the pillar resonators, we study the evolution of the transmission coefficients against the magnitude and phase of the external source. Both the traction force parallel to the top ends and pressure normal to the top ends are discussed. Their efficiency in modulating the transmission coefficient is evaluated. Finally, it ends with the general conclusion in Sec. 3.5.

3.2 Eigenmodes of a line of pillars

In this section, we investigate the transmission spectrum of an incident A_0 Lamb wave propagating through a line of pillars. In this way, the locally resonant modes of the line of pillars can be recognized owing to the dips occurring in the transmission spectrum. The finite element model we used is described in figure 3.1(a). The diameter and the height of the pillar were set to be d = 50μm and h = 245μm respectively. The line of pillars is infinite along the x-axis and the repeat distance a = 200μm is modeled by applying periodic conditions along the x-axis. The thickness of the plate was set to be e = 145μm. Perfectly match layers (PMLs) are arranged at two ends in order to eliminate the waves reflected by the boundaries. Both the pillars and the plate are assumed to be made of silicon. The elastic constants are C_{11} = 166GPa, C_{12} = 64GPa and C_{44} = 79.6GPa and the mass density is $\rho = 2330 kg/m^3$.

Subsequently, an incident A_0 Lamb wave was excited 1000μm away from the left side of the line of pillars by applying z-axis polarized pressure on the plate. The out-of-plane displacement is recorded at a distance of 500μm downstream the line of pillars. Then, the transmission spectrum can be computed by normalizing the out-of-plane displacement to the one in a reference model without pillars and displayed in figure 3.1(b). It can be seen that three sharp transmission dips appear. Each of them relates to a specific resonant mode that can be unambiguously identified owing to the associated displacement field depicted in figure 3.1(d). Obviously, the first one at frequency 0.8MHz is the first-order bending resonance, hereafter referred as B1. The second one corresponds to the second-order bending resonance (B2) at frequency 4.66MHz. And the

third one represents the first-order compressional resonance at frequency 7.24MHz denoted as C1. In comparison, the transmission coefficient at the compressional resonance C1 is much lower than the ones at the bending resonances B1 and B2. It might be ascribed to the perfect coupling between the compressional mode and the incident A_0 Lamb wave that features the out-of-plane polarization. It can also be explained from another point of view that will be discussed in the following. It should also be noticed that the transmission coefficient at the compressional resonance C1 is very small, but it is nonzero.

Compared to the pillared metamaterials or the phononic crystals discussed in the previous two chapters, the geometrical difference lies in that the line of pillars investigated in this chapter contains only one unit cell along the *y*-axis. Therefore, the coupling effect between the neighboring pillars along the *y*-axis no longer exists. Figure 3.1(d) shows the band structure of a square lattice pillared metamaterial built by the same pillar displayed in figure 3.1(a). The lattice constant is set to be 200μm. As discussed before, the flat dispersion curves denote the resonances of the pillars. For the bending resonances B1 and B2, they occur at frequencies 0.8MHz and 4.6MHz respectively that are in very good agreement with the first and second transmission dips depicted in figure 3.1(b). Obviously, for the bending resonances, the influence of the coupling between the neighboring pillars on the resonant frequencies can be neglected which might be related to the huge difference between the wavelengths of S_0 Lamb wave (9735μm at frequency 0.8MHz and 1690μm at frequency 4.6MHz) propagating in the plate at the same frequency and the lattice constant. For the compressional resonance C1, it occurs at frequency 6.91MHz that has a 4.56% discrepancy from the frequency at the third transmission dip which suggest that the coupling between the neighboring pillars may affect the eigenfrequency. It should be mentioned here that the wavelength of A_0 Lamb wave (468μm) propagating in the plate at the same frequency is the same order of magnitude as the lattice constant.

(a)

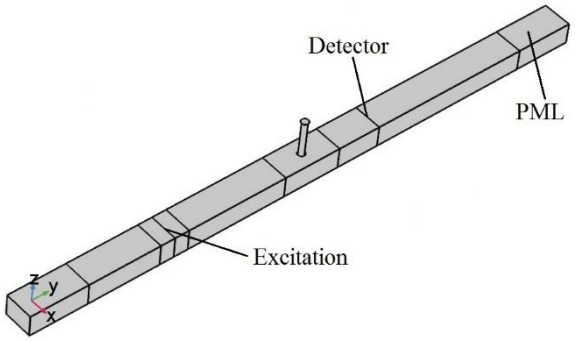

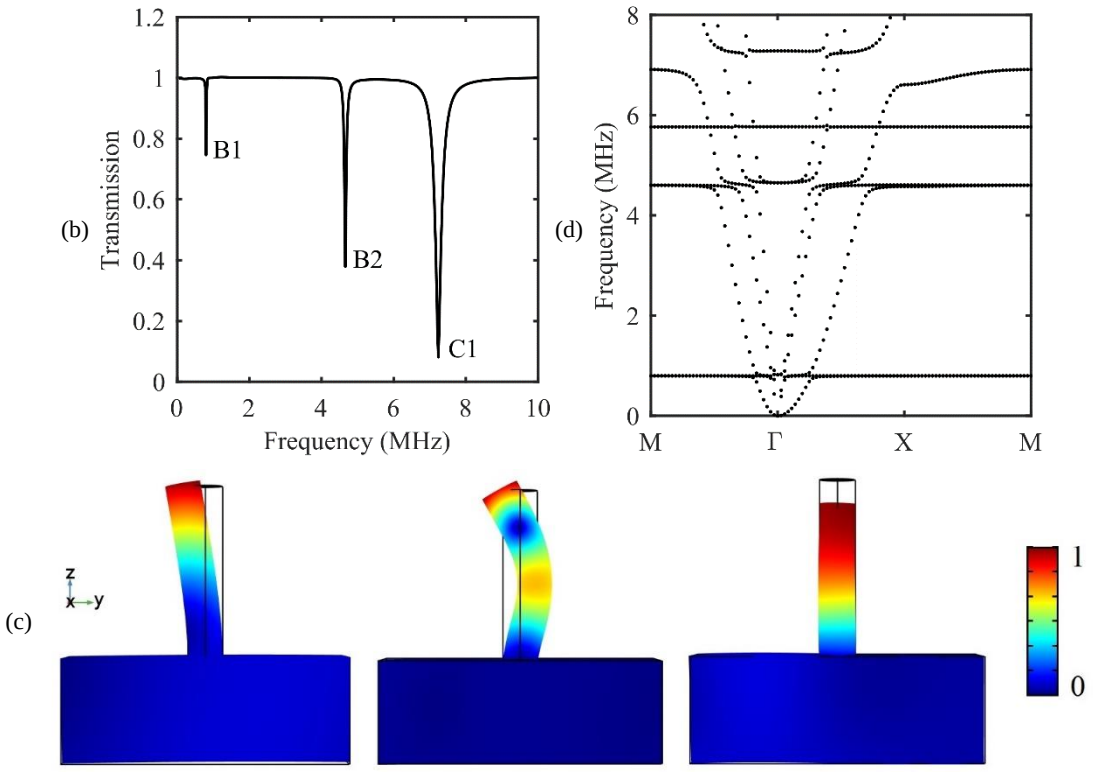

Figure 3.1: (a) Proposed finite element model and (b) transmission spectrum of an incident A_0 Lamb wave propagating through the line of pillars. (c) Normalized displacement fields of the line of pillars at the three transmission dips. (d) Band structure of a square lattice pillared metamaterial built by the same pillar shown in (a) with lattice constant set to be 200μm.

As mentioned in Ref. [82], the frequencies of both bending modes strongly depend on the diameter of the pillar but it is less sensitive to its height. Especially, the eigenfrequency of the bending resonance B2 increases much quickly than the one of the bending resonance B1 while the diameter of the pillar grows. As for the compressional resonance C1, the height of the pillar has a more significant impact than the diameter. Therefore, it can be speculated that the bending resonance B2 and the compressional resonance C1 can occur at the same frequency by properly selecting the height or the diameter of the pillar. Figure 3.2(a) depicts the evolution of the transmission spectra of an incident A_0 Lamb wave against the diameter of the line of pillars. Three different configurations are taken into consideration, namely 80μm, 100μm and 120μm represented by the black, the red and the blue solid lines respectively. It can be seen that the transmission dips generated by the bending resonance B1 shifts slightly and the transmission dips corresponding to the bending resonance B2 and the compressional resonance C1 merge gradually as the diameter of the pillars increases. By optimizing the parameters, it is found that the frequencies of the bending resonance B2 and the compressional resonance C1 overlap at frequency 7.57MHz when the diameter is set to be 112μm. The corresponding transmission spectrum is displayed in figure 3.2(b). The transmission coefficient at the

frequency B2/C1 is much larger than the ones in figure 3.1(b) where the bending resonance B2 and the compressional resonance C1 are separated.

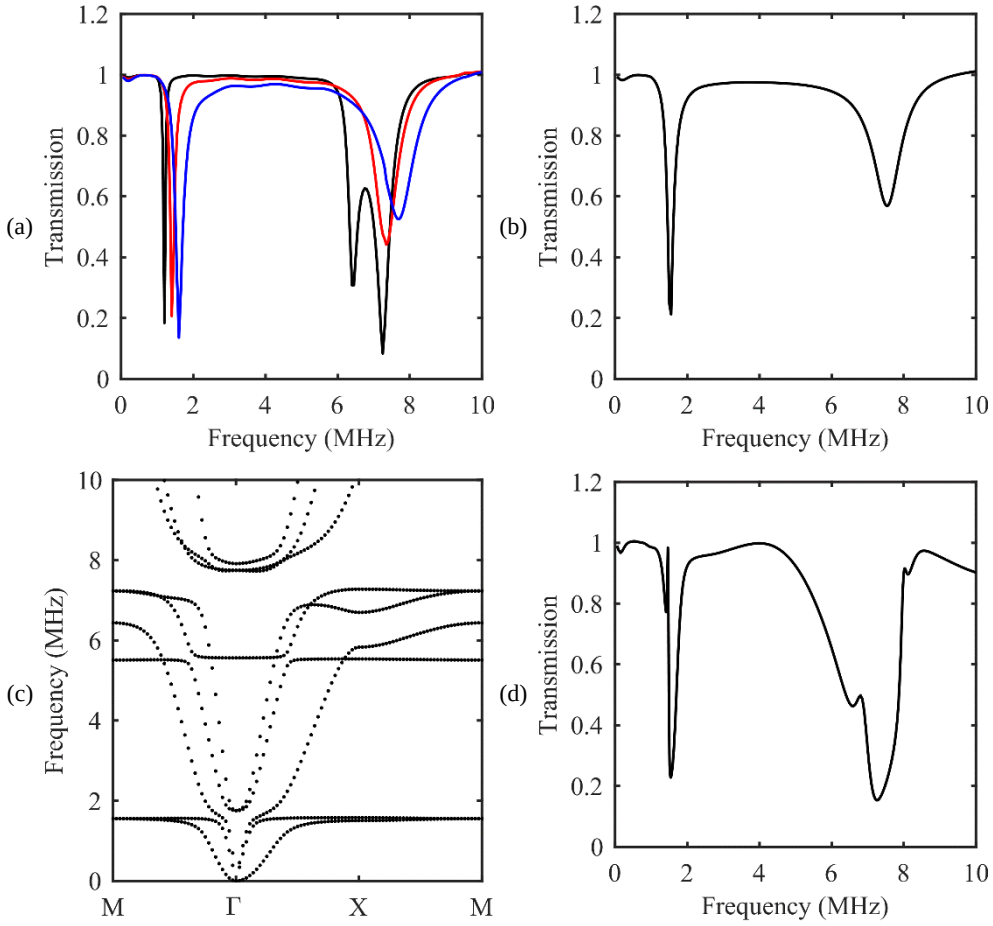

Figure 3.2: (a) Evolution of the transmission spectra of an incident A_0 Lamb wave against the diameter of the line of pillars. The black, the red and the blue solid lines represent the spectrum for the line of pillars with the diameter set to be 80μm, 100μm and 120μm respectively. (b) Transmission spectrum of an incident A_0 Lamb wave with the diameter of the line of pillars set to be 112μm. (c) Band structure of a square lattice pillared metamaterial built by the same pillars adopted in (b). (d) Transmission spectrum of an incident A_0 Lamb wave propagating through the three lines of pillars.

Figure 3.2(c) shows the band structure of a square lattice pillared metamaterial constructed by the corresponding pillars. The bending resonance B1 occurs at frequency 1.56MHz which is in very good agreement with the frequency at the first transmission dip. However, the bending resonance B2 and the compressional resonance C1 occur at frequencies 7.24MHz and 6.44MHz that has 4.39% and 14.97% discrepancies from the frequency at the second transmission dip. The coupling of the neighboring pillars has a significant influence on the resonant frequencies, especially on the compressional resonance C1. Figure 3.2(d) shows the transmission spectrum of an incident A_0 Lamb wave propagating through the three line of pillars (three unit cells along the *y*-axis). Thus, the coupling of the neighboring pillars along the *y*-

axis should be taken into consideration. Two separated transmission dips occur at frequencies 6.6MHz and 7.27MHz respectively which are in very good agreement with the resonant frequencies deduced from the band structure. Therefore, the line of pillars investigated in this chapter is quite different from the pillared metamaterials or the phononic crystals, because the coupling effect from the neighboring pillars are not involved that can significantly influence the resonant frequencies, especially when the wavelength of Lamb wave propagating in the plate is the same order of magnitude as the lattice constant.

3.3 Lamb waves reemitted by a line of pillars

As demonstrated in Ref. [82], the pillars can reemit Lamb waves when it is excited into vibration by an incident Lamb wave. In the linear regime where only small amplitude is involved, the superposition principle applies and thus, the displacement field downstream the line of pillars can be regarded as the sum of the incident Lamb wave and the remitted Lamb wave. Thus, subtracting the former from the transmitted wave allows to thoroughly analyze the features of the latter. In figure 3.3(a), we show the evolution against the frequency, of the complex amplitude of the reemitted Lamb wave, normalized to the incident Lamb wave. The square markers are introduced solely to help to visualize the tendency and the corresponding frequencies are shown in the adjacent labels. At the lower (*i.e.* 2.5MHz) or the higher (*i.e.* 10MHz) frequencies regimes that are far away from the resonances, both the real and imaginary parts tend to zero which means that almost no reemitted Lamb wave is generated by the line of pillars. It can be well understood by considering the huge difference between the diameter of the pillars and the wavelength of the Lamb wave propagating in the plate. The diffraction would occur around the line of pillars and the total transmission can be achieved. In contrast, the complex amplitude displays drastic changes in the vicinity of the resonances and rotates clockwise as the frequency increases. Moreover, at the bending resonance B2 and the compressional resonance C1, the imaginary parts become zero and the real parts turn negative, as shown in figure 3.3(b) that plots the top view (see from the positive *z*-axis) of figure 3.3(a), which means that the reemitted Lamb wave is out-of-phase with the incident Lamb wave. The destructive interference occurs that finally results in the transmission dips. In addition, the complex amplitude around the compressional resonance C1 changes gradually comparing to the one around the bending mode B2 that is consistent with the broader profile of the dip. The magnitude of the reemitted Lamb wave around the compressional resonance C1 is much larger (but still smaller than the one of the incident Lamb wave) that can further explain the smaller transmission coefficient.

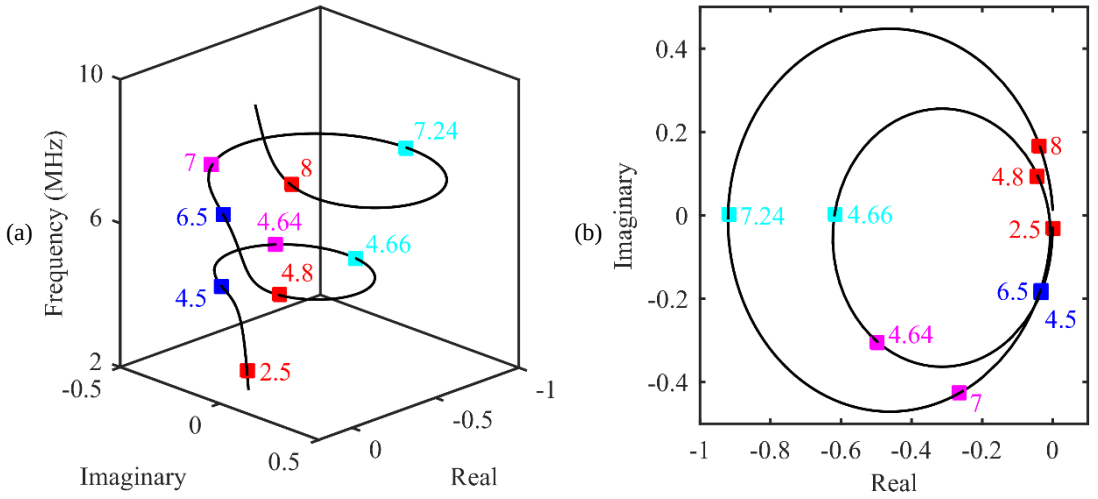

Figure 3.3: (a) Evolution of the complex amplitude of the reemitted Lamb wave against the frequency. (b) Top view (see form the positive *z*-axis) of the curve displayed in (a). The bending resonance B2 and the compressional resonance C1 are separated.

We have demonstrated in the previous subsection that the bending resonance B2 and the compressional resonance C1 can occur at the same frequency when the diameter is set to be 112μm. Reproducing the same procedure, we can analyze the reemitted Lamb wave in this situation. The evolution against the frequency of the complex amplitude of the reemitted Lamb wave is displayed in figure 3.4(a) and (b). The profiles are similar to the ones shown in figure 3.3(a) and (b) and the winding of the complex amplitude around the resonance can be observed. The difference between them lies in the magnitude of the reemitted Lamb wave which is almost 1.5 times the incident Lamb wave. It indicates that the incident Lamb wave is totally cancelled out by the reemitted Lamb wave and the remain part of the reemitted Lamb waves contributes to the transmitted field.

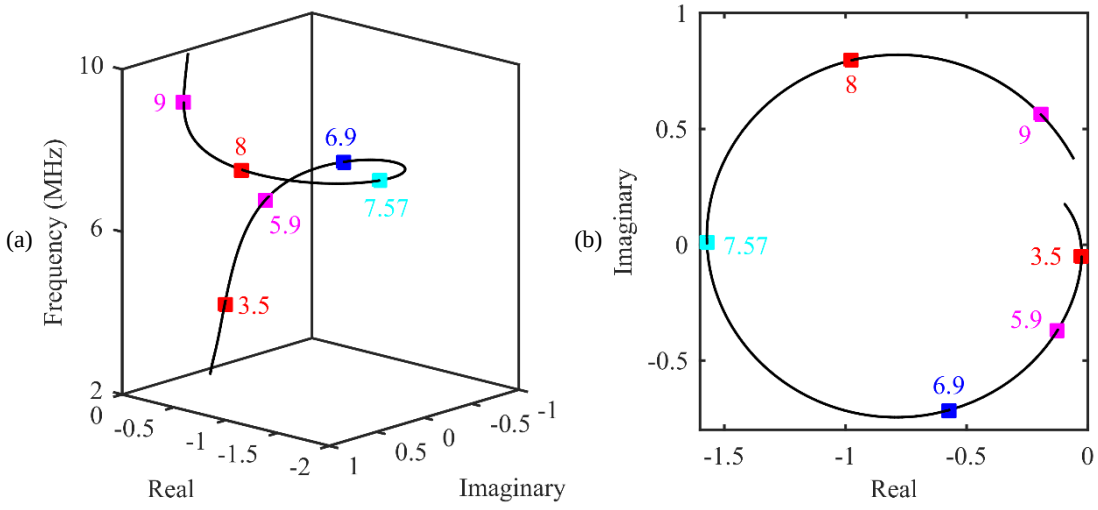

Figure 3.4: (a) Evolution of the complex amplitude of the reemitted Lamb wave against the frequency. (b) Top view (see from the positive *z*-axis) of the curve displayed in (a). The bending resonance B2 and the compressional resonance C1 are superimposed.

3.4 Control of the transmission through a line of pillars by introducing external sources

As discussed in Sec. 3.3, the superposition of the incident and reemitted Lamb wave generated by the vibration of the line of pillars finally results in the dips in the transmission spectrum. This interferential mechanism suggests to introduce external sources applied on the pillars as shown in figure 3.5, to enhance or suppress their vibration in order to handle the reemitted Lamb wave. Then, the transmission coefficient can be further modulated. In figure 3.5, the internal source allows to generate the incident Lamb wave with both phase and amplitude kept constant. The corresponding amplitude of the transmitted wave at the detector is denoted as $A_{transIn}$. On the other hand, if only the external source is involved, the amplitude of the transmitted wave is represented by $A_{transEx}$. The transmitted wave under the excitation of both these sources is simply expressed as $A_{transTotal} = A_{transIn} + A_{transEx}$.

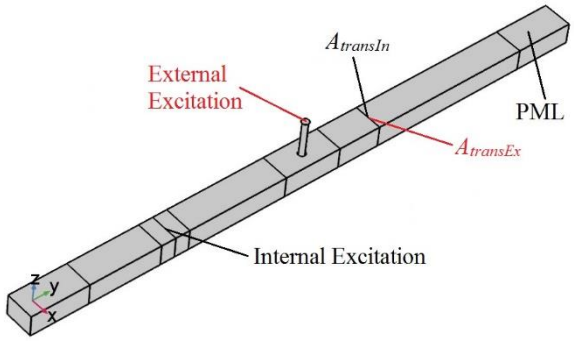

Figure 3.5: Schematic of the transmission control by introducing external sources applied on the line of pillars.

As much as the discussion in Secs. 3.2 and 3.3, two different systems will be studied. Firstly, the line of pillars with the bending resonance B2 and the compressional resonance C1 occurring at different frequencies and secondly, the line of pillars with both these resonances being superimposed.

3.4.1 Line of pillars with separated modes

To ensure a good coupling with the bending resonance B2, we firstly consider a traction force imposed on the top ends of the line of pillars, parallel to the y-axis, acting as the external source. The excitation frequency shifts slightly from the resonant frequency to avoid singularity and is chosen to be 4.6MHz. Two independent parameters of the external traction force can be controlled, namely, the magnitude and the phase difference with respect to the internal excitation. Figure 3.6 shows the transmission coefficient map against the phase difference and the magnitude of the external source. The color bar represents the transmission coefficient ranging from 0 to 1. In the calculation, the magnitude is assumed to be positive ranging from 0

to 1MPa; a negative magnitude will solely introduce an additional π-phase shift to the phase difference (varying from 0 to 2π). Unambiguously, the total transmission (transmission coefficient is equal to 1) can be easily achieved when matched magnitude and phase difference are applied. A large domain of solutions can be found from figure 3.6. However, to achieve zero transmission, there is only one possible scheme (inside the blue region). Moreover, when the phase difference is in between π and 1.5π, the transmission coefficient firstly decreases and then increases whereas the magnitude grows continuously.

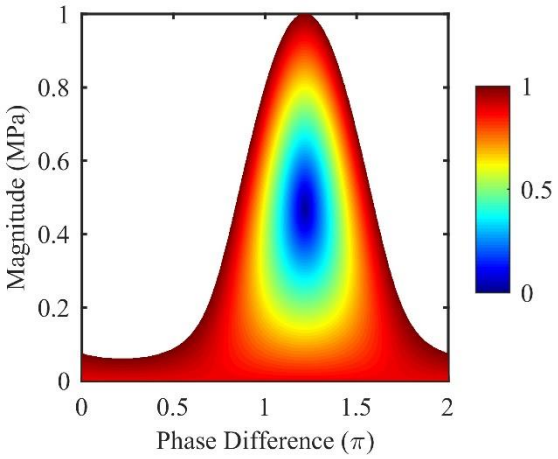

Figure 3.6: Transmission coefficient map against the phase difference and the magnitude of the external traction force. The color bar represents the transmission coefficient ranging from 0 to 1.

To better interpret the transmission coefficient map, the magnitude of the external traction force assumed to be 0.1MPa is considered. The transmission coefficient against the phase difference is depicted in figure 3.7(a). At point A (with the phase difference 0.22π), the transmission coefficient reaches the maximum value whereas it becomes minimum at point B (with phase difference 1.22π). In figure 3.7(b), we show the relative phase between the transmitted amplitude $A_{transEx}$ and $A_{transIn}$ given by the parameter $\beta = angle\left(A_{transEx} / A_{transIn}\right)$. At point A (0.22π), these two amplitudes are in-phase, whereas the out-of-phase relationship can be observed at point B (1.22π). Therefore, it is the constructive interference between the internal and external excitations that contributes to the maximum transmission coefficient at point A and the destructive interference that leads to the transmission dip at point B. It should also be mentioned that when the in-phase or out-of-phase relationship between the transmitted amplitudes $A_{transEx}$ and $A_{transIn}$ is constant, the transmission coefficient is proportional to the magnitude of the external traction force. Therefore, it can be continuously tuned in between 0 and 1.

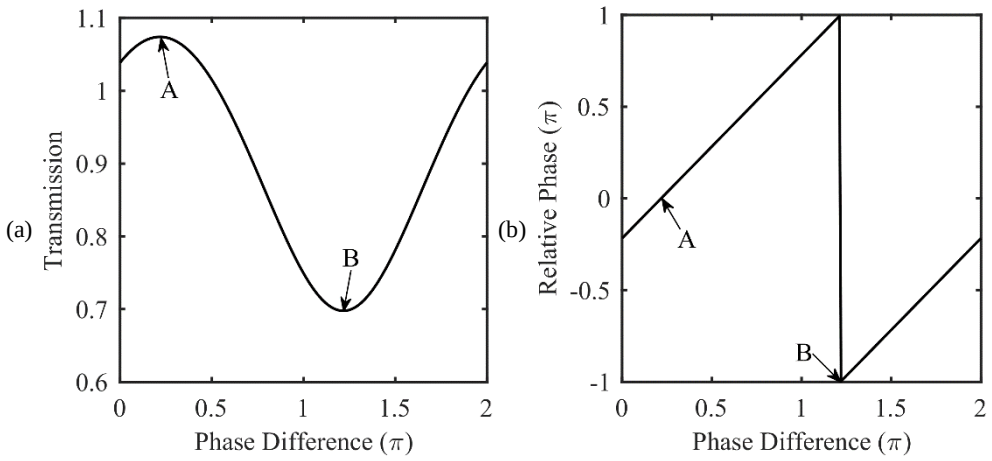

Figure 3.7: (a) Transmission coefficient against the phase difference of the external traction force when the magnitude is assumed to be 0.1MPa. (b) Relative phase between the transmitted amplitude $A_{transEx}$ and $A_{transIn}$.

Subsequently, the evolution between the transmission coefficient and the magnitude is investigated and displayed in figure 3.8(a). The phase difference is fixed at 0.22π where the transmitted amplitudes $A_{transEx}$ and $A_{transIn}$ are in-phase. As expected, the transmission coefficient is proportional to the magnitude of the external traction force. When the magnitude is set to be −0.47MPa (point C), the zero transmission can be achieved. The negative sign means an additional π-phase shift to the phase difference. That is 1.22π in this case. When the magnitude turns to be either 0.06MPa (point D) or −1MPa (point E), the transmission coefficient is equal to 1. To figure out the difference in these two cases, the relative phase between the transmitted amplitude $A_{transTotal}$ and $A_{transIn}$ is computed and shown in figure 3.8(b). At point D, the transmitted amplitude $A_{transTotal}$ is in-phase with $A_{transIn}$. This suggests that both the internal and external excitations contribute constructively to the transmitted field. While at point E, the transmitted amplitude $A_{transTotal}$ is out-of-phase with $A_{transIn}$. It is always maintained when the magnitude lies in between points C and E. Owing to the destructive interference, the transmitted wave from the internal source will be totally cancelled out. The final transmitted wave actually origins from the external source and the transmission coefficient increases with increasing magnitude.

Regarding the transmission coefficient map shown in figure 3.6, very small injected energy is needed to achieve the total transmission when the phase difference is set around 0.22π owing to the constructive interference between the transmitted waves generated by the internal and external sources. The minimum value is obtained when the phase difference is 0.22π and the magnitude is 0.66MPa. When the phase difference is set around 1.22π, the destructive interference happens. Thus, the transmission coefficient firstly decreases as the magnitude increases. When the transmitted wave from the internal source is totally cancelled out, the transmission coefficient increases as the magnitude continues to grow. The zero transmission can be obtained with the phase difference 1.22π and the magnitude 0.47MPa.

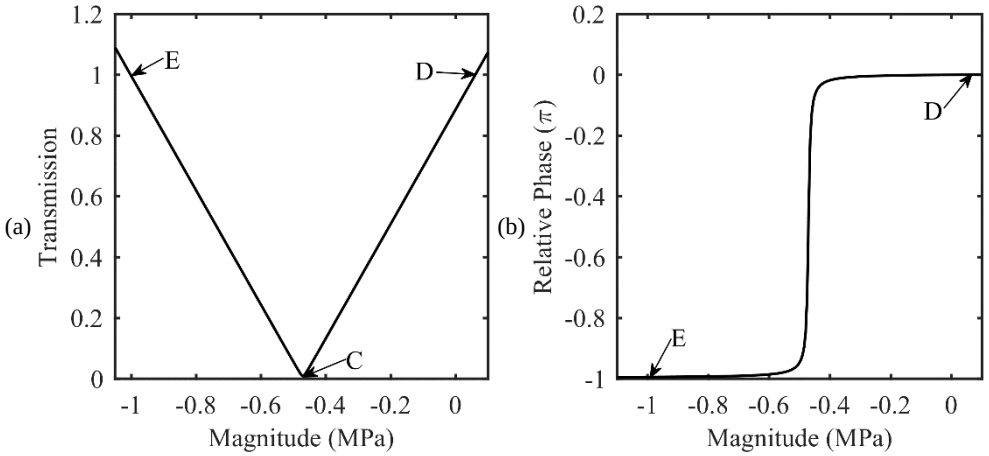

Figure 3.8: (a) Transmission coefficient against the magnitude of the external traction force when the phase difference is fixed at 0.22π. (b) Relative phase between the transmitted amplitude $A_{transTotal}$ and $A_{transIn}$.

Except the external traction force, we can also impose an external pressure on the top of the pillars. The evolution of the transmission coefficient against the phase difference if assuming a magnitude of 3MPa, is shown in figure 3.9(a). It reaches the maximum and minimum values with the phase difference set to be 0.57π and 1.57π respectively. These phases correspond to the transmitted amplitudes $A_{transEx}$ and $A_{transIn}$ in-phase and out-of-phase. Figure 3.9(b) depicts the transmission coefficient against the magnitude when the phase difference is chosen to be 0.57π. The total transmission can be achieved with the magnitude 1.1MPa or −18.8MPa and the zero transmission can be obtained with magnitude −8.8MPa.

In summary, either the external traction force or the pressure can be employed to modulate the transmission coefficient when the excitation frequency is close to the bending resonance B2. However, the external pressure needs higher energy level to achieve the total and zero transmission in comparison with the external traction force, because the coupling with the bending vibration of the pillars is less efficient.

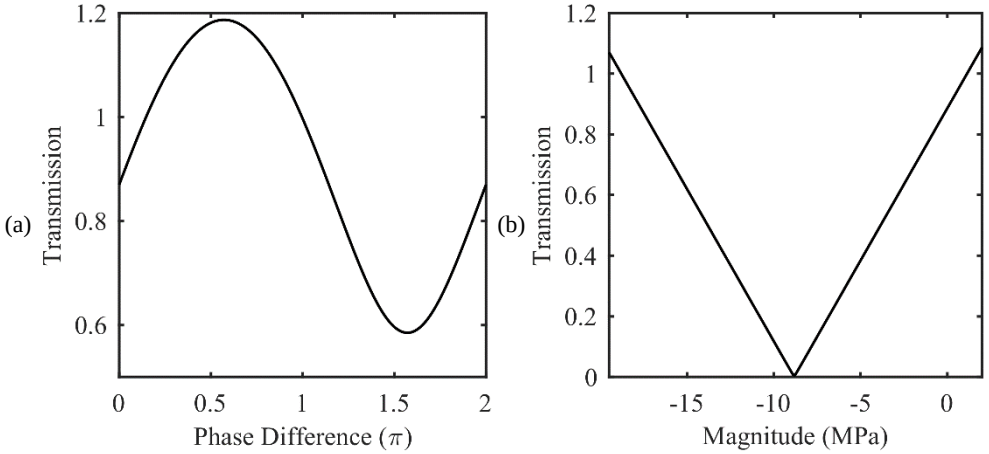

Figure 3.9: (a) Transmission coefficient against the phase difference of the external pressure when the magnitude is assumed to be 3MPa. (b) Transmission coefficient against the magnitude of the external pressure when the phase difference is chosen to be 0.57π.

Concerning the transmission control around the compressional resonance C1, an external pressure applied on the top of the pillars is firstly introduced which can easily couple into their compressional vibration. The excitation frequency is selected to be 7.2MPa. The transmission coefficient map versus the phase difference and the magnitude of the external pressure is displayed in figure 3.10 within which the phase difference varies from 0 to 2π and the magnitude ranges from 0 to 0.7MPa. It can be seen that the transmission coefficient can be continuously tuned. Figure 3.11(a) displays the transmission coefficient versus the phase difference when the magnitude is assume to be 0.5MPa. The minimum and maximum transmission occur at 0.72π and 1.72π respectively. Figure 3.11(b) depicts the relative phase between the transmitted amplitude $A_{transEx}$ and $A_{transIn}$. It is out-of-phase at 0.72π and becomes in-phase at 1.72π.

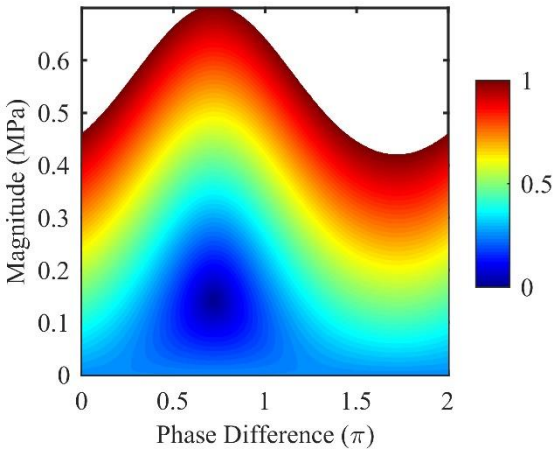

Figure 3.10: Transmission coefficient map against the phase difference and the magnitude of the external pressure. The color bar represents the transmission coefficient ranging from 0 to 1.

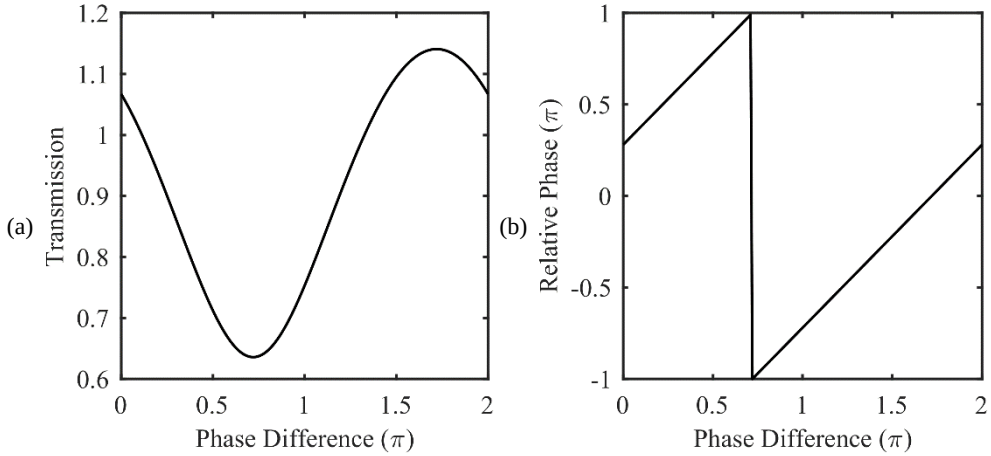

Figure 3.11: (a) Transmission coefficient against the phase difference of the external pressure when the magnitude is assumed to be 0.5MPa. (b) Relative phase between the transmitted amplitude $A_{transEx}$ and $A_{transIn}$.

Subsequently, the influence of the magnitude of the external pressure on the transmission coefficient is studied. The phase difference is chosen to be 1.72π where, according to figure 3.11(a), the maximum transmission is obtained. The evolution of the transmission coefficient versus the magnitude of the external pressure is displayed in figure 3.12(a). The total transmission can be achieved when the magnitude is −0.7MPa. The transmission coefficient decreases to 0 when the magnitude increases to −0.14MPa. Afterwards, it increases as the magnitude continues to grow and reaches 1 again at 0.42MPa. Figure 3.12(b) displays the relative phase between the transmitted amplitude $A_{transTotal}$ and $A_{transIn}$. When the magnitude is less than −0.14MPa, the contribution to the transmitted wave of the external source becomes dominant. When the magnitude is greater than 0, both the internal and external sources contribute to the transmitted field. When the magnitude is in between −0.14MPa and 0, the transmitted wave form the internal source is partly cancelled out and the rest part together with the one from the external source forms the transmitted field.

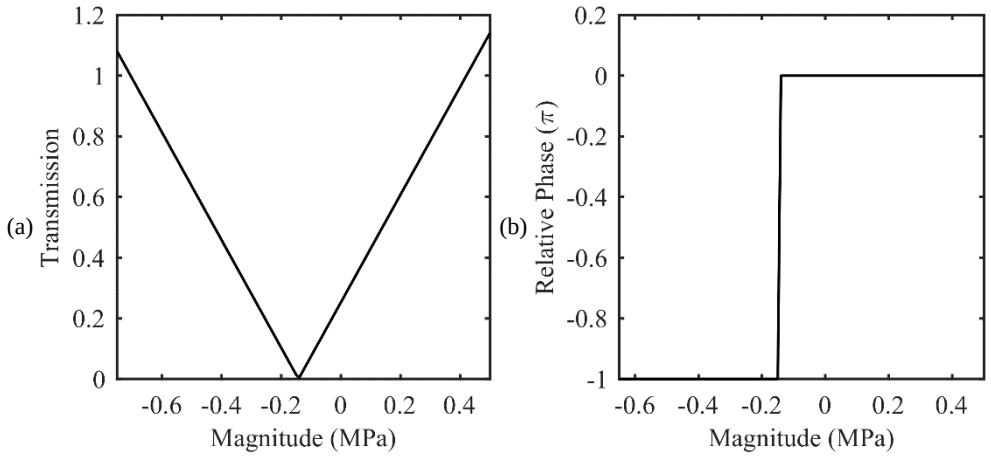

Figure 3.12: (a) Transmission spectrum against the magnitude of the external pressure when the phase difference is fixed at 1.72π. (b) Relative phase between the transmitted amplitude $A_{transTotal}$ and $A_{transIn}$.

We have also considered an external traction force. Figure 3.13(a) shows the transmission coefficient versus the phase difference when the magnitude is set to be 8MPa. It gets the maximum and minimum values with the phase difference 1.75π and 0.75π respectively where the transmitted amplitudes $A_{transEx}$ and $A_{transIn}$ are in-phase and out-of-phase. Figure 3.13(b) displays the transmission coefficient against the magnitude with the phase difference fixed to be 1.75π. The total transmission is achieved with the magnitude −13.2MPa or 8MPa. The transmission coefficient becomes zero with the magnitude −2.6MPa. In contrast to the external pressure, more injected energy is needed to obtain the total and zero transmission for the external traction force.

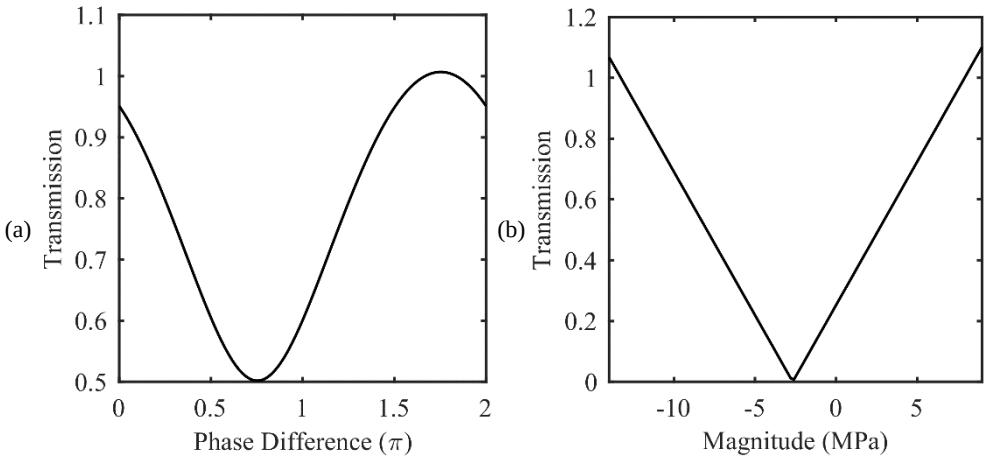

Figure 3.13: (a) Transmission coefficient against the phase difference of the external traction force when the magnitude is assumed to be 8MPa. (b) Transmission coefficient against the magnitude when the phase difference is chosen to be 1.75π.

3.4.2 Line of pillars with superimposed modes

In this part, we discuss the active control of the transmission through the line of pillars when the bending resonance B2 and the compressional resonance C1 occur at the same frequency. In such situation, either the external traction force or pressure can well couple into the vibration of the pillars. The excitation frequency is tuned to be 7.5MHz in the vicinity of the eigenfrequency.

Firstly, we consider the case of an external traction force applied on the top with the magnitude set to be 0.2MPa. The transmission coefficient against the phase difference is shown in figure 3.14(a). It reaches the maximum and minimum values when the phases are 0.52π and 1.52π respectively. Meantime, the transmitted amplitudes $A_{transEx}$ and $A_{transIn}$ are in-phase and out-of-phase, as shown in figure 3.14(b). Subsequently, we fix the phase difference to be 0.52π. The evolution between the transmission coefficient and the magnitude is depicted in figure 3.14(c). The zero transmission is achieved when the magnitude is −0.25MPa and the transmission coefficient gets the value 1 when the magnitude is −0.68MPa or 0.19MPa. Figure 3.14(d) shows the relative phase between the transmitted amplitude $A_{transTotal}$ and $A_{transIn}$. When the magnitude is less than −0.25MPa, the transmitted wave from the internal excitation is totally cancelled out and the transmitted field entirely results from the external source. When the magnitude is in between −0.25MPa and 0, the destructive interference from the internal and external sources occur. The former one is partly cancelled out and the rest part gets transmitted. When the magnitude is greater than 0, constructive interference occurs and both sources positively contribute to the transmission.

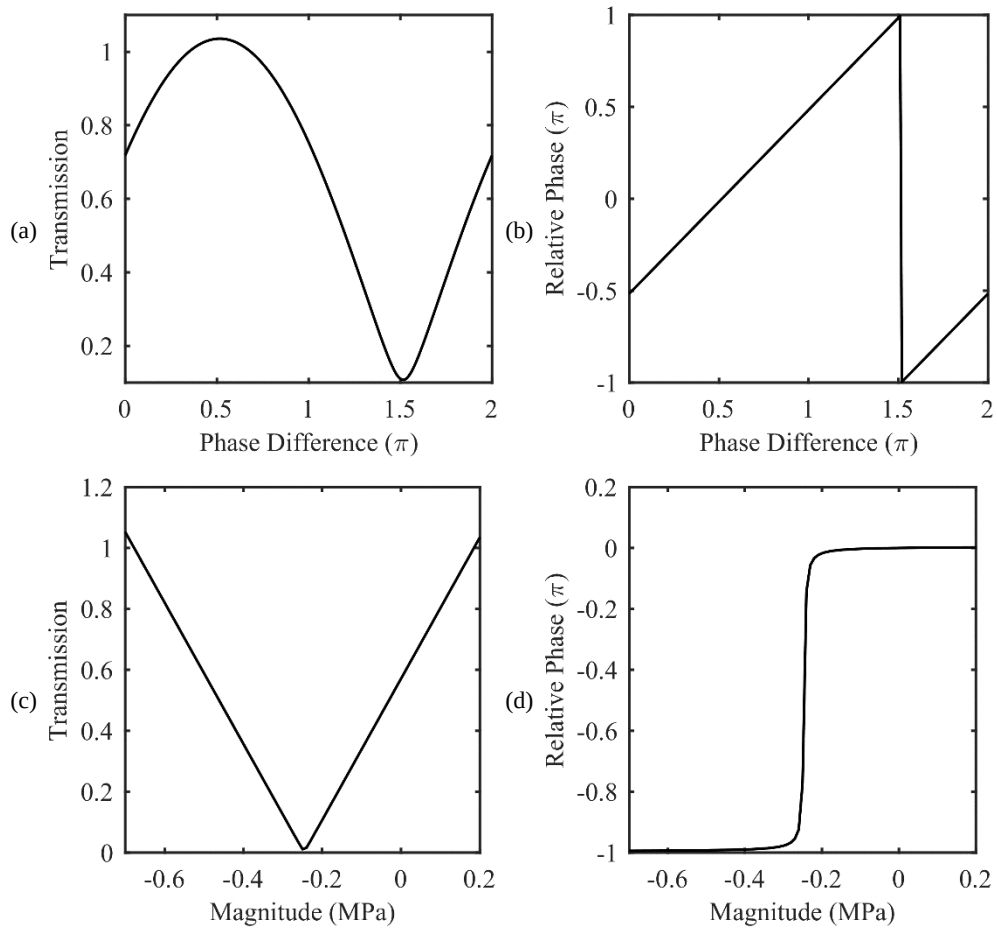

Figure 3.14: (a) Transmission coefficient against the phase difference of the external traction when the magnitude is assumed to be 0.2MPa. (b) Relative phase between the transmitted amplitude $A_{transEx}$ and $A_{transIn}$. (c) Transmission coefficient against the magnitude when the phase difference is fixed at 0.52π. (d) Relative phase between the transmitted amplitude $A_{transTotal}$ and $A_{transIn}$.

Secondly, an external pressure is applied on the top of the pillars. According to the transmission coefficient versus the phase difference shown in figure 3.15(a), with the magnitude set to be 0.25MPa and the relative phase between the transmitted amplitudes $A_{transEx}$ and $A_{transIn}$ depicted in figure 3.15(b), the transmitted amplitude $A_{transEx}$ is out-of-phase with $A_{transIn}$ for the phase difference of 0.08π. As a result, a dip occurs in the transmission spectrum whereas a peak is observed if the phase difference goes to 1.08π.

Afterwards, the transmission coefficient against the magnitude is illustrated in figure 3.15(c) with the phase difference fixed at 1.08π. It goes 0 at the magnitude −0.29MPa. And the total transmission can be achieved at the magnitude −0.78MPa or 0.21MPa. In the former case (*i.e.* −0.78MPa), the transmitted wave from the internal source is suppressed and the transmitted field solely depends on the external source, whereas in the latter case (0.21MPa), both sources make contribution according to the relative phase between the transmitted amplitude $A_{transTotal}$ and $A_{transIn}$ illustrated in figure 3.15(d).

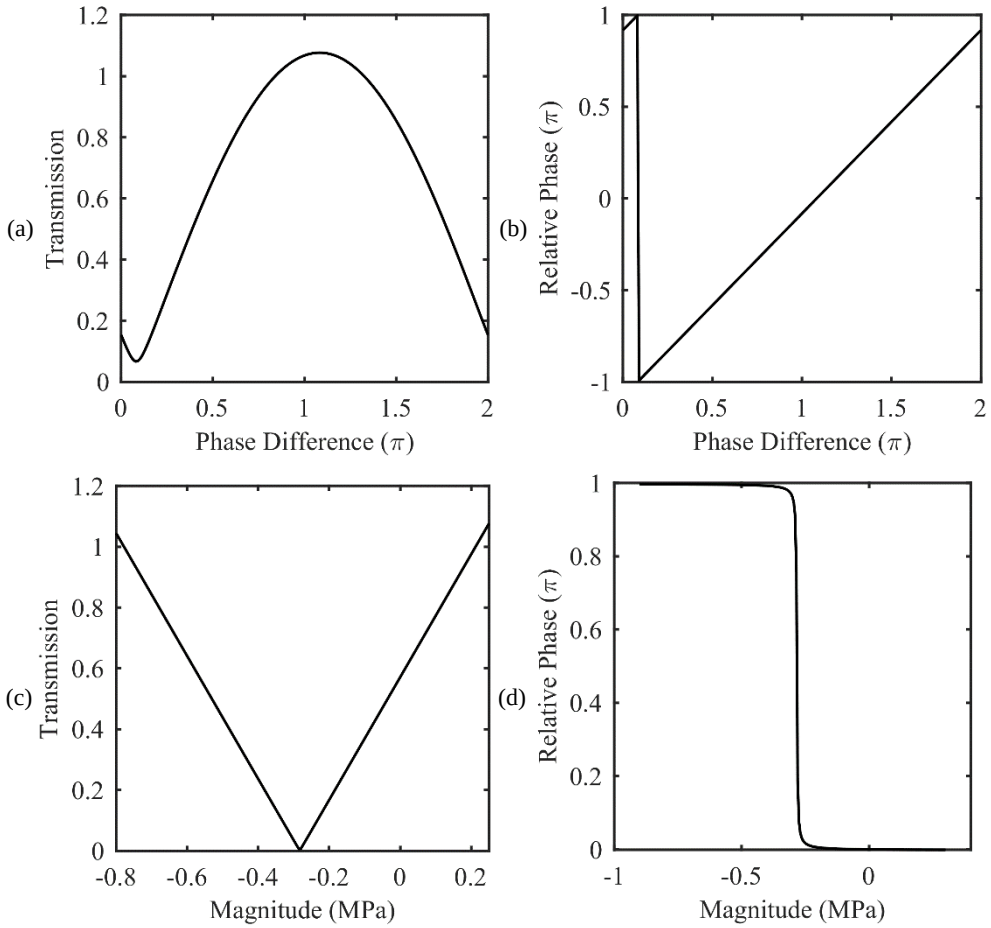

Figure 3.15: (a) Transmission coefficient against the phase difference of the external pressure when the magnitude is assumed to be 0.25MPa. (b) Relative phase between the transmitted amplitude $A_{transEx}$ and $A_{transIn}$. (c) Transmission coefficient against the magnitude when the phase difference is fixed at 1.08π. (d) Relative phase between the transmitted amplitude $A_{transTotal}$ and $A_{transIn}$.

In comparison, to achieve the zero transmission, we can apply an external traction force with the magnitude −0.25MPa and the phase difference 0.52π or an external pressure with the magnitude −0.29MPa and the phase difference 1.08π. In both approaches, the required injected energy is almost the same, the difference lies in the phase difference between the internal and external excitation. From the experimental point of view, it also provides a flexible manner to select the excitation device, for example, adopting the piezoelectric transducer to apply the external pressure and employing laser illumination to impose the external traction force. To obtain total transmission, the magnitude and the phase difference must be tuned to be 0.19MPa and 0.52π for the external traction force and 0.21MPa and 1.08π for the external pressure.

3.5 Conclusion

In this chapter, we have numerically investigated the active control of the transmission of an incident A_0 Lamb wave though a line of pillars by introducing an external excitation. Firstly, we have calculated the

transmission spectrum in order to recognize the resonant frequencies and modes of the line of pillars. The first-order bending resonances B1, the second-order bending resonance B2 and the first-order compressional resonance C1 result in three transmission dips. By a proper choice of the diameter of the pillars, the merging of the dips caused by the bending resonance B2 and the compressional resonance C1 can be obtained and hence optimizing the geometrical parameters, allow for the bending resonance B2 and the compressional resonance C1 to occur at the same frequency. In contrast to the pillared metamaterials or the phononic crystals, we have studied the effect of the coupling between the neighboring pillars on the resonant frequencies. We show that the coupling has a significant influence on the eigenfrequencies when the wavelength is of the same order of magnitude as the lattice constant and the coupling effect can be neglected in the subwavelength case. Secondly, the reemitted Lamb wave generated by the vibration of the line of pillars is analyzed. Its amplitude tends to be zero when the excitation frequency is far away from the eigenfrequencies. In the vicinity of the resonant frequencies, the amplitude in the complex plane rotates in the clockwise direction. When the bending resonance B2 and the compressional resonance C1 are separated, the magnitude of the reemitted Lamb wave is smaller than the incident Lamb wave. The transmitted wave is still in-phase with the incident wave. When the bending resonance B2 and the compressional resonance C1 are superimposed, the magnitude of the reemitted Lamb wave is larger than the incident Lamb wave. The transmitted wave turns out-of-phase with the incident Lamb wave. Thirdly, an external traction force or pressure applied on the top of the pillars is introduced to enhance or suppress the vibration downstream the line of resonators and to further control the transmission. In the vicinity of the bending resonance B2, the transmission coefficient can be continuously tuned in between 0 and 1 by imposing either a traction force or a pressure. Comparatively, the former one is more efficient. Less injected energy is needed to achieve the total or zero transmission. When the excitation frequency is close to the compressional resonance C1, applying an external pressure is a better choice. Further, when the bending resonance B2 and the compressional resonance C1 are superimposed, almost the same injected energy for both approaches is needed. The difference lies in the phase difference between the internal and external source. Thus, it provides a more flexible manner to select the external source.

General conclusion and perspectives

In this manuscript, we numerically demonstrated in the pillared phononic crystals and metamaterials two passive and one active approaches in manipulating the propagation of Lamb waves. In the first passive approach, we presented two mechanisms to achieve the doubly negative property in the double-sided pillared metamaterials, thus propagation of S_0 and SH_0 waves can be modulated in the subwavelength scale. In the second approach, we realized the topological transport of Lamb waves in the double-sided pillared phononic crystals and investigated the refraction at the zigzag termination and the transmission at the armchair termination. After that, we proposed an active way to control the transmission of A_0 Lamb wave propagating through an infinite line of pillars. We would like to summary the important findings in what follows.

To achieve the doubly negative property, we firstly studied two single-sided pillared metamaterials. By evaluating their effective properties in the vicinity of the resonant frequencies of the pillar, it is found that the combination of the bending and the compressional resonance results in the negative effective mass density and the torsional resonance leads to the negative effective shear modulus. Subsequently, based on these results, we obtained a SH polarized double-negative branch in an asymmetric double-sided pillared metamaterial that integrates the bending, the compressional and the torsional resonances into a common frequency interval. The width can be enlarged by simply involving perforated holes in the plate. We demonstrated inside this double-negative branch the polarization-dependent propagation along ΓX direction and the occurrence of the mode conversion from SH_0 mode towards A_0 (S_0) modes when deviating from ΓX direction. After that, a more special configuration, the symmetric double-sided pillared metamaterial, was considered. We presented a second mechanism to realize the doubly negative property. We show that the combination of the symmetric bending resonance and the antisymmetric compressional resonance results in the negative effective mass density and the symmetric compressional resonance contributes to the negative effective Young's modulus. Then, once the resonant frequency of the symmetric compressional mode is designed inside the frequency interval where the negative effective mass density occurs, a double-negative branch appears. Inside this double-negative branch, only the propagation of S_0 Lamb wave is allowed and while incident A_0 (SH_0) mode is totally reflected. Further, the applications in the negative refraction and zero-index refraction was also numerically evidenced.

Inspired by the unidirectional and lossless energy transport in the topological insulators, we extended this concept into the pillared phononic crystals. Following the previous discussion in the asymmetric double-sided configuration, we firstly resorted to its triangular counterpart. The double-negative branch was reserved. By transforming it to a honeycomb arrangement, a single Dirac cone occurred at point K of the BZ. We demonstrated inside the constituent branches of the Dirac cone the divergent wave propagation phenomena against the polarization and the propagation directions. Subsequently, by imposing the space-inversion symmetry breaking perturbation, the Dirac cone was lifted and the topological phase transition was introduced. By sandwiching two perturbed configurations with opposite valley Chern numbers to construct a three-layers ribbon supercell, the topologically valley-protected edge states occurring at the domain walls were obtained by calculating the band structure. It is found that the topological edge states might be gapped under the very large symmetry breaking perturbation. In that situation, very strong inter-valley scattering occurred at both the zigzag termination and sharp-corners which suggested that the topological protection was no longer guaranteed.

To be consistent, the topological transport in the symmetric double-sided pillared phononic crystals was studied. Thanks to the mirror-symmetry about the mid-plane of the plate, the symmetric and antisymmetric modes are completely decoupled that makes it possible to independently study their corresponding topological nature. For the antisymmetric dispersion curves, at the zigzag termination the valley-polarized edge states can refract into A_0 modes both positively and negatively. When increasing the height of the pillars, the negatively refractive angle quickly reaches maximum and vanishes. While at the armchair termination, either one or three transmitted A_0 modes can be observed depending the height of the pillars. For the symmetric dispersion curves, the situation became quietly complicated. When the Dirac cone occurred in the deep subwavelength scale, the topological edge states served as point sources once arriving the termination of the wave guide. Then, superposition of the wave fields generated by the points sources contributed to the transmission field, for example the circular shape wave front at the armchair outlet. When encountering the zigzag termination, the wave became evanescent at the interface owing to the extremely small wave vectors of S_0 and SH_0 modes in the plate and was strongly enhanced by the locally resonant modes. While increasing the height of the pillars, a second Dirac cone occurred at the high frequency. The corresponding valley-polarized refracted into S_0 and SH_0 modes. Subsequently, by optimizing the unit cell, a double Dirac cone was achieved. When breaking the mirror-symmetry about the plate, the double Dirac cone was lifted together with the opening of a nontrivial band gap. The symmetric and antisymmetric eigenmodes hybridized around the original double Dirac cone which introduced the emulation of the spin-orbit coupling interaction. By juxtaposing two perturbed systems with opposite spin Chern numbers, the topologically pseudospin-protected edge states occurred at the domain wall. Further, combining two perturbed configurations each supporting QSHE and QVHE respectively, the topologically pseudospin-

valley combined edge states were obtained at the domain walls. Their propagation depended on both the pseudospin and valley states. Based on these, we discussed the propagation of the topological pseudospin down state in a T-shaped wave guide and observed the valley based splitting at the junction.

Besides the passive approaches to manipulate Lamb waves, we also studied an active way to control the transmission of A_0 Lamb wave through an infinite line of pillars. The transmission spectrum was firstly computed which allows to identify the resonant frequencies and modes of the line of pillars. We show that the second-order bending resonance B2 and the first-order compressional resonance C1 superimposed in optimized design. In contrast to the pillared metamaterial, the coupling between the neighboring pillars on the resonant frequencies was investigated. It is found that the coupling has a significant influence on the resonant frequencies when the wavelength is the same order of magnitude as the lattice constant, but can be neglected in the subwavelength case. After that, we analyzed the reemitted wave by the pillars once excited into vibration. We found that the amplitude in the complex plane rotated in the clockwise direction when crossing the resonant frequencies. Further, we applied external traction force or pressure to enhance or suppress the vibration of the line of pillars to control the transmission. We show that the transmission coefficients can be continuously adjusted in between 0 and 1 by carefully choosing the magnitude and relative phase of the external sources. When the second-order bending resonance B2 and the first-order compressional resonance C1 are separated from each other, the external traction force is more efficient at the frequency close to the bending resonance frequency and less injected energy is needed for the external pressure around the compressional resonant frequency. while the second-order bending resonance B2 and the first-order compressional resonance C1 are superimposed, it is found that almost the same injected energy is required for both which provides a more flexible manner to select the external source.

The work in this manuscript is devoted to numerically study two passive approach exploring the doubly negative property and the topological transport and one active approach involving external sources to manipulate the propagation of Lamb waves. Experimental demonstration will be implemented to the evidence the numerical findings in future work, including the occurrence of the doubly negative property, the polarization filter behaviors and the topologically protected propagation. Regarding the topological transport in the symmetric double-sided pillared phononic crystals, it can be further extended. For example, investigating the topological edge states when simultaneously breaking the mirror-symmetry and the space-inversion symmetry and discussing the influence of the competition between two symmetry perturbations on the topological edge states. Concerning the active modulation, an actively tunable metasurface can be further developed. It can be done by gradually tuning the phase of the transmitted wave, thus abnormal refraction through the line of pillars might be achieved.

Bibliography

[1] P.A. Deymier, ed., Acoustic Metamaterials and Phononic Crystals, Springer Berlin Heidelberg, Berlin, Heidelberg, 2013.

[2] M.H. Lu, L. Feng, Y.F. Chen, Phononic crystals and acoustic metamaterials, Mater. Today. **12**, 34, (2009).

[3] G. Ma, P. Sheng, Acoustic metamaterials:From local resonances to broad horizons, Sci. Adv. **2**, e1501595, (2016).

[4] S.A. Cummer, J.C. Christensen, A. Alu, Controlling sound with acoustic metamaterials, Nat. Rev. Mater. **1**, 16001, (2016).

[5] M.R. Haberman, M.D. Guild, Acoustic metamaterials, Phys. Today. **69**, 42, (2016).

[6] M.S. Kushuwaha, P. Halevi, L. Dobrzynski, B. Djafari-Rouhani, Acoustic band structure of periodic elastic composites, Phys. Rev. Lett. **71**, 2022, (1993).

[7] J. Pierre, O. Boyko, L. Belliard, J.O. Vasseur, B. Bonello, Negative refraction of zero order flexural Lamb waves through a two-dimensional phononic crystal, Appl. Phys. Lett. **97**, 121919, (2010).

[8] X. Zhang, Z. Liu, Superlenses to overcome the diffraction limit, Nat. Mater. **7**, 435, (2008).

[9] M. Farhat, S. Guenneau, S. Enoch, Ultrabroadband elastic cloaking in thin plates, Phys. Rev. Lett. **103**, 024301, (2009).

[10] H. Nassar, H. Chen, A.N. Norris, G.L. Huang, Non-reciprocal flexural wave propagation in a modulated metabeam, Extrem. Mech. Lett. **15**, 97, (2017).

[11] Y. Pennec, B. Djafari-Rouhani, H. Larabi, J.O. Vasseur, A.C. Hladky-Hennion, Low-frequency gaps in a phononic crystal constituted of cylindrical dots deposited on a thin homogeneous plate, Phys. Rev. B. **78**, 104105, (2008).

[12] T.T. Wu, Z.G. Huang, T.C. Tsai, T.C. Wu, Evidence of complete band gap and resonances in a plate with periodic stubbed surface, Appl. Phys. Lett. **93**, 111902, (2008).

[13] Y. Jin, N. Fernez, Y. Pennec, B. Bonello, R.P. Moiseyenko, S. Hémon, Y. Pan, B. Djafari-Rouhani, Tunable waveguide and cavity in a phononic crystal plate by controlling whispering-gallery modes in hollow pillars, Phys. Rev. B. **93**, 054109, (2016).

[14] Y. Jin, Y. Pennec, Y. Pan, B. Djafari-Rouhani, Phononic Crystal Plate with Hollow Pillars Actively Controlled by Fluid Filling, Crystals. **6**, 64, (2016).

[15] Y. Jin, Y. Pennec, Y. Pan, B. Djafari-Rouhani, Phononic crystal plate with hollow pillars connected by thin bars, J. Phys. D. Appl. Phys. **50**, 035301, (2017).

[16] M. Oudich, B. Djafari-Rouhani, Y. Pennec, M.B. Assouar, B. Bonello, Negative effective mass density of acoustic metamaterial plate decorated with low frequency resonant pillars, J. Appl. Phys. **116**, 184504, (2014).

[17] M. Rupin, P. Roux, G. Lerosey, F. Lemoult, Symmetry issues in the hybridization of multi-mode waves with resonators: an example with Lamb waves metamaterial, Sci. Rep. **5**, 13714, (2015).

[18] W. Wang, B. Bonello, B. Djafari-Rouhani, Y. Pennec, J. Zhao, Double-Negative Pillared Elastic Metamaterial, Phys. Rev. Appl. **10**, 64011, (2018).

[19] W. Wang, B. Bonello, B. Djafari-Rouhani, Y. Pennec, J. Zhao, Exploring rotational resonance in elastic metamaterial plates to realize doubly negative property, ArXiv: 1801.06771, (2018).

[20] Y. Lai, Y. Wu, P. Sheng, Z.-Q. Zhang, Hybrid elastic solids, Nat. Mater. **10**, 620, (2011).

[21] X.N. Liu, G.K. Hu, G.L. Huang, C.T. Sun, An elastic metamaterial with simultaneously negative mass density and bulk modulus, Appl. Phys. Lett. **98**, 251907, (2011).

[22] V.E. Gusev, O.B. Wright, Double-negative flexural acoustic metamaterial, New J. Phys. **16**, 123053, (2014).

[23] R. Zhu, X.N. Liu, G.K. Hu, C.T. Sun, G.L. Huang, Negative refraction of elastic waves at the deep-subwavelength scale in a single-phase metamaterial., Nat. Commun. **5**, 5510, (2014).

[24] H.-W. Dong, S.-D. Zhao, Y.-S. Wang, C. Zhang, Topology optimization of anisotropic broadband double-negative elastic metamaterials, J. Mech. Phys. Solids. **105**, 54, (2017).

[25] Y. Zhou, X. Fang, D. Li, T. Hao, Y. Li, Acoustic Multiband Double Negativity from Coupled Single-Negative Resonators, Phys. Rev. Appl. **10**, 044006, (2018).

[26] M.Z. Hasan, C.L. Kane, Colloquium: Topological insulators, Rev. Mod. Phys. **82**, 3045, (2010).

[27] A. Bansil, H. Lin, T. Das, Colloquium: Topological band theory, Rev. Mod. Phys. **88**, 021004, (2016).

[28] G. Ma, M. Xiao, C.T. Chan, Topological phases in acoustic and mechanical systems, Nat. Rev. Phys. **1**, 281, (2019).

[29] P. Wang, L. Lu, K. Bertoldi, Topological Phononic Crystals with One-Way Elastic Edge Waves, Phys. Rev. Lett. **115**, 104302, (2015).

[30] L.M. Nash, D. Kleckner, A. Read, V. Vitelli, A.M. Turner, W.T.M. Irvine, Topological mechanics of gyroscopic metamaterials, Proc. Natl. Acad. Sci. **112**, 14495, (2015).

[31] Y. Ding, Y. Peng, Y. Zhu, X. Fan, J. Yang, B. Liang, X. Zhu, X. Wan, J. Cheng, Experimental Demonstration of Acoustic Chern Insulators, Phys. Rev. Lett. **122**, 014302, (2019).

[32] Z. Zhang, Q. Wei, Y. Cheng, T. Zhang, D. Wu, X. Liu, Topological Creation of Acoustic Pseudospin Multipoles in a Flow-Free Symmetry-Broken Metamaterial Lattice, Phys. Rev. Lett. **118**, 084303, (2017).

[33] S.H. Mousavi, A.B. Khanikaev, Z. Wang, Topologically protected elastic waves in phononic metamaterials, Nat. Commun. **6**, 8682, (2015).

[34] C. He, X. Ni, H. Ge, X.C. Sun, Y. Bin Chen, M.H. Lu, X.P. Liu, Y.F. Chen, Acoustic topological insulator and robust one-way sound transport, Nat. Phys. **12**, 1124, (2016).

[35] J. Lu, C. Qiu, L. Ye, X. Fan, M. Ke, F. Zhang, Z. Liu, Observation of topological valley transport of sound in sonic crystals, Nat. Phys. **13**, 369, (2017).

[36] J. Lu, C. Qiu, W. Deng, X. Huang, F. Li, F. Zhang, S. Chen, Z. Liu, Valley Topological Phases in Bilayer Sonic Crystals, Phys. Rev. Lett. **120**, 116802, (2018).

[37] M. Yan, J. Lu, F. Li, W. Deng, X. Huang, J. Ma, Z. Liu, On-chip valley topological materials for elastic wave manipulation, Nat. Mater. **17**, 993, (2018).

[38] M. Miniaci, R.K. Pal, R. Manna, M. Ruzzene, Valley based splitting of topologically protected helical waves in elastic plates, ArXiv: 1811.04814, (2018).

[39] Y. Kang, X. Cheng, X. Ni, A.B. Khanikaev, A.Z. Genack, Pseudospin-valley coupled edge states in

a photonic topological insulator, Nat. Commun. **9**, 3029, (2018).

[40] X. Ni, D. Purtseladze, D.A. Smirnova, A. Slobozhanyuk, A. Alù, A.B. Khanikaev, Spin- and valley-polarized one-way Klein tunneling in photonic topological insulators, Sci. Adv. **4**, eeap8802, (2018).

[41] F. Gao, H. Xue, Z. Yang, K. Lai, Y. Yu, X. Lin, Y. Chong, G. Shvets, B. Zhang, Topologically protected refraction of robust kink states in valley photonic crystals, Nat. Phys. **14**, 140, (2018).

[42] Y. Chen, X. Liu, G. Hu, Topological phase transition in mechanical honeycomb lattice, J. Mech. Phys. Solids. **122**, 54, (2019).

[43] T. Ma, G. Shvets, Scattering-free edge states between heterogeneous photonic topological insulators, Phys. Rev. B. **95**, 165102, (2017).

[44] C. He, S.-Y. Yu, H. Ge, H. Wang, Y. Tian, H. Zhang, X.-C. Sun, Y.B. Chen, J. Zhou, M.-H. Lu, Y.-F. Chen, Three-dimensional topological acoustic crystals with pseudospin-valley coupled saddle surface states, Nat. Commun. **9**, 4555, (2018).

[45] S. Chen, Y. Fan, Q. Fu, H. Wu, Y. Jin, J. Zheng, F. Zhang, A Review of Tunable Acoustic Metamaterials, Appl. Sci. **8**, 1480, (2018).

[46] F. Zangeneh-Nejad, R. Fleury, Active times for acoustic metamaterials, Rev. Phys. **4**, 100031, (2019).

[47] A. Baz, The structure of an active acoustic metamaterial with tunable effective density, New J. Phys. **11**, 123010, (2009).

[48] B.I. Popa, L. Zigoneanu, S.A. Cummer, Tunable active acoustic metamaterials, Phys. Rev. B. **88**, 024303, (2013).

[49] B.-I.I. Popa, D. Shinde, A. Konneker, S.A. Cummer, Active acoustic metamaterials reconfigurable in real time, Phys. Rev. B. **91**, 220303(R), (2015).

[50] L. Ning, Y.-Z. Wang, Y.-S. Wang, Active control of elastic metamaterials consisting of symmetric double Helmholtz resonator cavities, Int. J. Mech. Sci. **153**, 287, (2019).

[51] Z. Liu, X. Zhang, Y. Mao, Y.Y. Zhu, Z. Yang, C.T. Chan, P. Sheng, Locally resonant sonic materials, Science. **289**, 1734, (2000).

[52] Y. Wu, Y. Lai, Z. Zhang, Effective medium theory for elastic metamaterials in two dimensions, Phys. Rev. B. **76**, 205313, (2007).

[53] X. Zhou, G. Hu, Analytic model of elastic metamaterials with local resonances, Phys. Rev. B. **79**, 195109, (2009).

[54] J. Mei, Z. Liu, W. Wen, P. Sheng, Effective mass density of fluid-solid composites, Phys. Rev. Lett. **96**, 024301, (2006).

[55] Y. Ding, Z. Liu, C. Qiu, J. Shi, Metamaterial with simultaneously negative bulk modulus and mass density, Phys. Rev. Lett. **99**, 093904, (2007).

[56] N. Fang, D. Xi, J. Xu, M. Ambati, W. Srituravanich, C. Sun, X. Zhang, Ultrasonic metamaterials with negative modulus, Nat. Mater. **5**, 452, (2006).

[57] S.H. Lee, C.M. Park, Y.M. Seo, Z.G. Wang, C.K. Kim, Composite acoustic medium with simultaneously negative density and modulus, Phys. Rev. Lett. **104**, 054301, (2010).

[58] Y. Wu, Y. Lai, Z.Q. Zhang, Elastic metamaterials with simultaneously negative effective shear modulus and mass density, Phys. Rev. Lett. **107**, 105506, (2011).

[59] M. Yang, G. Ma, Z. Yang, P. Sheng, Coupled membranes with doubly negative mass density and bulk modulus, Phys. Rev. Lett. **110**, 134301, (2013).

[60] Q. Wei, Y. Cheng, X.J. Liu, Acoustic total transmission and total reflection in zero-index metamaterials with defects, Appl. Phys. Lett. **102**, 174104, (2013).

[61] L.-Y. Zheng, Y. Wu, X. Ni, Z.-G. Chen, M.-H. Lu, Y.-F. Chen, Acoustic cloaking by a near-zero-index phononic crystal, Appl. Phys. Lett. **104**, 161904, (2014).

[62] M. Lanoy, J.H. Page, G. Lerosey, F. Lemoult, A. Tourin, V. Leroy, Acoustic double negativity induced by position correlations within a disordered set of monopolar resonators, Phys. Rev. B. **96**, 220201, (2017).

[63] S. Kumar, P. Bhushan, O. Prakash, S. Bhattacharya, Double negative acoustic metastructure for attenuation of acoustic emissions, Appl. Phys. Lett. **112**, 101905, (2018).

[64] H.H. Huang, C.T. Sun, Anomalous wave propagation in a one-dimensional acoustic metamaterial having simultaneously negative mass density and Young's modulus, J. Acoust. Soc. Am. **132**, 2887, (2012).

[65] X. Wang, Dynamic behaviour of a metamaterial system with negative mass and modulus, Int. J. Solids Struct. **51**, 1534, (2014).

[66] Z. Li, X. Wang, On the dynamic behaviour of a two-dimensional elastic metamaterial system, Int. J. Solids Struct. **78**, 174, (2016).

[67] J.H. Oh, Y.E. Kwon, H.J. Lee, Y.Y. Kim, Elastic metamaterials for independent realization of negativity in density and stiffness, Sci. Rep. **6**, 23630, (2016).

[68] J.H. Oh, H.M. Seung, Y.Y. Kim, Doubly negative isotropic elastic metamaterial for sub-wavelength focusing: Design and realization, J. Sound Vib. **410**, 169, (2017).

[69] Y. Chen, G. Hu, G. Huang, A hybrid elastic metamaterial with negative mass density and tunable bending stiffness, J. Mech. Phys. Solids. **105**, 179, (2017).

[70] Y. Pennec, B. Djafari Rouhani, H. Larabi, A. Akjouj, J.N. Gillet, J.O. Vasseur, G. Thabet, Phonon transport and waveguiding in a phononic crystal made up of cylindrical dots on a thin homogeneous plate, Phys. Rev. B. **80**, 144302, (2009).

[71] M. Oudich, Y. Li, B.M. Assouar, Z. Hou, A sonic band gap based on the locally resonant phononic plates with stubs, New J. Phys. **12**, 083049, (2010).

[72] M. Oudich, M.B. Assouar, Z. Hou, Propagation of acoustic waves and waveguiding in a two-dimensional locally resonant phononic crystal plate, Appl. Phys. Lett. **97**, 193503, (2010).

[73] M. Oudich, M. Senesi, M.B. Assouar, M. Ruzenne, J.H. Sun, B. Vincent, Z. Hou, T.T. Wu, Experimental evidence of locally resonant sonic band gap in two-dimensional phononic stubbed plates, Phys. Rev. B. **84**, 165136, (2011).

[74] M. Badreddine Assouar, M. Senesi, M. Oudich, M. Ruzzene, Z. Hou, Broadband plate-type acoustic metamaterial for low-frequency sound attenuation, Appl. Phys. Lett. **101**, 173505, (2012).

[75] D. Zhang, J. Zhao, B. Bonello, F. Zhang, W. Yuan, Y. Pan, Z. Zhong, Investigation of surface acoustic wave propagation in composite pillar based phononic crystals within both local resonance and Bragg scattering mechanism regimes, J. Phys. D. Appl. Phys. **50**, 435602, (2017).

[76] M. Badreddine Assouar, M. Oudich, Enlargement of a locally resonant sonic band gap by using double-sides stubbed phononic plates, Appl. Phys. Lett. **100**, 123506, (2012).

[77] O.R. Bilal, M.I. Hussein, Trampoline metamaterial: Local resonance enhancement by springboards, Appl. Phys. Lett. **103**, 111901, (2013).

[78] O.R. Bilal, A. Foehr, C. Daraio, Observation of trampoline phenomena in 3D-printed metamaterial

plates, Extrem. Mech. Lett. **15**, 103, (2017).

[79] J. Zhao, B. Bonello, L. Becerra, O. Boyko, R. Marchal, Focusing of Rayleigh waves with gradient-index phononic crystals, Appl. Phys. Lett. **108**, 221905, (2016).

[80] S. Benchabane, R. Salut, O. Gaiffe, V. Soumann, M. Addouche, V. Laude, A. Khelif, Surface-Wave Coupling to Single Phononic Subwavelength Resonators, Phys. Rev. Appl. **8**, 034016, (2017).

[81] M. Oudich, B. Djafari-Rouhani, B. Bonello, Y. Pennec, S. Hemaidia, F. Sarry, D. Beyssen, Rayleigh Waves in Phononic Crystal Made of Multilayered Pillars: Confined Modes, Fano Resonances, and Acoustically Induced Transparency, Phys. Rev. Appl. **9**, 034013, (2018).

[82] Y. Jin, B. Bonello, R.P. Moiseyenko, Y. Pennec, O. Boyko, B. Djafari-Rouhani, Pillar-type acoustic metasurface, Phys. Rev. B. **96**, 104311, (2017).

[83] S. Li, T. Chen, X. Wang, Y. Li, W. Chen, Expansion of lower-frequency locally resonant band gaps using a double-sided stubbed composite phononic crystals plate with composite stubs, Phys. Lett. A. **380**, 2167, (2016).

[84] A. Hu, X. Zhang, F. Wu, Y. Yao, Enlargement of the locally resonant Lamb wave band gap of the phononic crystal plate at the deep sub-wavelength scale, Mater. Res. Express. **1**, 045801, (2014).

[85] R. Pourabolghasem, A. Khelif, S. Mohammadi, A.A. Eftekhar, A. Adibi, Physics of band-gap formation and its evolution in the pillar-based phononic crystal structures, J. Appl. Phys. **116**, 013514, (2014).

[86] S.H. Lee, O.B. Wright, Origin of negative density and modulus in acoustic metamaterials, Phys. Rev. B. **93**, 024302, (2016).

[87] R. Zhu, X.N. Liu, G.L. Huang, H.H. Huang, C.T. Sun, Microstructural design and experimental validation of elastic metamaterial plates with anisotropic mass density, Phys. Rev. B. **86**, 144307, (2012).

[88] Y. Xiao, J. Wen, X. Wen, Flexural wave band gaps in locally resonant thin plates with periodically attached spring–mass resonators, J. Phys. D. Appl. Phys. **45**, 195401, (2012).

[89] D. Qian, Z. Shi, Bandgap properties in simplified model of composite locally resonant phononic crystal plate, Phys. Lett. A. **381**, 3505, (2017).

[90] S. Yao, X. Zhou, G. Hu, Experimental study on negative effective mass in a 1D mass-spring system,

New J. Phys. **10**, 043020, (2008).

[91] Y.-F. Wang, Y.-S. Wang, C. Zhang, Two-dimensional locally resonant elastic metamaterials with chiral comb-like interlayers: Bandgap and simultaneously double negative properties, J. Acoust. Soc. Am. **139**, 3311, (2016).

[92] X.N. Liu, G.K. Hu, C.T. Sun, G.L. Huang, Wave propagation characterization and design of two-dimensional elastic chiral metacomposite, J. Sound Vib. **330**, 2536, (2011).

[93] D. Bigoni, S. Guenneau, A.B. Movchan, M. Brun, Elastic metamaterials with inertial locally resonant structures: Application to lensing and localization, Phys. Rev. B. **87**, 174303, (2013).

[94] A. Spadoni, M. Ruzzene, S. Gonella, F. Scarpa, Phononic properties of hexagonal chiral lattices, Wave Motion. **46**, 435, (2009).

[95] C. Ma, J. Guo, Y. Liu, Extending and lowing band gaps in one-dimensional phononic crystal strip with pillars and holes, J. Phys. Chem. Solids. **87**, 95, (2015).

[96] O.M. Ramahi, T.S. Almoneef, M. AlShareef, M.S. Boybay, Metamaterial particles for electromagnetic energy harvesting, Appl. Phys. Lett. **101**, 173903, (2012).

[97] A. Sukhovich, L. Jing, J.H. Page, Negative refraction and focusing of ultrasound in two-dimensional phononic crystals, Phys. Rev. B. **77**, 014301, (2008).

[98] J. Bucay, E. Roussel, J.O. Vasseur, P.A. Deymier, A.C. Hladky-Hennion, Y. Pennec, K. Muralidharan, B. Djafari-Rouhani, B. Dubus, Positive, negative, zero refraction, and beam splitting in a solid/air phononic crystal: Theoretical and experimental study, Phys. Rev. B. **79**, 214305, (2009).

[99] J. Zhao, R. Marchal, B. Bonello, O. Boyko, Efficient focalization of antisymmetric Lamb waves in gradient-index phononic crystal plates, Appl. Phys. Lett. **101**, 261905, (2012).

[100] J. Zhao, B. Bonello, O. Boyko, Focusing of the lowest-order antisymmetric Lamb mode behind a gradient-index acoustic metalens with local resonators, Phys. Rev. B. **93**, 174306, (2016).

[101] R. Zhu, X.N. Liu, G.L. Huang, Study of anomalous wave propagation and reflection in semi-infinite elastic metamaterials, Wave Motion. **55**, 73, (2015).

[102] H. Zhu, F. Semperlotti, Anomalous Refraction of Acoustic Guided Waves in Solids with Geometrically Tapered Metasurfaces, Phys. Rev. Lett. **117**, 034302, (2016).

[103] J. Xu, J. Tang, Tunable prism based on piezoelectric metamaterial for acoustic beam steering, Appl. Phys. Lett. **110**, 181902, (2017).

[104] H. Zhu, F. Semperlotti, Double-Zero-Index Structural Phononic Waveguides, Phys. Rev. Appl. **8**, 064031, (2017).

[105] F. Liu, X. Huang, C.T. Chan, Dirac cones at $k \rightarrow 0$ in acoustic crystals and zero refractive index acoustic materials, Appl. Phys. Lett. **100**, 071911, (2012).

[106] T. Ma, A.B. Khanikaev, S.H. Mousavi, G. Shvets, Guiding electromagnetic waves around sharp corners: Topologically protected photonic transport in metawaveguides, Phys. Rev. Lett. **114**, 127401, (2015).

[107] L.-H. Wu, X. Hu, Scheme for Achieving a Topological Photonic Crystal by Using Dielectric Material, Phys. Rev. Lett. **114**, 223901, (2015).

[108] Y.D. Lensky, J.C. Song, P. Samutpraphoot, L.S. Levitov, Topological Valley Currents in Gapped Dirac Materials, Phys. Rev. Lett. **114**, 256601, (2015).

[109] X. Cheng, C. Jouvaud, X. Ni, S.H. Mousavi, A.Z. Genack, A.B. Khanikaev, Robust reconfigurable electromagnetic pathways within a photonic topological insulator, Nat. Mater. **15**, 542, (2016).

[110] X. Wu, Y. Meng, J. Tian, Y. Huang, H. Xiang, D. Han, W. Wen, Direct observation of valley-polarized topological edge states in designer surface plasmon crystals, Nat. Commun. **8**, 1304, (2017).

[111] S. Yves, R. Fleury, T. Berthelot, M. Fink, F. Lemoult, G. Lerosey, Crystalline metamaterials for topological properties at subwavelength scales, Nat. Commun. **8**, 16023, (2017).

[112] J.W. Dong, X.D. Chen, H. Zhu, Y. Wang, X. Zhang, Valley photonic crystals for control of spin and topology, Nat. Mater. **16**, 298, (2017).

[113] S. Yves, T. Berthelot, M. Fink, G. Lerosey, F. Lemoult, Measuring Dirac Cones in a Subwavelength Metamaterial, Phys. Rev. Lett. **121**, 267601, (2018).

[114] Y. Yang, Y.F. Xu, T. Xu, H.X. Wang, J.H. Jiang, X. Hu, Z.H. Hang, Visualization of a Unidirectional Electromagnetic Waveguide Using Topological Photonic Crystals Made of Dielectric Materials, Phys. Rev. Lett. **120**, 217401, (2018).

[115] J. Noh, S. Huang, K.P. Chen, M.C. Rechtsman, Observation of Photonic Topological Valley Hall Edge States, Phys. Rev. Lett. **120**, 063902, (2018).

[116] M.I. Shalaev, W. Walasik, A. Tsukernik, Y. Xu, N.M. Litchinitser, Robust topologically protected transport in photonic crystals at telecommunication wavelengths, Nat. Nanotechnol. **14**, 31, (2019).

[117] Z. Yang, F. Gao, X. Shi, X. Lin, Z. Gao, Y. Chong, B. Zhang, Topological Acoustics, Phys. Rev. Lett. **114**, 114301, (2015).

[118] R. Fleury, A.B. Khanikaev, A. Alù, Floquet topological insulators for sound, Nat. Commun. **7**, 11744, (2016).

[119] J. Lu, C. Qiu, M. Ke, Z. Liu, Valley Vortex States in Sonic Crystals, Phys. Rev. Lett. **116**, 093901, (2016).

[120] M. Serra-Garcia, V. Peri, R. Süsstrunk, O.R. Bilal, T. Larsen, L.G. Villanueva, S.D. Huber, Observation of a phononic quadrupole topological insulator, Nature. **555**, 342, (2018).

[121] H. He, C. Qiu, L. Ye, X. Cai, X. Fan, M. Ke, F. Zhang, Z. Liu, Topological negative refraction of surface acoustic waves in a Weyl phononic crystal, Nature. **560**, 61, (2018).

[122] X.-T. He, E.-T. Liang, J.-J. Yuan, H.-Y. Qiu, X.-D. Chen, F.-L. Zhao, J.-W. Dong, A Silicon-on-Insulator Slab for Topological Valley Transport, Nat. Commun. **10**, 872, (2018).

[123] F. Gao, Y. Yang, Y. Chong, B. Zhang, H. Xue, Acoustic higher-order topological insulator on a kagome lattice, Nat. Mater. **18**, 108, (2018).

[124] S.-Y. Yu, C. He, Z. Wang, F.-K. Liu, X.-C. Sun, Z. Li, H.-Z. Lu, M.-H. Lu, X.-P. Liu, Y.-F. Chen, Elastic pseudospin transport for integratable topological phononic circuits, Nat. Commun. **9**, 3072, (2018).

[125] H. Fan, B. Xia, L. Tong, S. Zheng, D. Yu, Elastic higher-order topological insulator with topologically protected corner states, Phys. Rev. Lett. **122**, 204301, (2018).

[126] A. Foehr, O.R. Bilal, S.D. Huber, C. Daraio, Spiral-Based Phononic Plates: From Wave Beaming to Topological Insulators, Phys. Rev. Lett. **120**, 205501, (2018).

[127] X. Zhang, H.-X. Wang, Z.-K. Lin, Y. Tian, B. Xie, M.-H. Lu, Y.-F. Chen, J.-H. Jiang, Second-order topology and multidimensional topological transitions in sonic crystals, Nat. Phys. **10**, 1038, (2019).

[128] F. Zangeneh-Nejad, R. Fleury, Topological Fano Resonances, Phys. Rev. Lett. **122**, 014301, (2019).

[129] X. Ni, M. Weiner, A. Alù, A.B. Khanikaev, Observation of higher-order topological acoustic states

protected by generalized chiral symmetry, Nat. Mater. **18**, 113, (2019).

[130] A.B. Khanikaev, R. Fleury, S.H. Mousavi, A. Alù, Topologically robust sound propagation in an angular-momentum-biased graphene-like resonator lattice, Nat. Commun. **6**, 8260, (2015).

[131] Y.T. Wang, P.G. Luan, S. Zhang, Coriolis force induced topological order for classical mechanical vibrations, New J. Phys. **17**, 073031, (2015).

[132] X. Ni, C. He, X.C. Sun, X.P. Liu, M.H. Lu, L. Feng, Y.F. Chen, Topologically protected one-way edge mode in networks of acoustic resonators with circulating air flow, New J. Phys. **17**, 053016, (2015).

[133] Z.G. Chen, Y. Wu, Tunable Topological Phononic Crystals, Phys. Rev. Appl. **5**, 054021, (2016).

[134] H. Chen, H. Nassar, G.L. Huang, A study of topological effects in 1D and 2D mechanical lattices, J. Mech. Phys. Solids. **117**, 22, (2018).

[135] S. Yves, R. Fleury, F. Lemoult, M. Fink, G. Lerosey, Topological acoustic polaritons: Robust sound manipulation at the subwavelength scale, New J. Phys. **19**, 075003, (2017).

[136] Y. Deng, H. Ge, Y. Tian, M. Lu, Y. Jing, Observation of zone folding induced acoustic topological insulators and the role of spin-mixing defects, Phys. Rev. B. **96**, 184305, (2017).

[137] B.Z. Xia, T.T. Liu, G.L. Huang, H.Q. Dai, J.R. Jiao, X.G. Zang, D.J. Yu, S.J. Zheng, J. Liu, Topological phononic insulator with robust pseudospin-dependent transport, Phys. Rev. B. **96**, 094106, (2017).

[138] S.Y. Huo, J.J. Chen, H.B. Huang, Topologically protected edge states for out-of-plane and in-plane bulk elastic waves, J. Phys. Condens. Matter. **30**, 145403, (2018).

[139] L. Yang, K. Yu, Y. Wu, R. Zhao, S. Liu, Topological spin-Hall edge states of flexural wave in perforated metamaterial plates, J. Phys. D. Appl. Phys. **51**, 325302, (2018).

[140] J. Cha, K.W. Kim, C. Daraio, Experimental realization of on-chip topological nanoelectromechanical metamaterials, Nature. **564**, 229, (2018).

[141] R. Chaunsali, C.W. Chen, J. Yang, Experimental demonstration of topological waveguiding in elastic plates with local resonators, New J. Phys. **20**, 113036, (2018).

[142] R. Chaunsali, C.W. Chen, J. Yang, Subwavelength and directional control of flexural waves in zone-

folding induced topological plates, Phys. Rev. B. **97**, 054307, (2018).

[143] M. Miniaci, R.K. Pal, B. Morvan, M. Ruzzene, Experimental Observation of Topologically Protected Helical Edge Modes in Patterned Elastic Plates, Phys. Rev. X. **8**, 031074, (2018).

[144] D. Torrent, J. Sánchez-Dehesa, Acoustic analogue of graphene: Observation of dirac cones in acoustic surface waves, Phys. Rev. Lett. **108**, 174301, (2012).

[145] D. Torrent, D. Mayou, J. Sanchez-Dehesa, Elastic analogue of graphene: Dirac cones and edge states in the propagation of flexural waves in thin plates, Phys. Rev. B. **87**, 115143, (2013).

[146] X. Ni, M.A. Gorlach, A. Alu, A.B. Khanikaev, Topological edge states in acoustic Kagome lattices, New J. Phys. **19**, 055002, (2017).

[147] L. Ye, C. Qiu, J. Lu, X. Wen, Y. Shen, M. Ke, F. Zhang, Z. Liu, Observation of acoustic valley vortex states and valley-chirality locked beam splitting, Phys. Rev. B. **95**, 174106, (2017).

[148] Z. Zhang, Y. Tian, Y. Wang, S. Gao, Y. Cheng, X. Liu, J. Christensen, Directional Acoustic Antennas Based on Valley-Hall Topological Insulators, Adv. Mater. **30**, 1803229, (2018).

[149] Y. Yang, Z. Yang, B. Zhang, Acoustic valley edge states in a graphene-like resonator system, J. Appl. Phys. **123**, 091713, (2018).

[150] X. Wen, C. Qiu, J. Lu, H. He, M. Ke, Z. Liu, Acoustic Dirac degeneracy and topological phase transitions realized by rotating scatterers, J. Appl. Phys. **123**, 091703, (2018).

[151] H. Ge, X. Ni, Y. Tian, S.K. Gupta, M.H. Lu, X. Lin, W.D. Huang, C.T. Chan, Y.F. Chen, Experimental Observation of Acoustic Weyl Points and Topological Surface States, Phys. Rev. Appl. **10**, 14017, (2018).

[152] J.-J. Chen, S.-Y. Huo, Z.-G. Geng, H.-B. Huang, X.-F. Zhu, Topological valley transport of plate-mode waves in a homogenous thin plate with periodic stubbed surface, AIP Adv. **7**, 115215, (2017).

[153] R.K. Pal, M. Ruzzene, Edge waves in plates with resonators: An elastic analogue of the quantum valley Hall effect, New J. Phys. **19**, 025001, (2017).

[154] Z. Wang, S.-Y. Yu, F.-K. Liu, Y. Tian, S. Kumar Gupta, M.-H. Lu, Y.-F. Chen, Slow and robust plate acoustic waveguiding with valley-dependent pseudospins, Appl. Phys. Express. **11**, 107310, (2018).

[155] J. Wang, J. Mei, Topological valley-chiral edge states of Lamb waves in elastic thin plates, Appl. Phys. Express. **11**, 057302, (2018).

[156] E. Riva, D.E. Quadrelli, G. Cazzulani, F. Braghin, Tunable in-plane topologically protected edge waves in continuum Kagome lattices, J. Appl. Phys. **124**, 164903, (2018).

[157] T.W. Liu, F. Semperlotti, Tunable Acoustic Valley-Hall Edge States in Reconfigurable Phononic Elastic Waveguides, Phys. Rev. Appl. **9**, 014001, (2018).

[158] N. Lera, D. Torrent, P. San-Jose, J. Christensen, J. V. Alvarez, Valley Hall phases in kagome lattices, Phys. Rev. B. **99**, 134102, (2019).

[159] T.-W. Liu, F. Semperlotti, Experimental evidence of robust acoustic valley Hall edge states in a non-resonant topological elastic waveguide, Phys. Rev. Appl. **11**, 014040, (2019).

[160] Z. Wang, M.-H. Lu, S.-Y. Yu, Y. Jing, F.-K. Liu, S.-L. Yan, Guiding robust valley-dependent edge states by surface acoustic waves, J. Appl. Phys. **125**, 044502, (2019).

[161] Y. Wu, R. Chaunsali, H. Yasuda, K. Yu, J. Yang, Dial-in Topological Metamaterials Based on Bistable Stewart Platform, Sci. Rep. **8**, 112, (2018).

[162] J. Vila, R.K. Pal, M. Ruzzene, Observation of topological valley modes in an elastic hexagonal lattice, Phys. Rev. B. **96**, 134307, (2017).

[163] H. Zhu, T.-W.W. Liu, F. Semperlotti, Design and experimental observation of valley-Hall edge states in diatomic-graphene-like elastic waveguides, Phys. Rev. B. **97**, 174301, (2018).

[164] X.-D. Chen, F.-L. Shi, H. Liu, J.-C. Lu, W.-M. Deng, J.-Y. Dai, Q. Cheng, J.-W. Dong, Tunable Electromagnetic Flow Control in Valley Photonic Crystal Waveguides, Phys. Rev. Appl. **10**, 044002, (2018).

[165] Y. Yang, H. Jiang, Z.H. Hang, Topological Valley Transport in Two-dimensional Honeycomb Photonic Crystals, Sci. Rep. **8**, 1588, (2018).

[166] Z. Zhang, Y. Cheng, X. Liu, Achieving acoustic topological valley-Hall states by modulating the subwavelength honeycomb lattice, Sci. Rep. **8**, 16784, (2018).

[167] S.Y. Huo, J.J. Chen, H.B. Huang, G.L. Huang, Simultaneous multi-band valley-protected topological edge states of shear vertical wave in two-dimensional phononic crystals with veins, Sci. Rep. **7**, 10335, (2017).

[168] A. Baz, Active acoustic metamaterial with tunable effective density using a disturbance rejection controller, J. Appl. Phys. **125**, 74503, (2017).

[169] B.I. Popa, S. a Cummer, Non-reciprocal and highly nonlinear active acoustic metamaterials., Nat. Commun. **5**, 3398, (2014).

[170] S. Xiao, G. Ma, Y. Li, Z. Yang, P. Sheng, Active control of membrane-type acoustic metamaterial by electric field, Appl. Phys. Lett. **106**, 091904, (2015).

[171] L. Fan, H. Zhang, C. Xue, J. Ding, Z. Chen, S. Zhang, X.-J. Li, A tunable acoustic metamaterial with double-negativity driven by electromagnets, Sci. Rep. **6**, 30254, (2016).